AD-A223 767

CLOSED CYCLE EXCIMER LASER CONCEPTUAL DESIGN EFFORT — PHASES I AND IA

OK DTIC

AVCO EVERETT RESEARCH LABORATORY, INC.

a Subsidiary of Avco Corporation
2385 Revere Beach Parkway
Everett, MA 02149

DTIC
ELECTE
JUN 27 1990
S D

June 1982
Final Technical Report for Period 17 September 1980 — 1 November 1981

APPROVED FOR PUBLIC RELEASE; DISTRIBUTION UNLIMITED.

Prepared for

DEFENSE ADVANCED RESEARCH PROJECTS AGENCY
DARPA Order No. 3505
Amendment No. 10

90 06 25 077

DO NOT

UNCLASSIFIED

REPORT DOCUMENTATION PAGE		READ INSTRUCTIONS BEFORE COMPLETING FORM
1. REPORT NUMBER	2. GOVT ACCESSION NO.	3. RECIPIENT'S CATALOG NUMBER
4. TITLE (and Subtitle) Closed Cycle Excimer Laser Conceptual Design Effort - Phases I and IA		5. TYPE OF REPORT & PERIOD COVERED Final Technical Report 9/17/80 - 11/1/81
		6. PERFORMING ORG. REPORT NUMBER
7. AUTHOR(s)		8. CONTRACT OR GRANT NUMBER(s) DAAH01-80-C-1783
9. PERFORMING ORGANIZATION NAME AND ADDRESS Avco Everett Research Laboratory, Inc. 2385 Revere Beach Parkway Everett, MA 02149		10. PROGRAM ELEMENT, PROJECT, TASK AREA & WORK UNIT NUMBERS
11. CONTROLLING OFFICE NAME AND ADDRESS Defense Advanced Research Projects Agency DARPA Order No. 3505 Amendment No. 10		12. REPORT DATE June 1982
		13. NUMBER OF PAGES 196
14. MONITORING AGENCY NAME & ADDRESS(If different from Controlling Office) U.S. Army Missile Command Redstone Arsenal, AL 35809		15. SECURITY CLASS. (of this report) Unclassified
		15a. DECLASSIFICATION/DOWNGRADING SCHEDULE

16. DISTRIBUTION STATEMENT (of this Report)

Approved for public release; distribution unlimited

17. DISTRIBUTION STATEMENT (of the abstract entered in Block 20, if different from Report)

18. SUPPLEMENTARY NOTES

19. KEY WORDS (Continue on reverse side if necessary and identify by block number)

XeF Laser
Laser Raman Conversion
Repetitively Pulsed Gas Laser
Close Loop Gas Laser
E-Beam

Gas Processor
Injection Locking
Blue-Green Conversion
Flow and Acoustics
Pulse-Power

20. ABSTRACT (Continue on reverse side if necessary and identify by block number)

A conceptual design has been generated for a blue-green laser system with a closed cycle XeF laser as the driver. The XeF laser serves to integrated laser technologies and to provide a test bed for addressing scaling issues. Scaling is of interest for a practical Raman shifted blue-green laser ground based communications system. Scaling to higher powers for weapons application is also of interest.

DD FORM 1473 1 JAN 73   EDITION OF 1 NOV 65 IS OBSOLETE

The reported conceptual design meets all performance requirements. Demonstrated technologies are used wherever possible. The device is aimed at addressing all critical technologies including high reliability, high overall efficiency ($\geq 1\%$) and good beam quality (≥ 1.3 DL).

Component and system trade-offs were conducted to produce a baseline design. These studies point to areas where improvements in existing technologies are warranted. Scaling issues and the extent to which they are addressed by the XeF integrator are given. Recommendations are made for critical experiments.

Accesion For		
NTIS CRA&I	☑	
DTIC TAB	☐	
Unannounced	☐	
Justification		
By		
Distribution /		
Availability Codes		
Dist	Avail and / or Special	
A-1		

TABLE OF CONTENTS

AVCO EVERETT

◿◿AVCO EVERETT

LIST OF ILLUSTRATIONS

LIST OF TABLES

1.0 BACKGROUND AND INTRODUCTION

This report covers work performed under the Closed Cycle Excimer Laser Conceptual Design Program. The program is divided into two phases, Phase I and Phase IA. The Phase I effort was directed towards a conceptual design of a small closed cycle XeF laser while the Phase IA effort was directed towards a conceptual design of a blue-green laser system with a closed cycle XeF laser as the driver. The results generated under the Phase I program have been reported at DARPA in January 1981. Furthermore, that work has largely been superceded by the work performed subsequently under the Phase IA program, and, therefore, will not be included here. This report deals with work performed under the Phase IA effort.

1.1 PROGRAM SCOPE AND OBJECTIVES

The objective of the Phase IA effort is to produce a conceptual design of a blue-green laser system with a closed cycle XeF laser as the driver. The design of the closed cycle XeF laser is (if implemented under Phase II) to be used to demonstrate performance and technical scaling compatible with the requirements for the development of a driver for a Raman shifted blue-green laser useful for a ground based laser communications system. In addition, the design should also address component and subsystem technologies required for the development of large-scale excimer laser systems.

The various performance requirements for the XeF laser driver and Raman conversion system which we took as firm design goals are summarized in Table 1. The conceptual design reported here if implemented can satisfy all these requirements.

In addition to meeting all the performance requirements, the design reported is also driven by: (1) the use (where possible) of demonstrated technologies, (2) the goal of using the device to demonstrate all critical technologies required for an operational communication system, particularly those necessary to achieve long continuous run duration (> 10 hrs), high overall

AVCO EVERETT

TABLE 1. XeF INTEGRATOR DESIGN REQUIREMENTS

REQUIREMENTS	XeF	BLUE—GREEN
PULSE ENERGY	$\geq$ 100 J	30 J
PULSE LENGTH	$\geq$ 1 μ sec	SAME
AVERAGE POWER	> 10 KW	> 3 KW
REPETITION RATE (AVERAGE)	$\geq$ 100 pps	SAME
RECOVERY TIME (FOR PULSE INTERVAL MODULATION)	$\leq$ 5 msec	SAME
RUN TIME	$\geq$ 1 min continuous	SAME
DUTY CYCLE (DOWN TIME, ETC.)	5 ten sec runs/day 2 one min runs/month	SAME
BEAM QUALITY	$\leq$ 1.3 times Diffraction Limit	SAME
BANDWIDTH	—	< 1 Å
BEAM INTENSITY UNIFORMITY (NEAR FIELD)	$\pm$ 25% OF AVERAGE INTENSITY	SAME
OPTICAL LENGTH	$\geq$ 50 cm	SAME

NOMINAL OPERATING PARAMETERS

COMPONENT EFFICIENCIES		
PFN	$\geq$ 50%	SAME
E—GUN	$\geq$ 50%	SAME
CAVITY	$\geq$ 4.5%	SAME
RAMAN CELL		> 30%
WAVELENGTH	351 nm	450—520 nm
OVERALL SYSTEM EFFICIENCY	$\geq$ 1%	
CAVITY GAS		
TEMPERATURE	300—450°K	
DENSITY	2.0 – 3.6 amagat	

K2897

10

efficiency ($\geq$ 1 percent), and good beam quality ($<$ 1.3 and (3) the further use of this device to address scaling issues compatible with the development of high-power excimer laser systems for various other DARPA missions.

The salient features of the design are briefly outlined below. Also included in this section is a summary of assessment of the state of the technology and major technical risk areas associated with the implementation of the design.

1.2 CONCEPTUAL DESIGN OVERVIEW

The design of the XeF laser driver is based primarily on work performed under previous DARPA funding. The laser employs direct transverse e-beam excitation of high pressure $Ne/Xe/NF_3$, mixtures at elevated temperatures. The single pulse performance obtainable from such lasers is well understood theoretically and has been demonstrated experimentally on a variety of devices.

The basic geometry of the laser cavity is illustrated in Figure 1. The laser active volume is rectangular in shape with face-to-face e-guns along one axis providing the excitation. A gas flow is used along a second axis to flush the active volume and provide fresh gas for each pulse in repetitively-pulsed operation. The laser energy is extracted along the third axis with an optical resonator.

The active medium was chosen to be 12 cm in the gas flow direction, 14 cm in the e-beam direction and 130 cm along the optical resonator axis, yielding a total active volume of 21.8 liters. Of this volume useful laser energy would be extracted from the centra 20.3 liters after exclusion of boundary layers adjacent to the e-beam foil windows. The laser mixture was chosen to be 3.5 amagats of $Ne/Xe/NF_3$, operated at $450°K$. With an average e-beam excitation of intensity of 1.67×10^5 W/cm^3 and a pulse length of 1 μs, a specific energy of 7.5 J/liter is expected with an intrinsic efficiency of 4.5 percent.

The e-beams emerge through two face-to-face foil windows. The primary foil cooling concept chosen is conduction cooling. The foil is 1/2 mil thick titanium and 1/2 mil thick aluminum sandwich made by ion vapor deposition of aluminum on titanium. The titanium provides high-temperature structural strength while the aluminum provides heat conduction into the water-cooled foil support structure. The foil free span is 3.0 mm. The geometric transmission of the foil support structure is 65 percent.

11
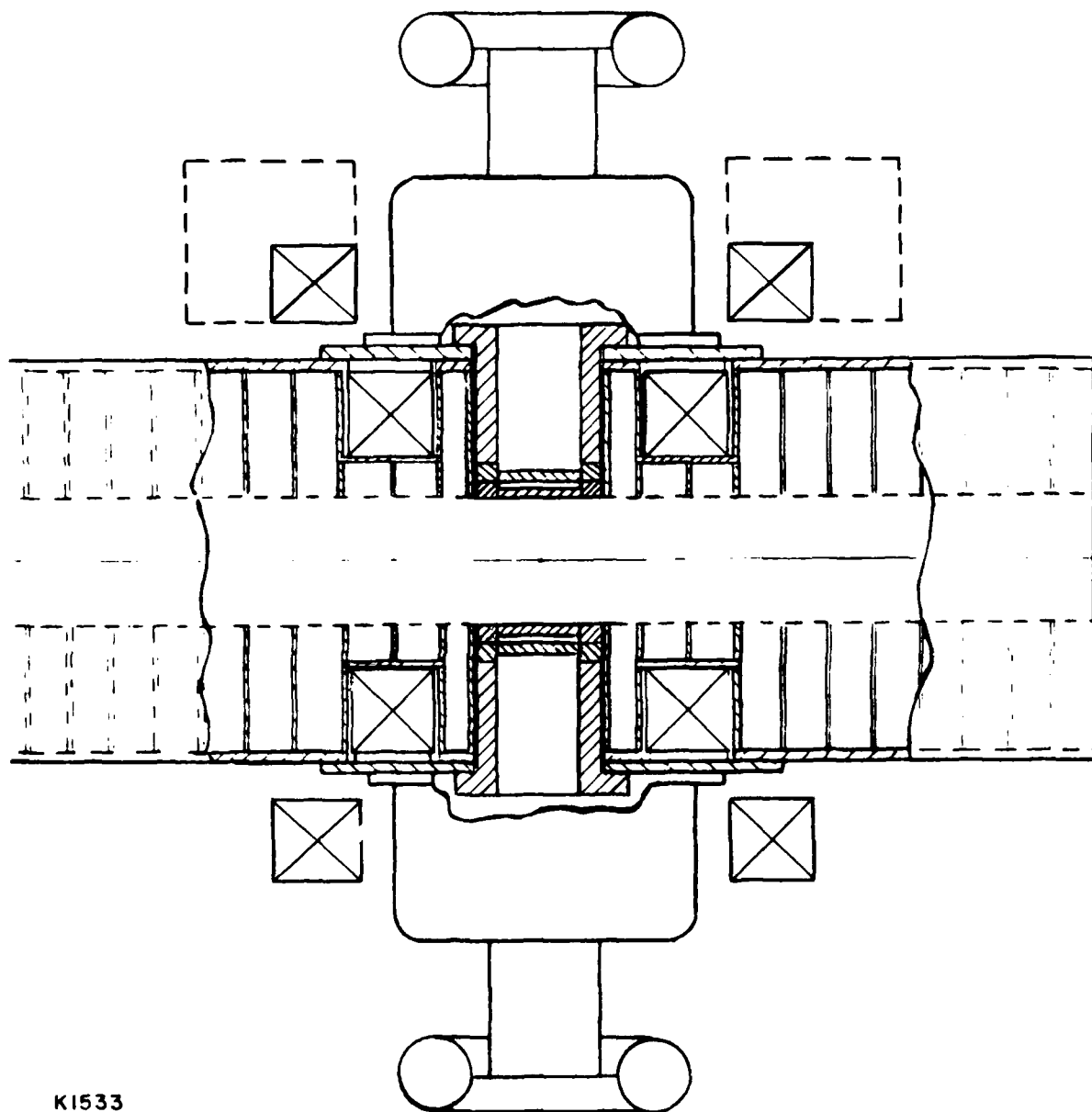
K1533

Figure 1.   Laser Cavity Arrangements

12

The e-guns are cold cathode field emission diodes. The cathode material is chosen to be carbon felt. The cathode is pulsed to 250 kV at 2 pulse lengths of 1 μs and 2 μs. Because of diode closure the e-beam current is expected to increase by a factor of two during the 1 μs pulse.

The e-beam is confined and guided into the active laser volume by an externally applied magnetic field of 1.5-2 kG. The field is generated by two racetrack-shaped water-cooled copper coils located external to the e-gun vacuum chambers. The coils are driven by a conventional low voltage high current dc power supply.

The e-guns are driven by two 10 section type E voltage fed PFNs. The PFNs utilize parallel plate oil capacitors. Constant voltage operation into a time varying load is achieved with passive uncharged type C voltage compensating networks. The PFNs are balance charged to ± 250 kV. Each PFN is switched by two air blown sparkgaps. One of the sparkgaps is a series injection triggered gap while the other is operated in the self-break mode.

The PFNs are charged, via pulse transformers, by thyratron switched command charge modulators. Voltage regulation is provided by de-Qing circuits. The PFN and modulators are oil insulated and contained in a single oil tank. Their outputs are fed into the e-guns via coaxial oil insulated lines.

Pressure wave attenuation inside the laser cavity and flow channel is provided by close-in sidewall mufflers located upstream and downstream of the laser cavity. Boundary layer suction is used through the upstream mufflers to minimize boundary layer thickness over the foil windows.

Downstream from the mufflers is a 1 to 3 area ratio diffuser which provides partial pressure recovery. Waste heat is extracted from the gas stream with a heat exchanger immediately downstream of the diffuser. The heat exchanger is modular in construction so that heat exchangers of differing effectiveness can be accommodated with ease.

The flow then goes through a vaned turn, a constant area rectangle to cylindrical transition, another 90° vaned turn, into the return leg. The flow is driven by a single stage, adjustable pitch, vane-axial fan powered by a variable speed hydraulic motor located in the return leg. Sidewall mufflers up and downstream from the fan provide acoustic quieting of fan noise.

Downstream of the fan is a fan diffuser, a 90° vaned turn, a cylindrical to rectangular transition, another vaned turn which brings the flow into a velocity/thermal equalizer located just upstream of the 3 to 1 area ratio nozzle before entry into the size wall muffler section upstream of the laser cavity. A schematic of the flow loop is shown in Figure 2.

To maintain constant laser gas chemistry < 10 percent of the flow is diverted into a gas processor. The gas processor consists of a hot alkali metal gas scrubber which removes all but the rare gases from the gas stream. Reactants are then reinjected into gas stream downstream from the scrubber to maintain constant NF_3 concentration in the flow loop. A regenerative heat exchanger is used on entry and exit from the scrubber to minimize heater power required to bring the gas temperature up to that required in the scrubber.

Laser energy extraction is achieved by an on-axis confocal unstable resonator with 84 percent output coupling. The resonator mirrors are located external to the laser cavity. Windows to the laser cavity are 3.5 cm thick AR coated CaF_2 flats. Temperature transition between the laser cavity and ambient is taken across a vacuum. For a one-minute burst mode operation, no active thermal control is necessary and no active wavefront compensation is used.

Narrow band single frequency operation (necessary for 1 Å bandwidth in blue-green) of the XeF laser is achieved by operating the XeF laser as an injection locked oscillator. The injector is a low power, frequency stable, narrow line, XeF laser which can be a discharge pumped laser.

Raman conversion into the blue-green is achieved by two sequential Stokes shifts in high pressure H_2. The concept chosen utilizes two separate H_2 cells. The Stokes shifts are taken sequentially first from XeF wavelengths into the violet (411 nm) in the first cell and then into the blue-green (500 nm) in the second cell. The Raman cells are operated as power amplifiers with low level injection at 411 and 500 nm provided either by uncorrelated dye lasers or correlated Raman oscillators pumped by splitting off a small portion of the main XeF beam.

High intensity needed for efficiency conversion in moderate length cells is achieved by focusing the pump beams to 15 J/cm^2 in the UV and 25 J/cm^2 in the violet before entrance to the Raman cells. Damage to the windows is avoided by using uncoated CaF_2 windows. The net energy conversion efficiency from XeF into the blue-green is expected to be > 30 percent.

14
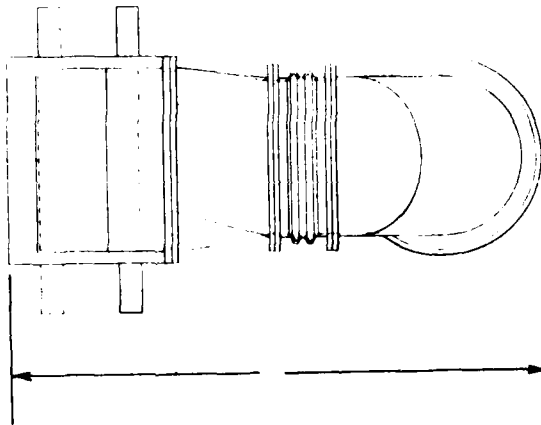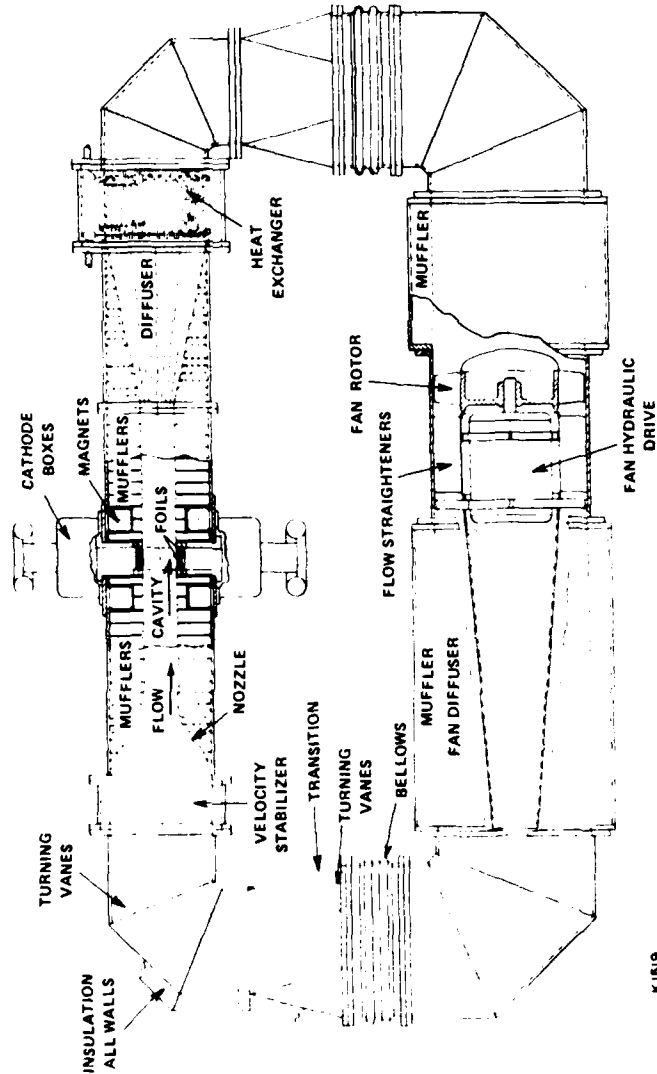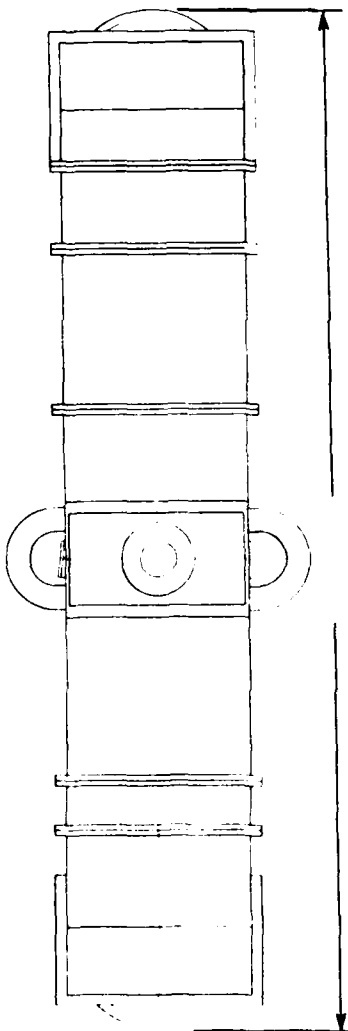
Figure 2.   Flow Loop Arrangements

K1519

15

H_2 gas flow is provided in the H_2 cells by fan driven flow loops. Acoustic attenuation in the Raman cells is provided by sidewall mufflers. Thermal homogeneity is achieved by heat exchangers and thermal stabilizers, analogous to that used in the XeF laser.

The conceptual design outlined will be capable of achieving all the performance goals listed in Table 2. However, in order to address the goals of long continuous duration run times and high efficiency (> 1 percent overall into the blue-green) necessary for an operational communication system and technologies relevant to the development of high-powered XeF system for other DARPA missions, we recommend that the device be upgradable in two additional phases in the future.

In the first phase the device should be upgraded to address technologies required to achieve long continuous operation of the XeF drive/Raman converter systems. To do this, thermionic cathode technology developed under DARPA/AERL funding at AERL would be implemented on the XeF laser e-guns. This would allow the e-guns to be run for extended periods. In addition thermionic cathodes would allow the XeF laser to be operated at constant e-beam current leading to an approximately constant power output pulse from the XeF laser. This would enable slightly higher XeF laser efficiency and > 50 percent Raman energy (compared with ~ 30 percent with cold cathodes) conversion into the blue-green. Also the optical system will have to be modified to include active cooling on the windows and mirrors. Active phase compensation may also be necessary to achieve steady-state optical quality performance.

1.3 CONCLUSIONS AND MAJOR TECHNOLOGY RISK AREAS

The major conclusions of this conceptual design study are:

a) The performance goals for the Closed Cycle XeF Laser/Blue-Green Raman Converter can be met with acceptable risk.

b) Areas where improvement in existing demonstrated technologies are needed have been identified. (This is briefly discussed below.)

c) The device can be upgraded to demonstrate remaining technologies necessary for the development of an operational ground based communication system so that this development can then proceed expeditiously with low risk.

TABLE 2. AREAS WHERE TECHNOLOGY ADVANCEMENTS ARE REQUIRED

Laser Cavity

Efficient XeF energy extraction with narrow line operation via injection
locking. (elevated temperature)

Foils

Foil reliability and lifetime.

E-Beams

Cold cathode lifetime.

Outgassing.

Pulse Power

Long life high-voltage sparkgap switches.

Acoustics

Impact of variable pulse internal on medium recovery.

Recyclability

Flow loop materials compatibility.

Optics

Fabricability of large, high optial quality CaF_2 optics.

High-power optical coatings.

High quality cooled UV mirrors.

AVCO EVERETT

Although the conceptual design generated by this design study is based largely on demonstrated technologies, there are areas where some development is necessary. These are listed in Table 2. Most of these include extensions of demonstrated technology.

1.4 REPORT ORGANIZATION

The overall approach to system definition is presented in Section 2.1. Performance requirements are the basis for identification of system elements. Trade-offs associated with component selections are discussed. These trade-off studies stress low technological risks, high system reliability and long life. Baseline design parameters are developed.

The laser cavity is discussed in Section 2.2. Cavity dimensions are bounded by performance requirements. Distance between foils is related to gas density, gun voltage and foil material. Flow length is related to repetition rate, type of cathode and cavity aspect ratio. Gain length is related to laser extraction efficiency and beam quality. Pulse length is related to blue-green laser conversion, overall laser efficiency and fuel burnup. Implications of narrow line operation are discussed. These studies expand the technical basis for selection of baseline design parameters.

Foil performance is analyzed in Section 2.3. Results indicate that either conductive cooling or phase change cooling will meet performance requirements. Conduction cooling is preferred in the conceptual design since at present it represents the lower technology risk and higher system reliability. Pressure wave attenuation is discussed in Section 2.4. The detailed design of the muffler system will be based upon the results of DARPA flow technology programs conducted by Poseidon and AERL as well as theoretical predictions. The flow recirculation system is discussed in Section 2.5. Although there are no critical issues related to the flow loop, careful engineering design and precise flow and thermal control are indicated. Gas composition control is discussed in Section 2.6. Modeling of homogeneous gas chemistry provides theoretical lower bounds on scrubber requirements. Measurements of fuel burnup and of homogeneous and heterogenous reaction products will provide the basis for practical scrubber sizing. E-gun and pulse power considerations are discussed in Sections 2.7 and 2.8, respectively. Cold

18

cathodes are preferred for Phase I and IA operating conditions. However the system will be compatible with the future inclusion of thermionic cathodes. A conservative pulse power design is described which is aimed at addressing long life issues relevant to future Phase II requirements.

Optics design considerations in Section 2.9 were carried out for a smaller cavity volume of 10 liters. Concurrent system integration led to the selection of a larger system as described above. Since this updated design did not substantially impact the performance conclusion this rather detailed optics design was not updated. Issues relating to Raman conversion to the blue-green are discussed in Section 2.10. Here too the design concept is based on the smaller XeF cavity volume. The design approach is not altered when applied to the higher power XeF laser discussed above.

Scaling issues are presented in Section 3.0. The degree to which the XeF Integrator addresses high power and long run duration issues is assessed. Risk reduction experiments are recommended.

2.0 XeF LASER - CONCEPTUAL DESIGN DESCRIPTION

2.1 SYSTEM TRADE-OFFS AND OVERALL SYSTEM DESCRIPTION

This section presents a definition and general discussion of the approach to meeting the requirements for a strategic blue-green/excimer laser communication system integrator. A baseline system has been defined and the basic system and subsystem concepts are described together with alternative design approaches. The analytic methodology supporting these approaches and discussion of the critical subsystem issues and trade-offs are presented in the following sections.

In this section we present a brief system overview of the conceptual design. The architecture of the proposed design is driven by: (1) the requirement of overall XeF laser efficiency, beam quality and reliability; (2) the requirement of Raman conversion efficiency and blue-green beam quality; (3) the goal of using the integrator to help resolve critical issues related to the development of communications and weapon class devices.

The XeF laser is pumped by face-to-face e-beams. Conduction cooled foils separate the high-pressure laser cavity from the e-gun vacuum. The cross section of the active laser region is rectangular in shape with foils with a spacing of 14 cm. The foil apertures are 12 cm wide by 130 cm long. The resultant e-beam excited volume measures ~ 21.8 l. After exclusion of 1/2 cm thick boundary layers near the foils, a useful laser active volume of 20 liters remains.

The cavity will be operating from 300 to 450°K at densities from 2.0 to 3.6 Amagat of NF_3/Ne/Xe mixture. Using the baseline designed average pumping intensity and resonator optical configuration we project a cavity intrinsic efficiency of 4.5 percent with a collapsing diode (2 to 1 pump intensity variation during the pulse). The projected specific output energy is 7.5 J/l in a 1 μ pulse. Narrow line (< 0.5 A) operation is achieved by running the laser as an injection locked oscillator with an external narrow line injection laser.

The e-guns are designed to operate at 250 to 300 kV. Each e-gun cathode is fed by a single high-voltage bushing and an impedence matched transmission line by a separate PFN.

Magnetic guide field for the e-beam is provided by two water-cooled copper coils located outside the e-gun vacuum chambers.

The baseline reference pulse power system is made up of type E PFNs with voltage compensating networks to allow for time-varying load impedances. The PFNs use parallel plate oil capacitors for energy storage and the inductors can be changed to allow the output pulselength to be varied from 1 to 2 µs.

The PFNs are balance charged to $\pm$ the output voltage via resonant step-up transformers from intermediate energy storage capacitors. The PFNs are each switched by two, two-electrode air-blown 300 kV spark gaps. One of the gaps is triggered via voltage injection while the other is operated in the self-break mode. The PFNs are command charged from the intermediate energy store in 12 µs by parallel thyratrons.

The primary baseline acoustic concept utilizes close-in sidewall mufflers immediately upstream and downstream of the laser cavity to attenuate pressure waves generated by the e-beams. Suction in the upstream mufflers is used to control boundary layer growth along the straight upstream muffler walls. At the entrance to the upstream muffler section is a 3 to 1 contraction section and a diffuser is used downstream to provide pressure recovery.

The flow is generated by a variable speed adjustable pitch hydraulically driven vane-axial fan. This is located in the return leg of the flow channel. Fan noise is controlled by secondary acoustics mufflers located on the sidewalls near the fan. Flow thermal homogeneity is achieved by a downstream heat exchanger which takes out all the excess waste thermal energy and an upstream thermal stabilizer which provides temperature equilibration.

A small fraction of the flow is diverted to a scrubber which removes all non-noble gases from the flow. Pure NF_3 makeup is then provided downstream of the scrubber. This system will be capable of maintaining the loop gas composition within acceptable tolerances to allow continuous laser operation. A regenerative heat exchanger is used to condition entry and exit gas to the scrubber to minimize heater power. The entire flow loop is designed for minimum volume and loop head loss to minimize flow power.

A confocal unstable resonator with a magnification of 2.5 is employed. The resonator mirrors are water-cooled to allow continuous operation. The mirrors are external to the laser cavity. The temperature transition from $450°K$ laser cavity to room temperature can be taken across a vacuum or a stratified He filled tube outboard of CaF_2 windows.

The Raman converter system converts the XeF 351 nm output into the blue-green by two Stokes shifts in H_2. The Stokes shifts are achieved sequentially in two separate 6 atm room temperature H_2 cells. The cell lengths are minimized by using high pump intensity which is made possible by the use of uncoated windows. A separate Raman oscillator provides correlated first and second Stokes seed beams which are injected after spatial filtering into the two Raman cells. 1.3 x DL blue-green beam quality is achieved by injecting a near diffraction limited seed beam into the second Raman cell. The overall power conversion efficiency into the blue-green is expected to be over 30 percent with a factor of 2 time-varying XeF output pulse.

2.1.1 System Architecture and Engineering Trade-offs

During the past several years, under DARPA/ONR sponsorship, the physics of XeF lasers has been intensively researched. The key processes underlying XeF laser operation have been identified, and various important rates and cross sections have been calculated and measured. To date, this work has led to a reasonably complete understanding of this laser. Based on this understanding, a theoretical model has been constructed in order to predict laser performance. At Avco the model predictions have been checked with experimental results from 1-m laser devices. Substantial agreement has been obtained so that the ultimate performance of the large-scale versions of these lasers can now be projected with confidence. The best results obtained in XeF are summarized in Table 3. We have obtained intrinsic laser efficiencies of 5.5 percent and extracted specific energies of 14 J/1.

Under DARPA sponsorship and IRAD programs, Avco has investigated key technologies that are essential for the operation of closed-cycle repped lasers. These include experimental verification of:

- Base flow and acoustic clearing that are consistent with obtaining a near diffraction limited beam from a repped laser.

TABLE 3. SUMMARY OF HEATED XeF LASER RESULTS

–	Gas Mixture	Ne/Xe/NF$_3$	
–	Temperature	450 °K	
–	Pressure	3 Amagat	

● LASER PERFORMANCE

–	Intrinsic Efficiency	5.5 percent	5.0 percent
–	Specific Energy	5.4 J/1	14 J/1

● E-BEAM CHARACTERISTICS

–	Beam Current Density	8.5 A/cm^2	14 A/cm^2
–	Beam Energy	250 kV	250 kV
–	Pulselength	0.7 μs	1.6 μs

- Thermionic cathodes operating up to 20 A/cm^2 which is consistent with the requirements for XeF lasers.
- Further we have investigated the homogeneous and hetrogeneous chemistry of the laser mixture in sufficient detail to be able to identify compatible materials and scrubbing techniques that will allow continuous closed-cycle operation.
- Avco has been conducting Raman experiments using XeF lasers as the pump and H_2 as the converting gas since FY79. Initial experiments utilized a 10 mJ, 10 ns commercial UV-preionized discharge device. Conversion of this pump radiation to first Stokes output at energy efficiencies of 44 percent were observed. Due to the triangular temporal pulse shape of the pump, this corresponded to ~ 66 percent power conversion and permitted a realistic projection for a two-cell, two-step conversion of > 40 percent to the blue-green. Later experiments were performed with a 1-m e-beam excited XeF laser as a pump. Fitted with unstable optics, this device produces ~ 3 J in 400 ns at near diffraction limit. Raman conversion experiments carried out with this device showed 30-35 percent conversion to the blue-green in a single cell using a focused beam and ~ 60 percent conversion to first Stokes in a single cell using a collimated beam. These experiments are continuing with emphasis on beam quality issues. Also, additional single cell collimated beam Raman experiments are planned which will utilize the full aperture output beam of the 3-m XeF scale-up device. Upon completion, these experiments will have demonstrated significant energy conversion in a large aperture Raman cell and establish the feasibility of this approach to reach the required energy levels for the mirror satellite, submarine laser communications concept.

In summary, the XeF integrator has been designed with the following objectives:

- To meet all integrator requirements.
- Wherever practical to use technologies that are scalable to communications applications.
- To resolve many key technological issues that pertain to large-scale XeF lasers.

2.1.1.1 System Architecture

The system architecture is largely driven by device requirements, which are shown in Table 4. These requirements have resulted in the selection of the baseline concept which incorporates an injection locked XeF cavity e-beam pumped from two sides with a two stage Raman conversion process. The requirements that most strongly impacted this concept selection are discussed below.

- Linewidth of < 1 A in the blue-green. This implies that the XeF laser linewidth be < 0.5 A. To accomplish narrow line operation requires that the XeF laser be an injection locked oscillator.

- Beam quality of 1.3 times diffraction limited beam in the blue-green. As a result of this requirement, a two-stage Raman conversion approach becomes attractive. From a preliminary Avco IRAD analysis it is apparent that the beam quality of the Raman-shifted laser depends only on the injected signal and not on the pump. Hence, we are not concerned about the beam quality of the emerging first Stokes from cell 1, which is the pump for cell 2. Instead, we inject a beam of good quality into the 2nd cell to obtain the desired blue-green output.

- We will also meet the requirement of a 1.3 times diffraction limited beam out of the XeF laser.

- Reliability, good beam quality, and long run durations have led to a 1 μs, 7.5 J/1 design of the XeF laser. However, the 1 μs pulse length is also advantageous to the Raman cell design, since the Raman conversion into the blue-green is flux dependent. Hence, to keep the conversion cells short, one would like to go to high fluxes. This in turn requires short pulse lengths if one wants to remain below the threshold for damage to optical components. The shorter pulse length also results in a lower foil loading, which is necessary for lifetime and efficiency. However, the construction of a large XeF laser drives the design to longer pulses because it makes for a more compact and efficient design. These conflicting requirements are resolved in favor of the 1 μs pulse length. However, to verify the higher energy density operation of the XeF laser, the PFN will be operated with minor modifications with a 2 μs pulse.

26

TABLE 4. XeF INTEGRATOR DESIGN REQUIREMENTS

REQUIREMENTS	XeF	BLUE—GREEN
PULSE ENERGY	$\geq$ 100 J	30 J
PULSE LENGTH	$\geq$ 1 μ sec	SAME
AVERAGE POWER	> 10 KW	> 3 KW
REPETITION RATE (AVERAGE)	$\geq$ 100 pps	SAME
RECOVERY TIME (FOR PULSE INTERVAL MODULATION)	$\leq$ 5 msec	SAME
RUN TIME	$\geq$ 1 min continuous	SAME
DUTY CYCLE (DOWN TIME, ETC.)	5 ten sec runs/day 2 one min runs/month	SAME
BEAM QUALITY	$\leq$ 1.3 *times* Diffraction Limit	SAME
BANDWIDTH	—	< 1 $\overset{o}{A}$
BEAM INTENSITY UNIFORMITY (NEAR FIELD)	$\pm$ 25% OF AVERAGE INTENSITY	SAME
OPTICAL LENGTH	$\geq$ 50 cm	SAME

NOMINAL OPERATING PARAMETERS

COMPONENT EFFICIENCIES		
PFN	$\geq$ 50%	SAME
E—GUN	$\geq$ 50%	SAME
CAVITY	$\geq$ 4.5%	SAME
RAMAN CELL		> 30%
WAVELENGTH	351 nm	450—520 nm
OVERALL SYSTEM EFFICIENCY	$\geq$ 1%	
CAVITY GAS		
TEMPERATURE	300—450°K	
DENSITY	2.0 — 3.6 amagat	

K2897

$\mathscr{A}$AVCO EVERETT

- At the e-beam energies required, it is difficult to obtain the required e-beam efficiency of > 50 percent with phase transition cooling. Therefore, a single conduction cooled foil approach is necessary to meet the e-beam and system efficiency requirements. The lower foil loadings at 1 μs facilitate this concept.
- Because cold cathodes are more rugged and easier to implement than thermionics, we are using cold cathodes. However, the laser system will be designed to be compatible with thermionics.
- Clearly it will be possible to run other excimer lasers in the facility. The most probable choice is KrF* which radiates at 250 nm. In fact a double shift of KrF* through the two Raman cells will result in a 315 nm laser. Such a laser could be used for atmosphere propagation experiments. Another advantage of using KrF* is that it will not require that the cavity and flow loop be thoroughly cleaned when one wished to return to running with XeF.
- Adaptive optics techniques required for the uplink phase of the communications link.

2.1.1.2 System Engineering Integration

The following discussions describe some of the major design interactions which must be integrated with the various laser subsystems and translated into design requirements. The total system has been divided into eight convenient subsystems: (1) Laser Cavity, which includes the e-beam assembly and foil; (2) Acoustic Suppression, which includes only the XeF laser requirements; (3) Optics-Resonator, which includes analysis of the resonator design, optical injection, mirrors and windows necessary to achieve the required beam quality; (4) Raman Conversion, which includes the optical configuration as well as the flow and acoustics design; (5) Gas Recirculator, which includes only the XeF gas flow system, and the Gas Processor, which includes the flow and purification elements necessary to clean up the XeF laser gas contamination; (6) Power Supply and Conditioning, which includes the power source as well as the voltage charging and pulse forming networks; (7) Controls and Instrumentation, which includes the operational requirements including data acquisition and

display as well as the fault protection system; and (8) Diagnostics, which includes the laser performance and laser beam diagnostics. All but the last two (which pervade many other subsystems) are depicted on the laser subsystem block diagram of Figure 3 which shows the interrelationships of the various subsystems and some of their key elements.

The design requirements for each of these subsystems stem from the optical requirements for either the XeF laser or the Raman shifted blue-green output. Some of the interacting trade-offs which must be considered include the following.

Cavity Dimensions. The selection of the cavity dimensions is very critical, since they determine many key technology parameters such as window loading, foil loading, e-beam efficiency, extraction efficiency, flush factor, and flow rate, all of which impact either performance or beam quality.

Flow Loop. The size of the XeF flow loop and corresponding pressure loss establishes the fan power requirement. This in turn affects the overall system efficiency, and hence could impact the efficiency budget for other subsystems.

E-Beam Voltage. The e-beam voltage affects the cavity e-beam deposition uniformity, the e-beam efficiency, the foil loading, the cathode design, and the PFN design.

Resonator Magnification. Selection of the resonator magnification is critical because it strongly impacts the laser efficiency and beam quality.

Cavity Pump Rate. The cavity pump rate is important, because it essentially sizes the cavity volume. Since small sizes are economically desirable, high pump rates are desirable. However, high pump rates can also lead to higher window and foil loadings (at constant PRF and pulse width) which degrade either beam quality or life or both.

Medium Homogeneity. This parameter represents a critical flow technology area which strongly affects beam quality.

Pulse Width. The pulse width selection affects the PFN/cathode design and efficiency, and also directly impacts the foil and window loadings. Short pulse widths are primarily beneficial in these areas as well as in the Raman cell.

29
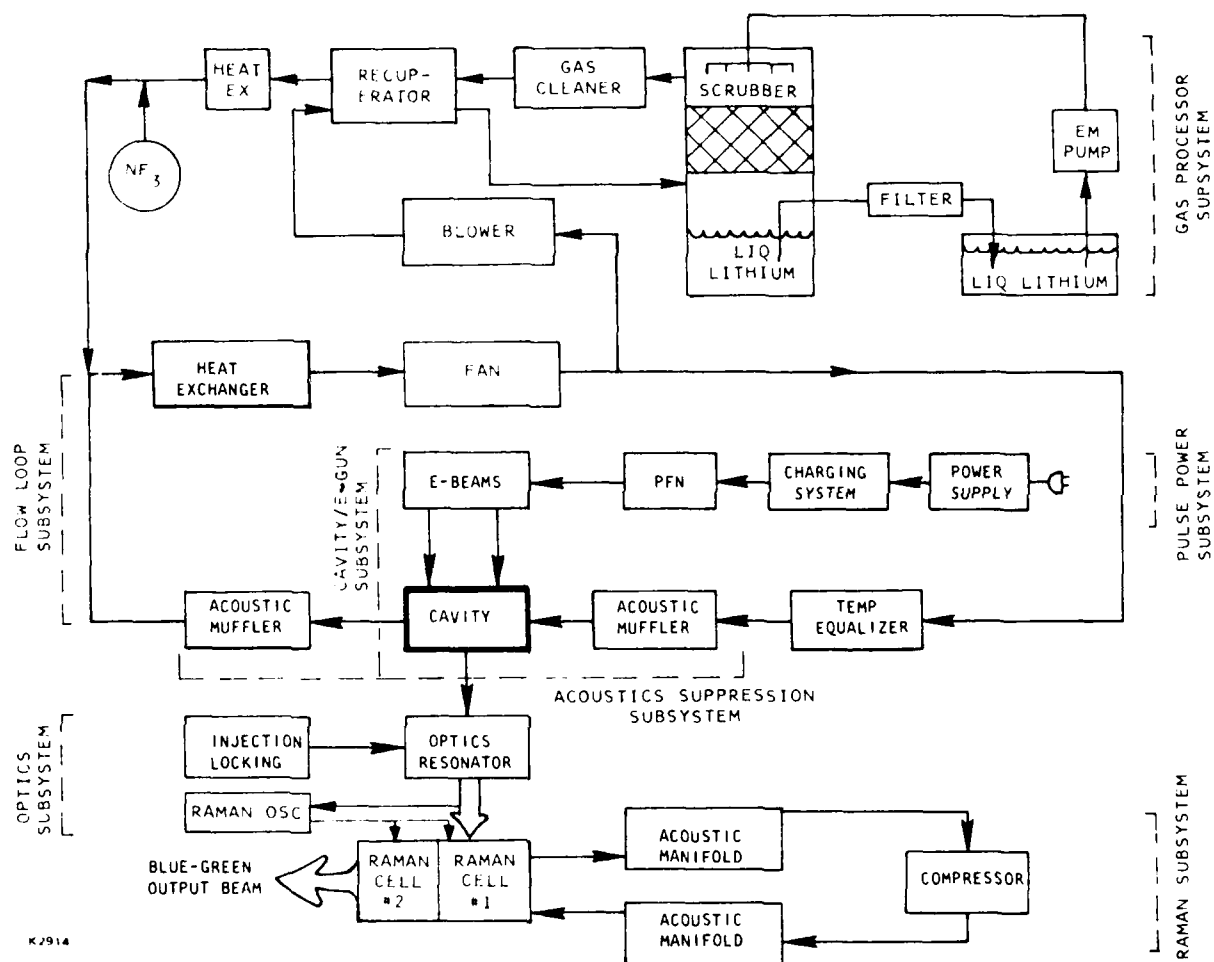
Figure 3.   Integrator Subsystem Block Diagram

30

Window Design. The selection of the window material, design, and location strongly impacts the beam quality budget, and hence the technology requirements for other areas such as medium homogeneity, or the cavity geometry and resonator magnification.

Raman Cell Concept. The selection of the Raman cell concept (uncoated high intensity, high loss optics or coated low intensity, low loss optics) directly affects the system efficiency, but it also impacts the beam quality. The high loss approach results in short cells which have easier medium homogeneity requirements, while the low loss approach results in longer cells which require significantly more difficult flow homogeneity technology. This tradeoff decision is also strongly dependent upon development testing to demonstrate the predicted beam quality cleanup characteristics of the Raman process. If cleanup is corroborated, longer, lower loss designs become more feasible.

The foregoing trade-offs are just some of the many system interactions which must be considered in a total system design.

2.1.1.3 System Engineering Trades

Given the UV laser intrinsic efficiency requirements, it is now necessary to address the cavity sizing relationships required to produce such efficiency and their impact on the UV laser beam quality. The significant trade-off variables are the cavity pump rate (S, kW/cc), the resonator magnification (M), and the cavity geometry (L_{opt} and a, mirror side dimension). It will be shown later that a nearly square aperture is most desirable from a beam quality standpoint, and hence the following analysis will be based upon a square mirror.

The active cavity volume (Vol., liters) is defined by the output power required (Power, kW), the cavity pump rate (S, kW/cc), the intrinsic efficiency (η_{IN}), the pulse width (τ_p, μs), and the pulse repetition frequency (PRF, Hz) according to the following relationship:

$$\text{Power} = S \times \text{Vol} \times \eta_{IN} \times \tau_p \times \text{PRF}.$$

31

In addition, the intrinsic efficiency is related to the medium efficiency (η_m) and the extraction efficiency (η_{ex}) as their product:

$$\eta_{IN} = \eta_m \times \eta_{ex},$$

where the medium efficiency represents the maximum laser energy available for extraction, and the extraction efficiency is dependent upon the cavity optical length, small-signal gain and resonator magnification (output coupling).

Preparatory to any system parametric trade-off analysis, it is necessary to obtain the basic laser kinetics parametric performance. These parametrics (involving medium efficiency and small-signal gain as a function of pump rate) were developed from Avco kinetics modeling and test data for broad band laser output. The performance for narrow line operation has not yet been experimentally verified and hence an analytic estimate was made for anticipated hot cavity injection locked performance. The Chernin-Moore-McCarthy resonator extraction efficiency model[1] was used to calculate extraction efficiency as a function of magnification, small signal gain, gain length, and gain-to-loss ratio. An effective gain-to-loss ratio of 15:1 including both medium and optics losses was assumed.

The desire for a low cost demonstrator system implies a minimum power device. However, the system efficiency and beam quality requirements place some lower bounds upon the size. For instance, the e-beam separation distance cannot be made arbitrarily small since the e-beam efficiency drops drastically at the size approaches 10 cm. The optics beam quality requirement for square apertures then fixes the flow dimension, which then leaves only the optical path length to be determined. This parameter, together with the resonator magnification, establishes the extraction efficiency, and hence there is little latitude in the selection of L optical. The resultant cavity produces 15 kW of power rather than the minimum requirement of 10 kW. Sizing and technology trade-offs have been carried out and results are summarized in a baseline design in Table 5.

1.   Chernin, David P., "Optical Extraction Efficiency in Lasers with High Fresnel Number Confocal Unstable Resonators," Applied Optics, Vol. 18 No. 21.

TABLE 5. INTEGRATOR BASELINE DESIGN CHARACTERISTICS
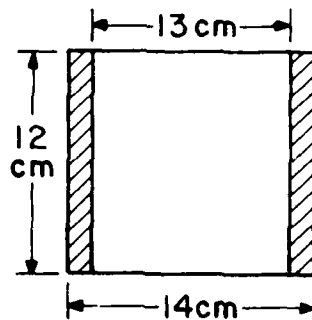
Active 13 x 12 x 130 cm
Overall 14 x 12 x 150 cm
20.3 liters active volume
152 J/pulse 7.5 J/liter

Output power;   4.5 kw blue-green
Output power;   15.2 kw X_eF

g_o = 2.54 %/cm g_oL = 3.3

g_o / α_o = 15   Magnification = 2.5

η_{INT} = 4.5% $\eta_{Pulse\ Shape}$ = 90%

Pump Rate = 166.7 kw/cc
3.5 Amagats   450 k
100 Hz   1.0 μsec

Mach No. = 0.086
Flush Factor = 2.0 (200 Hz), 4.0 (100 Hz)

V_{EB} = 250 kV J_{EB} = 10.0 A/cm^2

Foil Loading = 37.6 w/cm^2
Window Loading = 116 w/cm^2

Beam Quality < 1.3

Raman Cell	Cell No. 1	Cell No. 2
Pressure	5.8 atm	5.8 atm
Length	315 cm	240 cm
Aperture	3.6 x 3.3 cm^2	2.56 x 2.36 cm^2

K2974

33

The XeF laser is driven with two e-beams because this improves the over-all efficiency. Large XeF laser systems will also require two e-beams, hence the configuration chosen is scalable. We have designed an injection laser for XeF to insure narrow line operation, and the 351 nm output from the XeF laser is pumped into the first hydrogen cell. The first Stokes output from cell number one is then pumped into the second hydrogen cell. Both Raman cells have injection lasers for reasons discussed earlier.

Table 5 shows the XeF output power is 15 kW, with 4.5 kW produced in the blue-green. The basic XeF cavity has foil walls separated by 14 cm, with an e-beam height of 12 cm. The optical path length is 130 cm with an overall length of 150 cm allowing for a 10 cm setback at each window. Raman cell lengths are 315 and 240 cm, respectively.

This system meets all the design requirements and provides a 1 percent overall system efficiency out of the XeF laser. The basis for this system efficiency is given in Table 6.

TABLE 6.   OVERALL LASER EFFICIENCY

XeF OUTPUT	15.21 kW
BI–Gr OUTPUT	4.56 kW
ELECTRICAL EFF	
PFN	0.78
E–BEAM	0.50
PULSE SHAPE	0.90
VOL EFF	0.93
EL SCAT EFF	0.92
INTRINSIC EFF	0.45
XeF ELEC EFF	1.36 PERCENT
XeF ELEC POWER	1118 kW
AUXILIARY POWER	
FLOW	129 kW
MISC.	230 kW
TOTAL XeF SYS POWER	1477 kW
OVERALL XeF EFF	1.03 PERCENT
RAMAN CONV EFF	0.3
RAMAN AUX POWER	15 kW
TOTAL BI–Gr SYS	1492 kW
OVERALL BI–Gr EFF	0.3 PERCENT

K2981

35

2.2 LASER CAVITY

During the past several years, under DARPA/ONR sponsorship, the physics of XeF lasers has been intensively researched. The key processes underlying XeF laser operation have been identified, and various important rates and cross sections have been calculated and measured. To date, this work has led to a reasonably complete understanding of this laser. Based on this understanding, theoretical modeling has been conducted at Avco to predict laser performance. The model predictions have been checked with experimental results obtained from 1-m laser devices. Substantial agreement has been obtained so that the ultimate performance of large-scale versions of these lasers can now be made with confidence. In this subsection we will use our understanding of the laser to determine the laser dimensions for the XeF integrator.

The main objectives are:

- To obtain a near diffraction limited 3 kW blue-green laser
- To resolve many key technological issues that pertain to large-scale XeF lasers.

2.2.1 Laser Dimensions and Kinetic Constraints

Optimization of laser dimensions requires consideration of a number of important issues. One can begin with the realization that the laser kinetics and intrinsic absorption processes essentially determine the optimum laser mixture, the total pressure or density, and the temperature. They also place constraints on the e-beam current density and pulsewidth. Typically, mixtures are 99.3 percent Ne/0.5 percent Xe/0.2 percent NF_3 at a total density of 3-4 amagats, and a temperature of $450°K$. For such mixtures, an e-beam current density of 10 A/cm^2 and a pulsewidth of 4 μs is possible for NF_3 depletion considerations. With a pulse length of 4 μs, over 70 percent of the NF_3 is predicted to be consumed by the end of the laser pulse. Adding larger amounts of NF_3 leads to difficulties with interception in the formation kinetic channels, and larger current densities can lead to significant quenching of XeF* by electrons. The 4 μs pulse duration, which in itself is a significant advance, was made possible by virtue of the Avco thermionic e-gun development which obviates the previous cold cathode/diode closure limit. Consideration must and will be given to the fact that thermionic cathodes may not be

sufficiently advanced for use in the initial device. However, because of the many advantages offered by thermionic cathodes, the system will be designed such that thermionic cathodes can be installed at a later time.

For a simple rectilinear cavity as shown in Figure 4 one has first to determine the laser volume and the corresponding three dimensions. We are required to deliver energies in excess of 10 kW at 100 Hz. As we will see subsequently, in order to obtain a 1.3 times diffraction limited beam with an overall efficiency of > 1 percent, the XeF laser has to deliver 15 kW. Allowing for a volumetric efficiency of 93 percent because of boundary layers along the walls, the device should be capable of delivering 16.2 kW. Hence, the single pulse energy will be 162 J. To determine the volume one now has to establish the energy density that the device is to work at. Because of foil cooling constraints and reliability we have chosen 7.5 J/liter. Hence the laser volume is 21.6 liter. We will now determine the laser dimensions.

The distance between the e-beams will depend on:
- Laser gas density
- E-beam energy
- Foil material and foil cooling method.

As we have stated previously, typical XeF laser mixtures contain > 99 percent of Ne, about 0.5 percent Xe and 0.1-0.2 percent NF_3 at a total density of about 3 amagats and a temperature of 450°K. The reason one chooses these conditions is that the XeF laser optimizes for such a density, mixture ratio and temperature. In Figure 5 we see a plot of the laser output from the Avco 1-m device as a function of the mixture density. The laser output optimizes experimentally and theoretically around 3-4 amagats. Having established the laser mixture density, the distance between the e-beams will depend on the fast electron energy and the foil material and thickness.

Electron scattering is caused by the coulomb field of the nucleus and hence depends on the square of the nuclear charge. The fast electrons lose energy because of inelastic collisions with orbital electrons. This loss rate is given by the Bethe stopping power. Both the elastic scattering and energy loss of the fast electrons depend on their energy. Hence the penetration of the electrons into the laser mixture will be energy dependent.
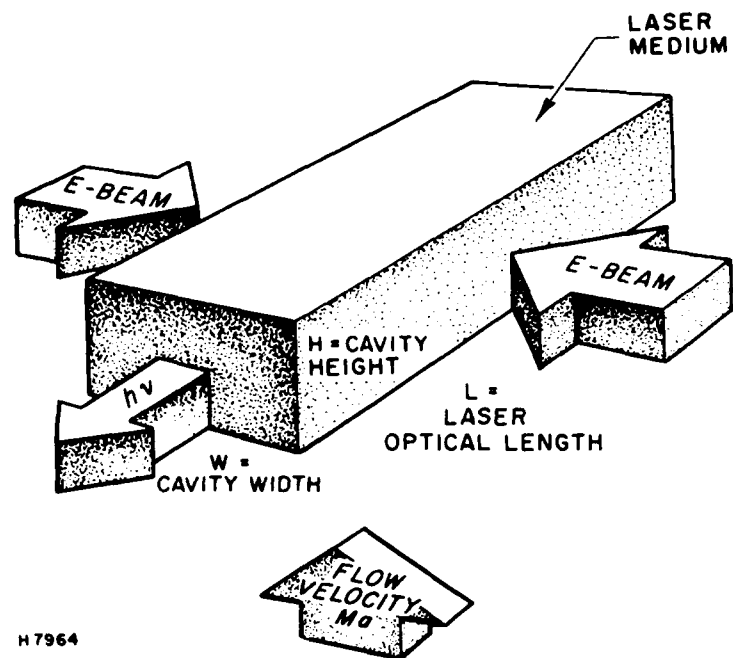
Figure 4.   Repped Laser Geometry
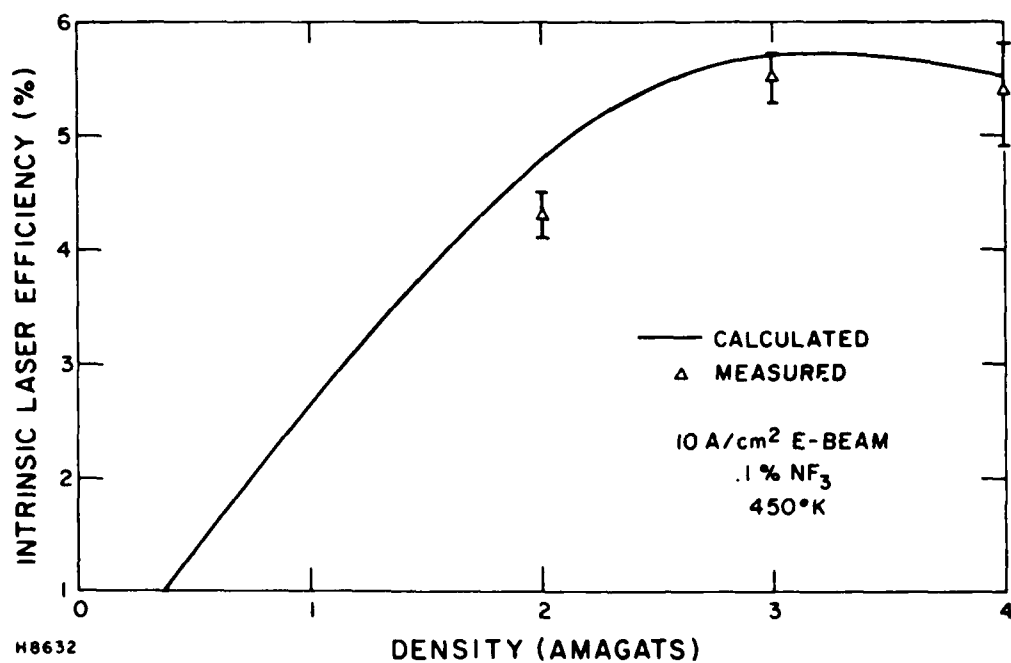
Figure 5.   Intrinsic Laser Efficiency vs. Density

38

Another factor to consider in determining the range of the e-beam deposition is that, utilizing standard Avco designs, the electrons are constrained from diffusing out of the optical volume by an applied magnetic field. This applied magnetic field serves a number of functions:

- It prevents the e-beam from pinching under the influence of its self-magnetic field,
- by inhibiting the diffusion of electrons outside the optical volume, the overall electrical efficiency of the laser is increased.

The self-magnetic field is largest at the edge of the e-beam. For a maximum diode current density of 13 A/cm^2, this field will be 190 G for the device under consideration. Hence, an applied field of 2 kG should be adequate to eliminate the self-field beam pinching. The choice of the applied magnetic field is determined by several other factors which will be discussed later in the section.

The energy dependence of the electron range for an XeF laser mixture is shown in Figure 6 which is a semi-log plot of the distance between the e-beams as a function of the initial e-beam energy. This applies for a foil of 1/2 mil Ti clad with 1/2 mil Al. One advantage of using two e-beams is that 90 percent e-beam energy can be deposited in the optical volume. Using a single e-beam, only 70 percent of the beam energy can be deposited in the optical volume. The reason for this is apparent if one looks at Figure 7 which shows the e-beam deposition by each beam and the total deposition. If only one beam is used and the deposition across the laser cavity is to be relatively uniform, then 30 percent of the beam energy could be lost. When two e-beams are used, however, this last 30 percent can be used. So the distance between the e-beams should be ~ 14 cm for the present design.

The choice of the e-beam height is determined by the following considerations:

- Aspect ratio
- Repetition rate
- Type of cathode

Because of beam quality consideration an aspect ratio of unity, i.e., a square aperture is desirable. As the distance between the e-beams is 14 cm this says that we would like an e-beam height of 12-15 cm. For such an e-beam height
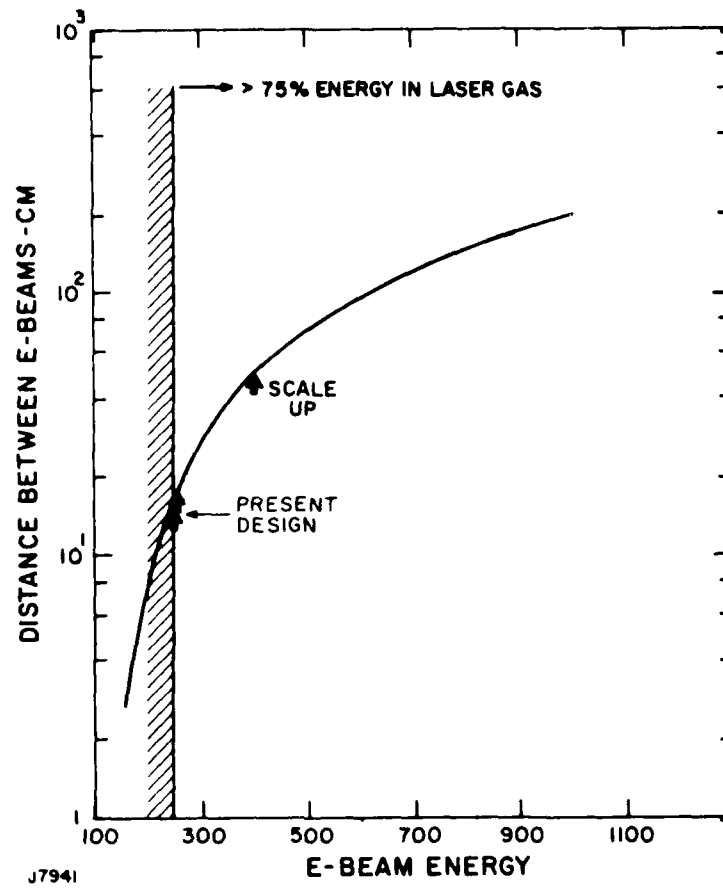
Figure 6.   Distance Between E-Beams vs. E-Beam Energy
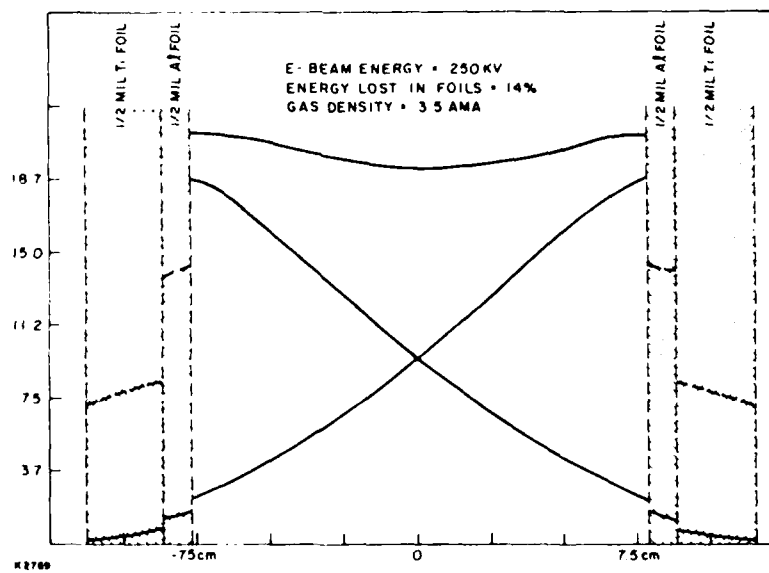
Figure 7.   Transverse Energy Deposition in Laser Cavity

40

and the present flow technology we see no issue to achieving the required flow clearing of 5 ms. Hence we have to determine if an e-beam height of 12-15 cm is consistent with the choice of cathode and applied magnetic fields.

The application of a magnetic field is, of course, to improve the efficiency of the XeF laser. To insure that we deposit $\geq$ 90 percent of the post foil energy in the optical volume we require a certain minimum magnetic field. This minimum magnetic field is determined by the diffusion across the field lines. The diffusion length, L_D, across the field lines is given by the square root of the age.

$$L_D = \left\{ \int_0^W dw \frac{\lambda}{3 \times (1 + \lambda^2/r_1^2)} \right\}^{1/2}$$

where x is the Bethe stopping power, λ is the transport mean free path and r_1 is the Larmor radius. For > 90 percent of the energy to be deposited in the active volume we require $H/L_D > 5$, where H is the e-beam height.

Figure 8 shows a plot of the e-beam height vs. the applied magnetic field for e-beam energies of 200, 250 and 400 kV. From these curves it is clear that at an e-beam height of 12 cm and an e-beam energy of 250 kV, the required magnetic field must be $\geq$ 1.5 kG. Clearly, as the magnetic field is increased, the volumetric efficiency is increased. However, we cannot increase the magnetic field arbitrarily because the electrical power increases as the square of the B-field and we initially plan to use cold cathodes. As the B-field increases with the use of cold cathodes, the pulse length one can use decreases. This issue will be addressed later in this section.

The choice of the gain length is determined primarily by the following constraints:

- High extraction efficiency
- Good beam quality which implies a large magnification
- An active volume of about 20 liters to insure single-pulse energies of 100-150 J at 100 Hz

41
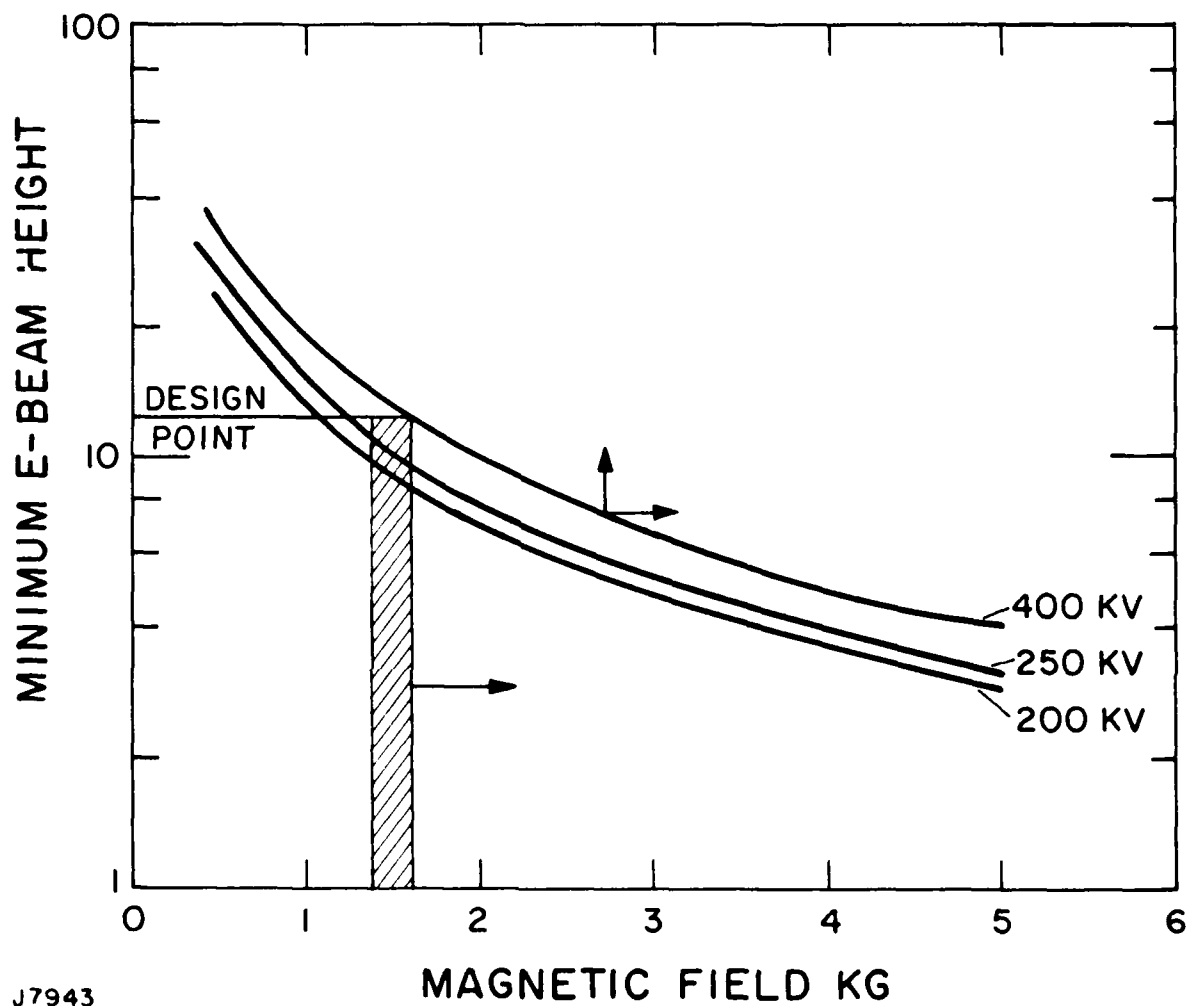
Figure 8.   Minimum E-Beam Height vs. Magnetic Field

We, of course, require that the laser length is > 50 cm. For beam quality considerations we want the magnification M and output coupling T to be as large as possible. As will be discussed in the optics section, we can achieve a 1.3 x DL beam with a M of 2.5, which corresponds to T of 84 percent. We are required to obtain an extraction efficiency of > 4.5 percent. As we will discuss in the following subsection the pulse length is 1 μs and the e-beam pump intensity 167 kW/cm^3. For such a pump intensity the Avco kinetic code predicts a small-signal gain of 0.025 cm^{-1}. For such a small-signal gain we can achieve the required intrinsic efficiency of 4.5 percent with a gain length of 130 cm.

2.2.2 The Pulse Length

The pulse length of the XeF laser is determined by the following criteria:

- Blue-green laser conversion
- Type of cathode
- Magnetic field compression
- Fuel burnup

From the Raman conversion point of view one would like as short a pulse as possible. This is because the Raman gain is flux dependent and damage to optical components is energy dependent. Since the specification of the RFP requires pulse lengths of $\geq$ 1 μs, we have designed the XeF laser for a 1 μs pulse length. From a weapons point of view one would like a long pulse length primarily because of efficiency and cost considerations. Hence we have specified that the PFN shall be operable also at 2 μs, thereby addressing the longer pulse higher energy density issues.

Another reason for choosing the shortest pulse possible is because we are initially operating the device with a cold cathode. Cold cathodes exhibit the phenomenon of diode collapse. If we wish to keep the e-beam voltage constant then a collapsing diode results in an increase in current and consequently an increase in the pump power as a function of time. Such a situation is unattractive because it means that it cannot operate at optimum conditions and both the XeF laser and the Raman conversion efficiency suffer.

Figure 9 shows the operating region that is available for a 1 μs pulse assuming a diode collapse of two, i.e., the e-beam current density and hence the power varies by a factor of two during the pulse. The reason we have chosen a collapse of two is that a flux variation of two will allow one to obtain the required 30 percent conversion efficiency into the blue-green. From Figure 10 it is clear that at the design voltage of 250 kV and mean current density of 6.2 A/cm^2, the closure velocity should be 1.7 cm/μs. At Avco we have investigated the closure velocity as a function of the applied magnetic field. The results are shown in Figure 10. From this figure one sees that at the design region of 1.5-2 kG the closure velocity lies between 1.5-2 cm/μs.

2.2.3 Free-Running Laser Issues

The key kinetic issues of a free-running e-beam pumped XeF laser are shown schematically in Figure 11. For efficient laser operation, four criteria have to be met:

- The upper laser levels should be formed efficiently.
- The quenching by heavy particles and electrons should be sufficiently slow.
- The active medium absorption should be much less than the gain. Further, the absorption length should be less than unity.
- Finally, the lower level should be removed rapidly.

The XeF laser satisfies all four criteria. By e-beam pumping, the upper laser level is formed mainly by ionic recombination. The cross-section for such a process is, of course, coulombic and hence large. As a result, the upper laser level forms rapidly and efficiently. The XeF upper level has a degeneracy. These states are commonly called the XeF(B) and XeF(C) states. The juxta position of these states in relation to one another has been a very controversial subject. Suffice it to say that at Avco we have experimentally shown that all the energy in the C-state can be accessed by the laser photons.

Once the upper laser level has been formed, one would like to extract the photons efficiently. To achieve this, one must insure that the probability of stimulating the XeF* is much larger than the combined probability of radiative decay and collisional quenching. For the XeF laser under typical operating conditions, the probability of stimulating the XeF* is three to four times that of losses by spontaneous decay and quenching.

44
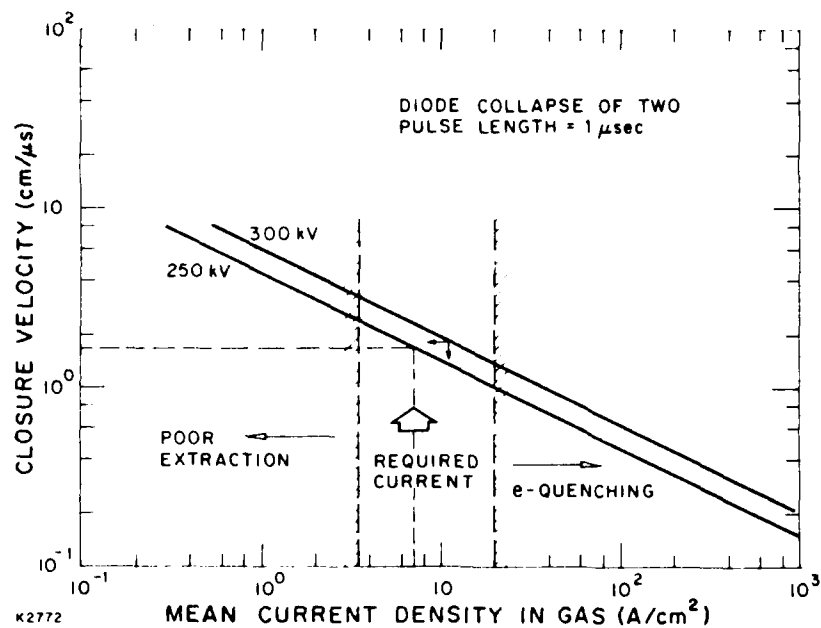
Figure 9.   Mean Current Density in Gas (A/cm²)
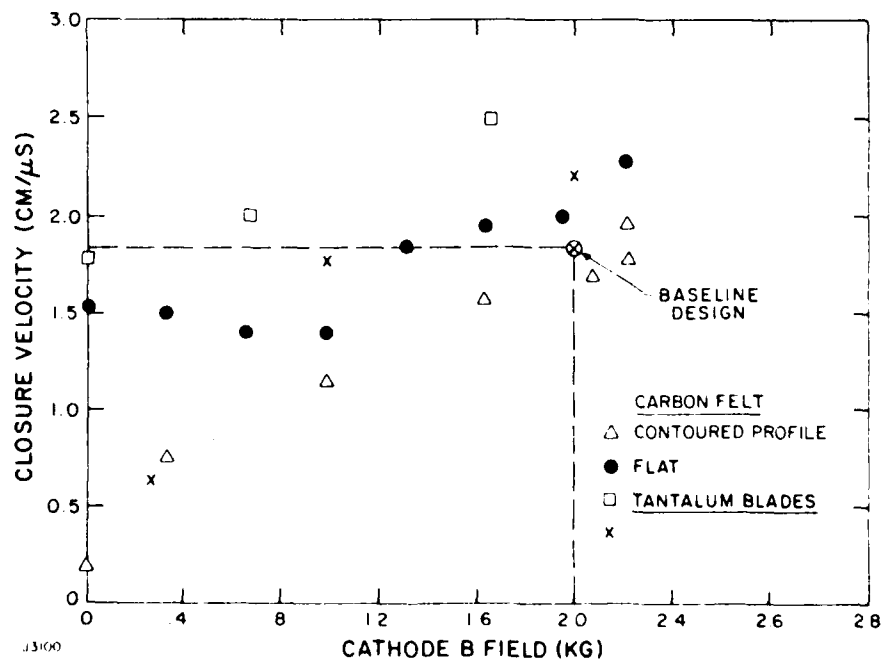
Figure 10.   Felt Cathode Closure vs. Magnetic Field

45
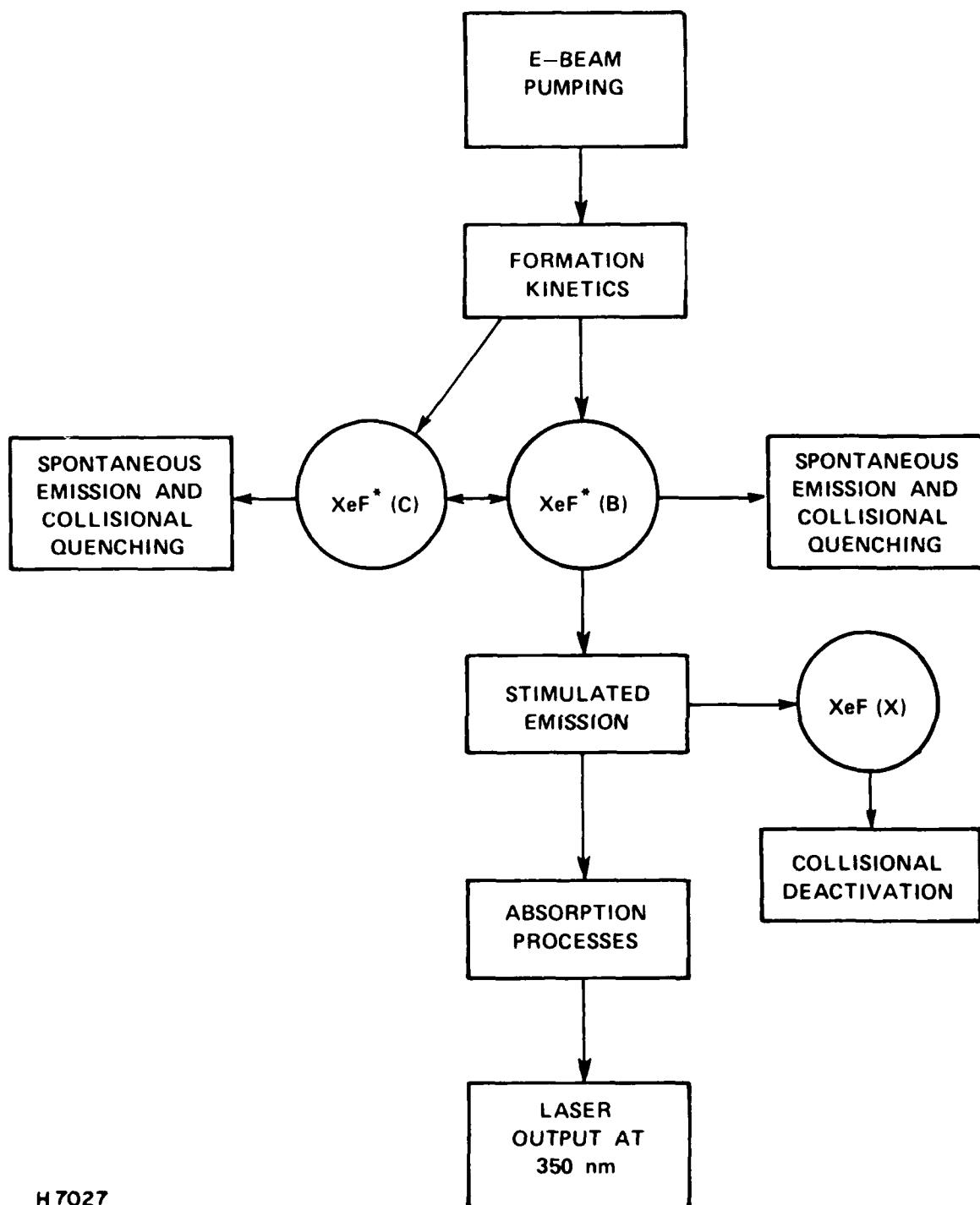
Figure 11.   Key Issues in XeF Lasers

H 7027

46

The active medium absorption in XeF has been measured at various laboratories in the U.S. These measurement have produced small-signal gain to loss ratios in the 15-20 range with varying techniques. Because the absorption in XeF is small the uncertainties in these measurements are often large. In order to provide a conservative design and allow some margin for safety the intrinsic efficiency projections will be based on a medium gain to loss ratio of 15.

Finally, the lower level of XeF dissociates rapidly enough at elevated temperatures that "bottlenecking" has less than a 5 to 10 percent impact on laser efficiency.

All of the above understanding obtained by early kinetics and laser experiments at Avco, NRL, and elsewhere supported optimism for aperture, length, and pulse width scaling of efficient free-running XeF lasers to high energy and led to the successful Scale-up demonstration experiment at Avco.

2.2.4 Narrow Line Extraction

The SLC mission requires not only high intrinsic efficiency (> 4.5 percent) but also narrow linewidth ($\leq$ 0.5 Å) for the XeF Raman driver in order to achieve 1 Å bandwidth in the visible (~ 496 nm). The linewidth requirement at the specified power level virtually assures the necessity for injection locking, and introduces practical issues listed in Table 7. Experimental data related to the practical issues are scarce and inconclusive but provide some useful indications summarized immediately below.

The available data on injection locking characteristics of XeF discharge lasers[2,3] provide some useful information in spite of the fact that the spectral details appear to be somewhat inconsistent and quantitative narrow-line extraction efficiency data are lacking. The experiments of Goldhar, et al.,[2] support the assumption of rotational equilibrium within

2.   Goldhar, J., et al., "Injection Locking of a Xenon Fluoride Laser," Appl. Phys. Lett. 31, 677 (1977).

3.   West, J.B., et al., "Efficient Injection-Locking of an E-Beam-Excited XeF Laser," J. Appl. Phys. 52, 5383 (1981).

TABLE 7. KINETICS RELATED NARROW—LINE EXTRACTION ISSUES

- INJECTION λ FOR BEST η_{INT}

- ACHIEVABLE η_{INT} @ $\Delta\lambda < 0.5\overset{\circ}{A}$

- ACHIEVABLE η_{INT} @ $\Delta\lambda < 1\ \overset{\circ}{A}$

- ACHIEVABLE η_{INT} vs $\Delta\lambda$

- SENSITIVITY TO MEDIUM CONDITIONS
  (S, ρ, T, MIX)

- INJECTION POWER REQUIREMENT

- INJECTION PULSE LENGTH REQUIREMENT

- SUPPRESSION REQUIREMENT FOR COMPETING λ's

K2917

◢◢AVCO EVERETT

a v' level even at the relatively low density of 1 amagat of argon. Hence, the assumption of full rotational equilibrium for 3- to 4-amagat Ne mixes should not be an issue. This room temperature experiment also shows that the V-T coupling between v' = 1 and v' ≈ 0 is slow because of the failure to suppress (1-4) emission with 353-nm (0-3) injection and because of the low estimated narrow band to free-running efficiency ratio of ~ 50 percent for injection at either 351- or 353-nm. Bigio et al.,[4] also infer a degraded narrow to free efficiency ratio (~ 60 percent) in 2 atm He diluent at room temperature. However, the efficiency performance details are clearly not relevant to conditions appropriate for efficient e-beam pumped lasing (3- to 4-amagat, Neon, 400- to 500-°K) because of significant differences in the B-state pumping, quenching, and vibrational relaxation.

Recent room-temperature e-beam-pumped 353-nm injection-locking experiments[3] have demonstrated narrow-line extraction (< 0.5 cm^{-1}) on the (0-3) transition with > 90 percent of the free-running broadband 353-nm efficiency (typically $\leq$ 2.5 percent). This result implies a high degree of rotational equilibrium which is a necessary condition for efficient narrow-line extraction. It was also shown that injection on a weak laser spectral feature at 351 nm attributed to (1-2) lasing (but probably (1-4) + (0-2) lasing) did not significantly depress the 353 nm lasing. This result is not surprising since the (0-2) peak stimulated emission cross section at 351 nm is about a factor of two lower than that of the (0-3) at 353 nm and since the cold (1-4) inversion is basically low and further depressed by (0-3) lasing.

Efficient narrow-line extraction near 351 nm in e-beam pumped systems is really only plausible at elevated temperature. But hot injection experiments have not yet been performed for conditions where the highest free running efficiency (η_{INT} ~ 5.5 percent) is achieved with comparable extraction at both 351- and 353-nm. Under these conditions, achieving η_{INT} > 4.5 percent

---

4.   Bigio, I.J. and Slatkine, M., "Transform-Limited-Bandwidth Injection-
       Locking of an XeF Laser with an Ar-Ion Laser at 3511 A," submitted to
       Optics Letters, (LANL preprint LA-UR 81-2631).

with $\Delta\lambda < 1$ Å requires accessing effectively the populations of both $v' = 1$ and $v' = 0$ levels. The feasibility of achieving this simultaneous $v' = 0$ and 1 access efficiently is a critical open issue both theoretically and experimentally and is fundamentally tied to the B-state pump-detail and V-T rate issues.

The practical issues of injection power and pulse duration requirements for linewidth and polarization control have been experimentally investigated in Refs. 2-3 to a very limited extent and only under kinetics conditions where the free running efficiency is low. These issues are discussed later in more detail.

In summary, from an experimental viewpoint, the important practical issues of Table 7 are currently unresolved. However, the DARPA sponsored program at Northrop is presently addressing this issue. Critically required results are expected during the upcoming PDR phase of the XeF integrator program.

2.2.5 Selection of Optimum Output Coupling

For the cavity length and pumping rates discussed earlier in this section the gain length $g_0 L = 3.3$ and $\alpha L \sim 0.165$. Allowing for a loss of 4 percent for one uncoated window and a 0.5 percent loss per mirror the equivalent $\alpha L \sim 0.02$. From Figure 12, which is a plot of the optimum output coupling as a function of g_0 for various αL, we see that the optimum output coupling is about 70 percent. This corresponds to a magnification of 1.8. If we use internal windows there could be an additional loss of 8 percent and the optimum output coupling would then be about 75 percent and the corresponding magnification 2. To obtain a 1.3 x DL we prefer a magnification of 2.5 on an output coupling of 84 percent. The loss in efficiency in increasing the output coupling is 10 percent as can be seen from Figure 13. Hence, we have designed the system with a magnification of 2.5.

Figure 14 shows the predicted efficiency as a function of time for three cases:

- No internal windows
- One internal window corresponding to an 4 percent loss plus 0.5 percent per mirror
- Two internal windows corresponding to an 8 percent loss plus 0.5 percent per mirror

Figure 13. Output Coupling

Figure 12. Optimum Output Coupling as a Function of g_0L and αL

51
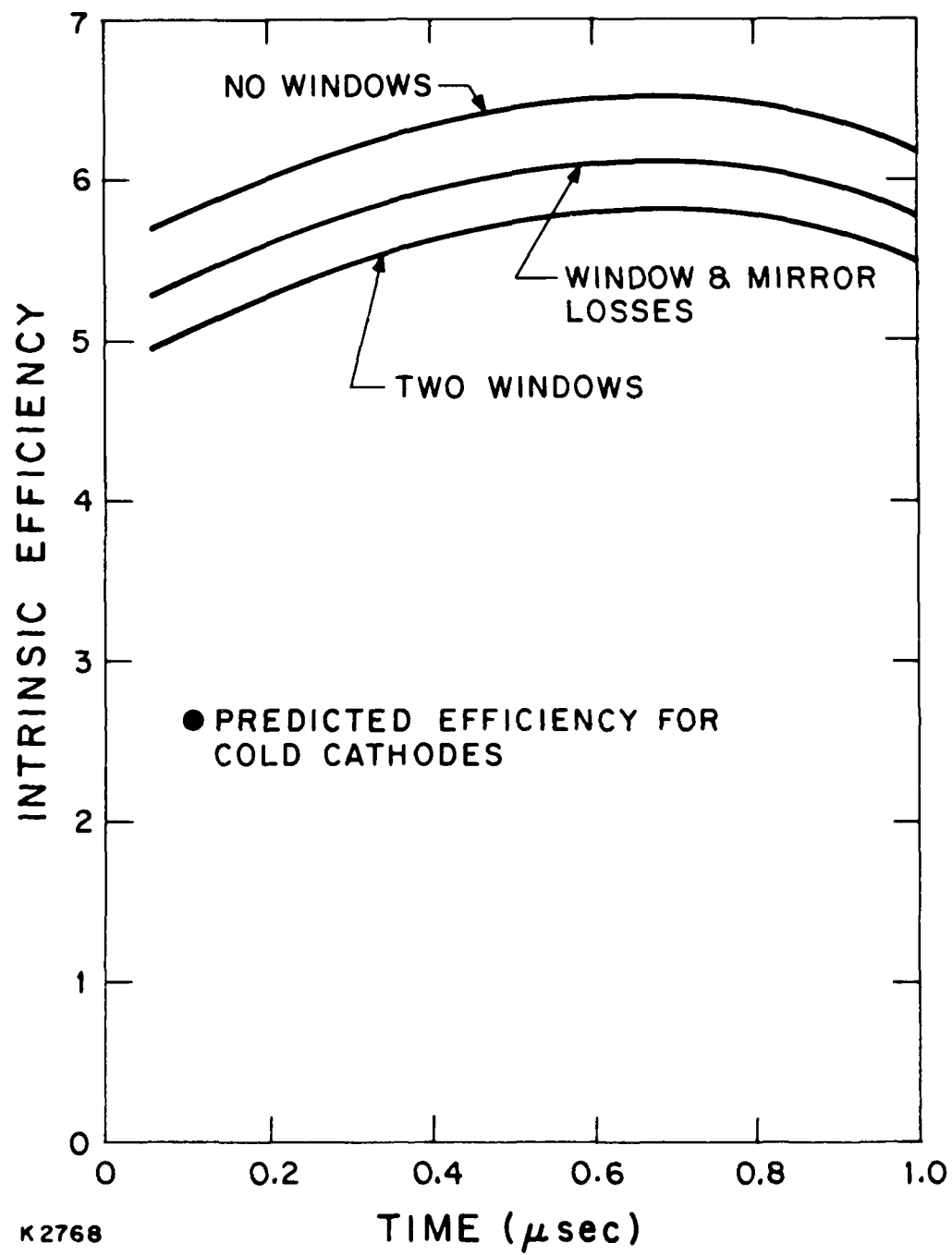
Figure 14.   Intrinsic Efficiency vs. Time

K2768

From Figure 14 it is apparent that we can easily meet the requirement of a 4.5 percent intrinsic efficiency even if we have internal windows. For narrow line extraction we presently predict a drop of efficiency of 15 percent. Allowing for such decrease in efficiency it is still possible to obtain the requirement of 4.5 percent intrinsic efficiency. In the above discussion we have assumed that one surface of a window can be AR-coated. These details will be discussed later in this chapter. It is interesting to note that the intrinsic efficiency peaks at 700 ns. This is because we have allowed the pump power to vary by a factor of two and the optimum conditions are reached when the current is somewhat larger than the mean value.

53

2.3 FOIL SUPPORT AND FOIL COOLING

For the design concept of the integrator, an e-beam is to be used to excite the gas in pulses. The e-beam generator will be at essentially vacuum conditions, but the cavity laser gas will be at 5 or 6 atm pressure. To prevent the laser gas from entering the e-beam, a solid barrier is to be used which is partially transparent to the e-beam. Electrons which are deposited in the foil cause a thermal load on the foil while the cavity pressure and overpressure due to pulse heating of the gas, cause a static and dynamic load on the barrier, respectively. To minimize the e-beam loss through the barrier, it must be a thin foil, and means must be supplied to conduct the e-beam heating in the foil away from it. Being thin, the foil must also have special considerations to retain its mechanical integrity against the pressure differences between the cavity and the e-beam vacuum. The parameters of interest are shown in Table 8.

As part of an Avco IRAD program, the feasibility of various foil cooling techniques were investigated. The results are listed below.

2.3.1. Conduction Cooled Foil Temperature Distribution

We first calculate the foil temperature distribution relative to its ends at foil support bars, considered fixed. The foil heating rate during a pulse is $Q(t)$. The temperature rise history is then

$$T(x,t) = \frac{4}{\pi \rho c_p b} \sum_{n=0}^{\infty} \frac{(-1)^n}{(2n+1)} \cos\left[\frac{(2n+1)\pi x}{\ell}\right] \int_0^t Q(t)e^{-\kappa(2n+1)^2 \pi^2 (t-t)/\ell^2} dt \tag{1}$$

where
$$\kappa = k/\rho c_p \tag{2}$$

k = thermal conductivity

b = foil thickness

t = time

ρ = density

c_p = specific heat

ℓ = foil free span

for a foil between parallel support bars where x is measured from the span center. If the pulse time is small compared to the diffusion time t_d, given by

$$t_d = \frac{\ell^2}{4\pi^2 \kappa} ,$$ (3)

then $Q(t)$ can be considered a δ function. For a high conductivity foil, aluminum, $k = 2.2$ W/cm$^\circ$C, $\rho = 2.7$ g/cm^3, and $c_p = 0.96$ J/gm$^\circ$K, then $\kappa = 0.85$. For a foil span of 0.3 cm, the diffusion time is 2.7 ms. Even a 4 μs pulse is much smaller by three orders of magnitude, hence the response is (Ref. 5).

$$T(x,k) = \frac{4E}{\pi \rho c_p b} \sum_{n=0}^{\infty} \frac{(-1)^n}{(2n+1)} \cos\left[\frac{(2n+1)\pi x}{\ell}\right] e^{-\kappa (2n+1)^2 \pi^2 t/\ell^2}$$ (4)

where E is the area energy density per pulse due to the e-beam deposition in the foil, $Q(t)dt$. The peak temperature rise occurs at the foil center, $x = 0$, hence

$$T(0,t) = \frac{4E}{\pi \rho c_p b} \sum_{n=0}^{\infty} \frac{(-1)n}{(2n+1)} e^{-\kappa (2n+1)^2 \pi^2 t/\ell^2}$$ (5)

We next consider an evenly-spaced train of pulses separated by time τ. The case of random spacing of the pulses has been calculated by a computer model which used a random-number generator algorithm, which gives an equivalent $E^* > E$, hence the evenly spaced model can still be used. Then,

$$T(0,t) = \frac{EH(t-\tau)}{\rho c_p b} + \frac{4E}{\pi \rho c_p b} \sum_{n=0}^{\infty} \sum_{m=0}^{\infty} \frac{(-1)^n}{(2n+1)} e^{-\kappa (2n+1)^2 \pi^2 (t+m\tau)/\ell^2}$$

5. Carslaw, H.S., and Joeger J.C., Conduction of Heat in Solids, Oxford, 1959, p. 130.

$$= \frac{E}{\rho c_p b} \left\{ H(t-\tau) + \frac{4}{\pi} \sum_{n=0}^{\omega} \sum_{n=0}^{\omega} \frac{(-1)^n}{(2n+1)} e^{-\beta t} e^{-\beta m \tau} \right\}$$

$$= \frac{E}{\rho c_p b} \left\{ H(t-\tau) + \frac{4}{\pi} \sum_{n=0}^{\infty} \sum_{n=0}^{\infty} \frac{(-1)^n}{(2n+1)} e^{-\beta t} \left[1 + e^{-\beta \tau} + (e^{-\beta \tau})^2 + \dots \right] \right\}$$

$$= \frac{E}{\rho c_p b} \left\{ H(t-\tau) + \frac{4}{\pi} \sum_{n=0} \frac{(-1)^n}{(2n+1)} e^{-\beta t} \left[1 - e^{-\beta} \right]^{-1} \right\} \qquad (6)$$

where $\beta = (2n+1)^2 \pi^2 / \ell^2$ and H is the Heaviside function defined as

$$\begin{aligned} H(x) &= 0 & x < 0 \qquad (7) \\ H(x) &= 1 & x \geq 0 \end{aligned}$$

The peak temporal temperature occurs at $t = \tau$, just after the next pulse in which the first term of Eq. (8) represents the pulse. Then Eq. (6) becomes,

$$T(o,t) = \frac{E}{\rho c_p b} \left[1 + \frac{4}{\pi} \sum_{n=0}^{\infty} \frac{(-1)^n}{(2n+1)} \frac{1}{e^{\beta \tau} - 1} \right] \qquad (8)$$

For a very high repetition rate, $\beta \tau > 0$ while the time-average (over the pulses) heating per unit area is $q = \lim (E/T)$. Then Eq. (8) becomes

$$T(0) = \frac{q \ell^2}{8 \rho c_p b} \qquad (9)$$

which is the same as for cw foil heating with an average heating of q.

For a typical case, $\beta(n=1) = 0.3$ and $\beta(n=2) = 3$, hence only the first term of the series in Eq. (9) need be considered, which leads to:

$$T(0,t) = \frac{E}{\rho c_p b} \left[1 + \frac{4}{\pi} \frac{1}{e^{\beta t} - 1} \right] \qquad (10)$$

For consistency, it is useful to change the coefficient of the second term from $4/\pi$ to $\pi^2/8$; hence the final scaling result is:

$$T(0,t) = \frac{E}{\rho c_p b} \left[1 + \frac{\pi^2}{8} \frac{1}{e^{\beta t} - 1} \right] \qquad (11)$$

Equation (11) gives the peak temperature difference in the foil from the center of the foil to that in contact with the foil support bar. In addition, the following thermal resistances have been considered:

- Contact resistance from the foil to the support bar. This is minimized by the high cavity pressure and the choice of soft contact material.
- The thermal resistance of the foil support bar.
- The film cooling temperature potential of the liquid coolout, for forced convection.
- The temperature rise of the coolout as it flows through the foil support bar, due to heat absorbed from the foil. A separate cooling tube is used to absorb the energy of any e-beam impingement on the vacuum side of the e-beam support.

The results are shown in Figure 15, for two different conceptual foils:

Foil	Avg Heating Rate	Tmax
1/2 mil Ti/1/2 mil Al	140 W/cm^2	550°C
1 mil Al	60 W/cm^2	200°C

and for two coolants, liquid nitrogen and ambient water.

As can be seen, for water-cooling, a foil free span of about 3.5 mm is possible for aluminum and 2.5 mm is needed for the Ti-Al composite foil. It is shown later that the static stresses are excessive for the aluminum foil.
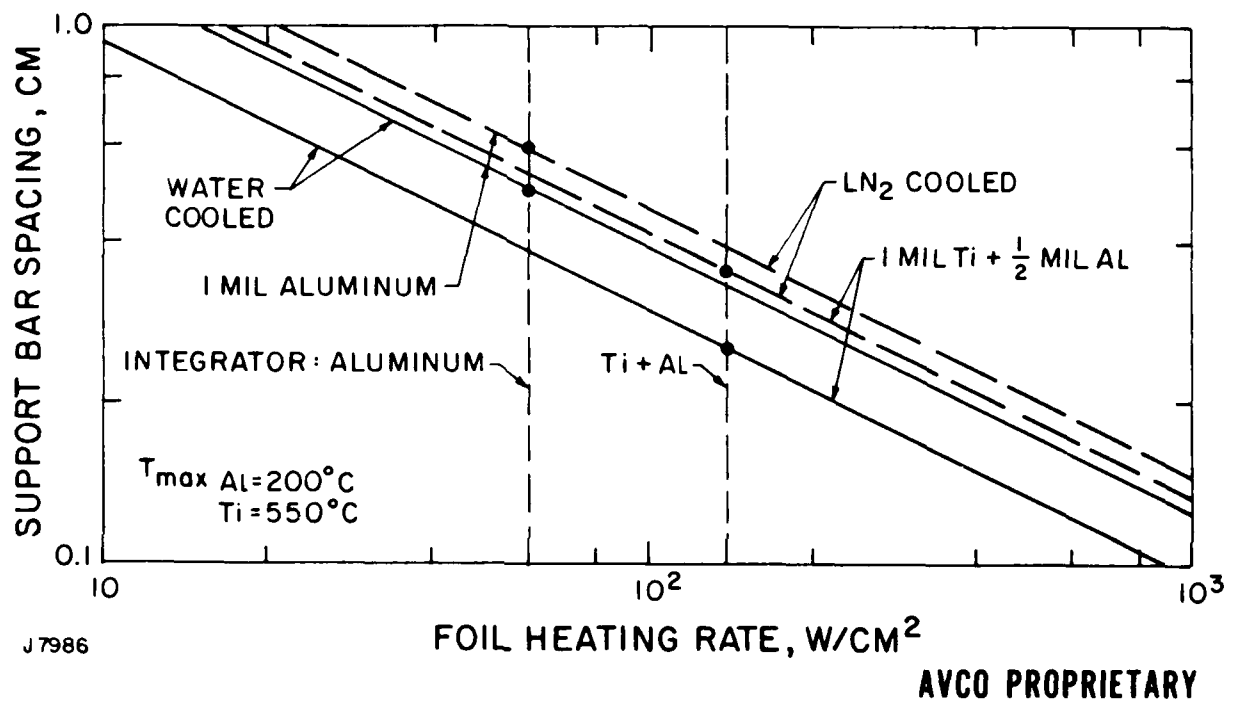
Figure 15.   Required Foil Free Span as a Function of Foil Material and
             Coolant in Foil Support Bar

58

2.3.2. Convection Cooled Double Foil

We next examine the feasibility of using convection cooling in a channel formed by a double-foil as shown in Figure 16. The film heat transfer coefficient h can be obtained from Reynold's analogy with the friction coefficient c_f:

$$h = \rho u c_p (c_f/2) \qquad (12)$$

where u is the interchannel gas speed, and ρ is the gas density Nm where N is the coolant gas number density and m is the gas particle mass. The former is given by

$$N = \frac{p}{KT} \qquad (13)$$

where p is the interfoil coolant gas pressure, K in Boltzmann's constant, and T is the coolant gas absolute temperature. Also, the specific heat of the coolant gas is given by:

$$c_p = \frac{(\hbar+2)\ K}{2m} \qquad (14)$$

where $\hbar$ is the degrees of freedom of the coolant gas molecule. As an example, we consider a monatomic coolant gas, for which $\hbar = 3$. Then Eq. (12) becomes:

$$h = \frac{5pu}{2T} \ (\frac{f}{2}) \qquad (15)$$

which shows that the gas cooling heat transfer coefficient depends on the product of the gas speed and pressure, and is insensitive to the gas molecular weight. Hence, high pressures and gas speeds are desirable. The gas speed cannot be increased indefinitely due to choking effects caused by the increase in the gas temperature as it passes through the channel. This increase is given by:

59
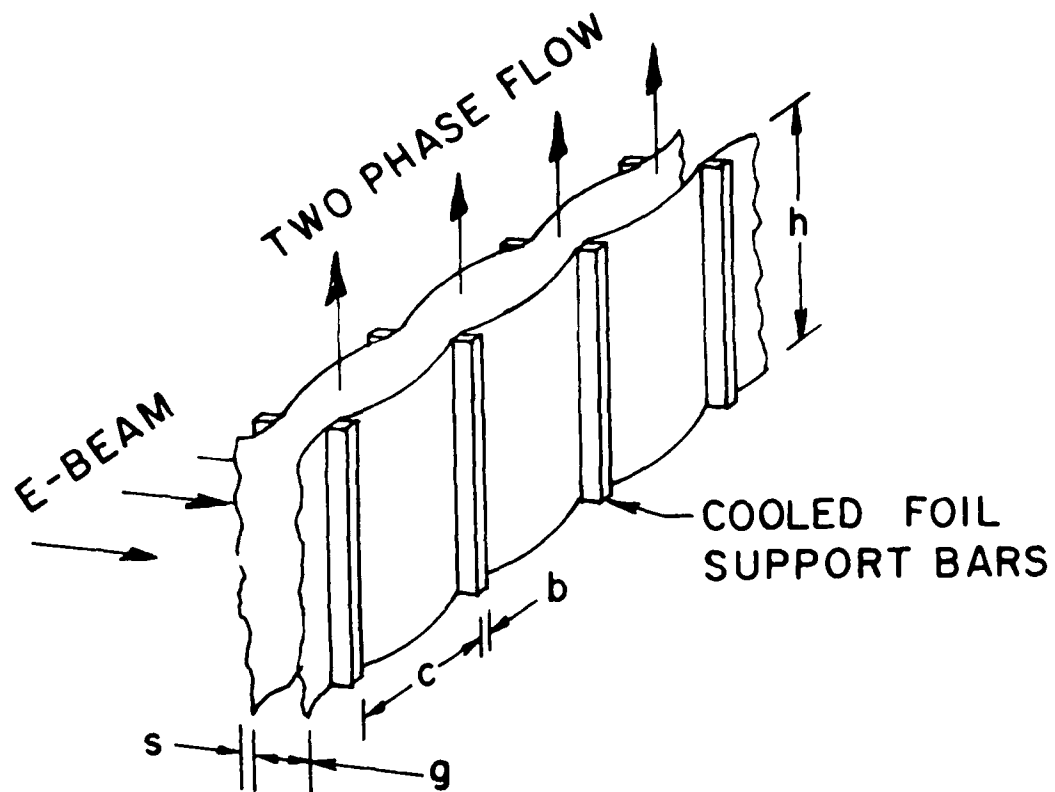
HI672

Figure 16.   Schematic Diagram of a Double Foil for Convective or
Phase-Change Cooling. The case shown is for the interfoil
pressure greater than the cavity pressure

$$T_0(x) - T_{0_1}(0) \simeq \frac{2}{5} \frac{q_t\, T_1}{p_1 u_1}\, \frac{x}{a} \qquad (16)$$

where the subscript 1 refers to the inlet, as the channel half-height, and q_t is the total heat transfer into the gas consisting of the e-beam heating of the foil and the coolant gas. The choking limit is given by: [6]

$$\frac{T_{0_2}}{T_{0_1}} = \frac{\left(1 + \gamma M_1^2\right)^2}{2(\gamma+1) M_1^2 \left(1 + \frac{\gamma-1}{2} M_1^2\right)} \qquad (17)$$

where the subscript 2 refers to the outlet where the Mach number is unity, and γ is the ratio of specific heat for the coolant gas. The highest friction co-efficient c_f possible is for very rough walls, for which $c_f = 0.015$. Using the above 3 relations, the results shown in Figure 17 were calculated for two different foils and for two different initial coolant temperatures, 100°K and 300°K. The short dashed lines suggest that one should avoid design of the exit Mach number near unity. For the latter, an initial helium speed of 10^2 M/S is needed. For smoother walls, the friction factor is lower by about a factor of 4, implying that 15 W/cm^2 and 35 W/cm^2 could be removed for an inlet speed of 10^2 M/S. To achieve the original design values, an inlet helium coolant speed of 400 M/S is needed which could entail additional risk or development; for example, the possibility of flow-induced flutter.

The effect of extension of the cavity width to 50 cm is shown in Figure 18. For the same amount of cooling, about 50 percent more gas coolant speed would be required, which, for a friction coefficient of 0.004 comes very

6. Shapiro, A.H. "Compressible Fluid Flow," Ronald, N.Y. 1953, p. 196.

AVCO EVERETT

Figure 17.   Convective Cooled Foil Performance for the Closed Cycle
              Integrator.   The maximum Stanton number possible for cooling was
              used.   Coolant pressure = 5 atm
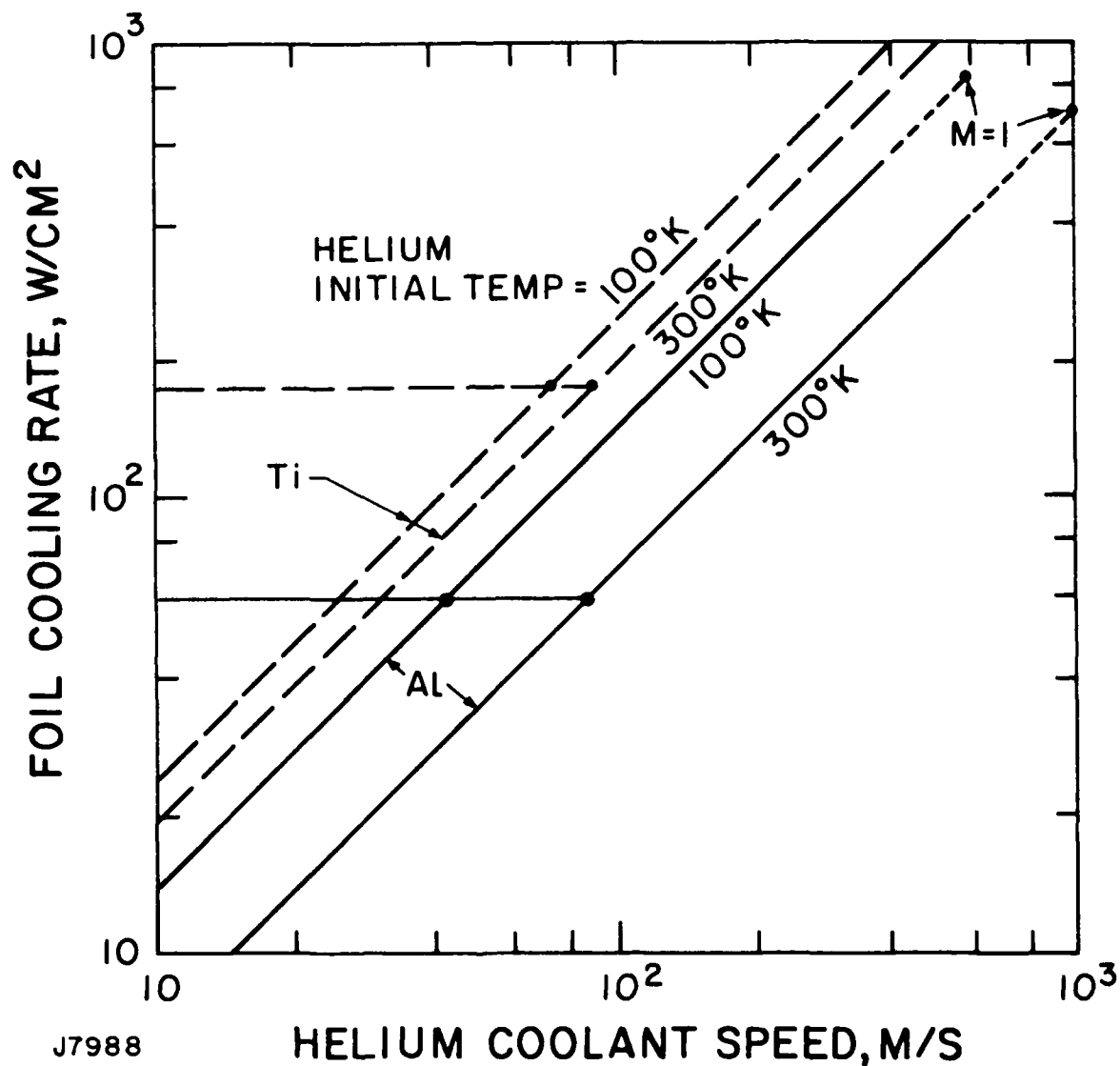
AVCO PROPRIETARY
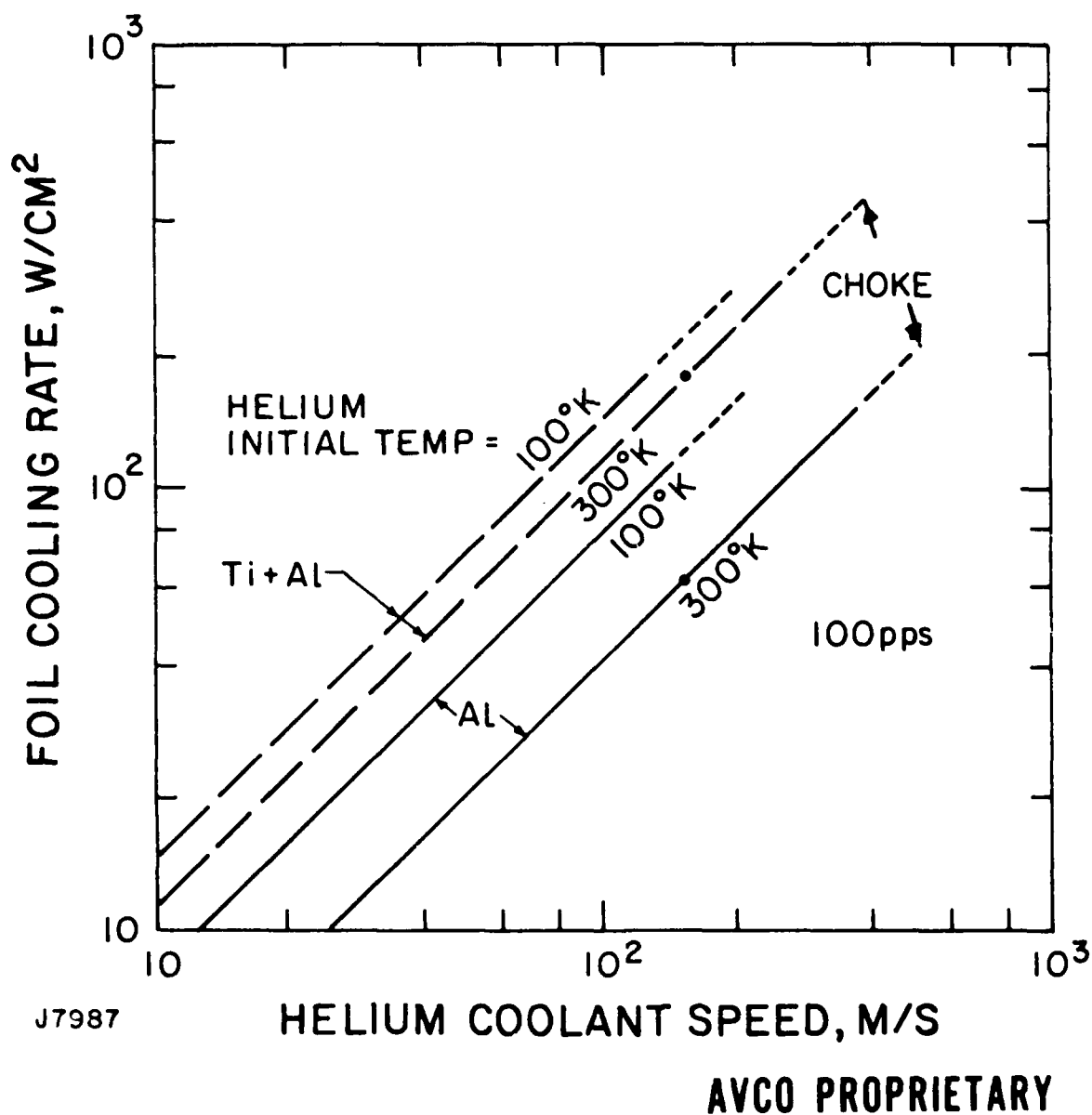
Figure 18. Convective Cooled Foil Performance for a 50 cm Wide Foil. The maximum Stanton number possible for cooling was used. Coolant pressure = 5 atm

63

close to the choke point. The lack of adequate margin makes the convective cooling less desirable than the other potential techniques.

2.3.3. Phase-Change Cooling

As a variation on the concept of convective cooling, liquid droplets can be added to gas flow previously mentioned. The droplets will diffuse to the foil as a form of spray cooling, for which some experiments have been performed.[7] An equation to predict the performance of this technique has been derived, which gives the maximum average cooling rate, as follows:

$$q_{pc} = g \, \Delta h_v \rho_d u \tag{18}$$

where g is a constant whose numerical value has been determined, Δh_v is the latent heat of evaporation of the coolant liquid, u is the carrier gas speed in the channel between the two foils, and ρ_d is coolant liquid density in the two phase flow. The cooling results predicted from Eq. (18) agree very closely with the experimental results of Ref. (7).

A safety margin, however, should be applied to Eq. (18). This causes a liquid layer to build up on the foil between pulses, because the rate at which droplets impinge on the foil is greater than the rate at which any liquid on the foil can evaporate.

A model of the history of such a liquid layer has been derived. The foil is superheated by the pulse, and initiates a vapor layer which is close to the foil temperature between the foil and the liquid layer, and therefore the vapor layer is at a very high pressure. The high-pressure vapor layer then acts on the liquid layer to drive it away from the foil. In the next step, the expansion of the vapor layer cools adiabatically, but heat conduction from the foil through the vapor layer to the liquid layer evaporates more vapor. As the liquid layer moves away from the foil, the vapor conductance decreases, while the expansion continues until the pressure of the vapor layer becomes close to the channel pressure. Surface tension of the liquid layer then breaks it into droplets which are returned to the bulk flow. This first stage takes a few microseconds. Afterward, a second stage

7. "Phase Transition Cooled Window Studies for High Average Power Electron Guns, RCC Industries Report 80-11403-80, Dec. 1980.

△ⅉAVCO EVERETT

ensues, of spray cooling in which each droplet evaporates as it impinges on the surface, thereby continuing to cool the foil. This process continues until the foil temperature decreases below the coolant saturation temperature, after which a third stage occurs in which the liquid layer builds up, and the cooling proceeds by molecular diffusive evaporation of the coolant from the surface. This process is shown schematically in Figure 19. The maximum foil temperature T_{max} just after the liquid layer is removed is given by:

$$T_{max} - T_{sat} = \Delta T_p \; \frac{\rho_{dmin}/\overline{\rho_v} - 1}{\rho_{dmin}/\overline{\rho_v} - S} - 1 \tag{19}$$

where T_{sat} is the saturation temperature of the coolant at the interchannel pressure, ΔT_p is the foil temperature increase due to a pulse, ρ_{dmin} is the minimum droplet mass density as determined from Eq. (18), S is a safety factor and ρ_v is the mean vapor pressure between the saturation temperature and $T_{max} - \Delta T_p$.

For the conceptual design, we considered a helium carrier at 5 to 20 m/sec. From Eq. (18), adequate cooling is predicted for phase change cooling, as shown in Figure 20.

2.3.4. Foil Stress Considerations

In addition to the thermal load the foil must also carry a mechanical load due to the pressure difference across it. Two cases are considered, (a) foil initially flat, and (b) foil initially preformed.

(a) Foil initially flat. For this case, the static foil stress σ is given by

$$\sigma = \frac{2}{3} E \left(\frac{3}{8} \frac{p\ell}{Eb} \right)^{2/3} \tag{20}$$

Where E is Young's modules and p is the pressure difference across the foil. Note that the stiffer the material, the higher the stress. The stresses predicted from Eq. (20) are shown as the solid lines in Figure 21. These results

65
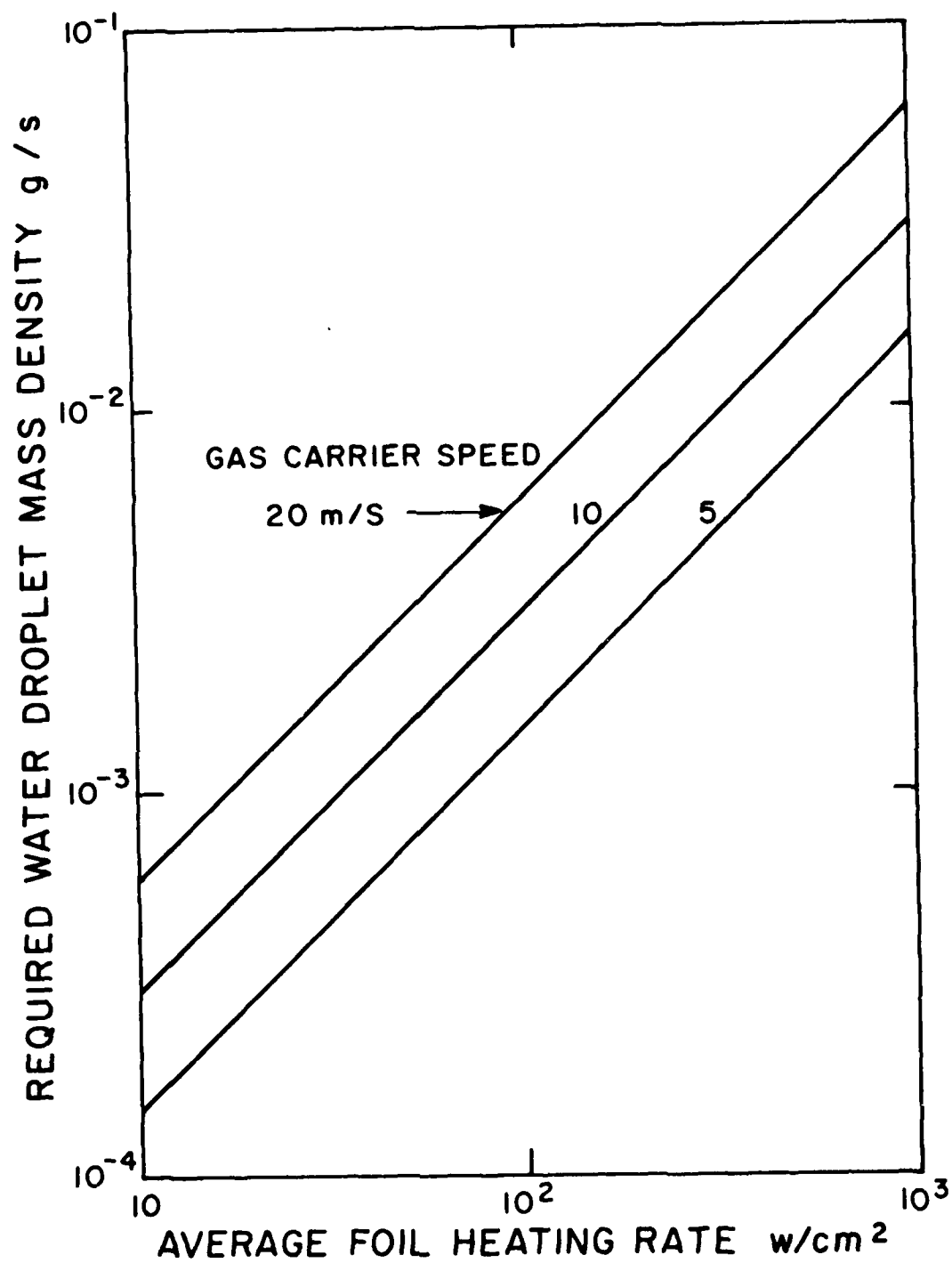
Figure 19.   (Top Only) Schematic of the Temperature History of a Foil
Subjected to Phase-Change Cooling

K5022
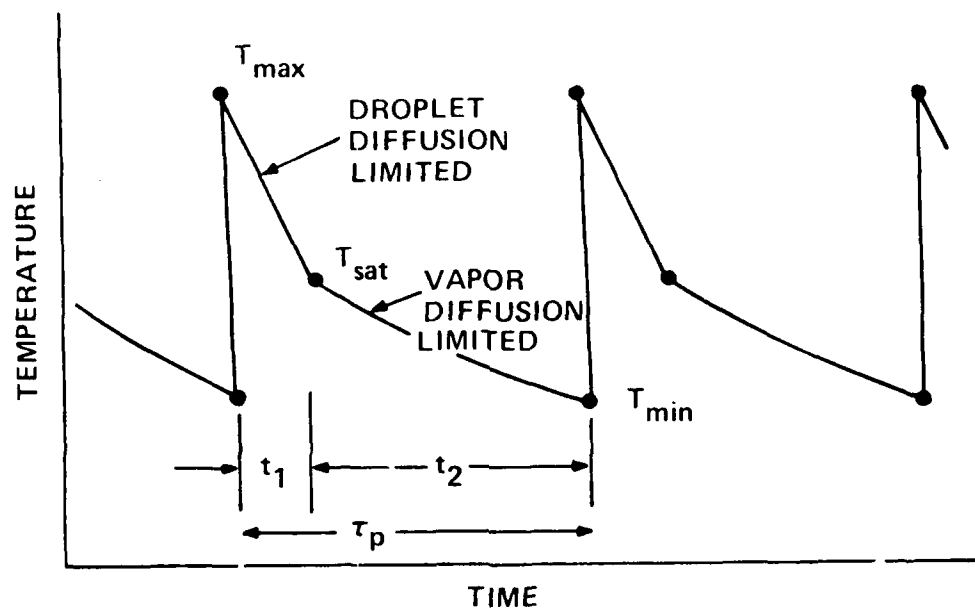
Figure 20.   Minimum Water Droplet Density needed for Phase-Change Cooling

indicate that rather small support bar spacing is needed. This can be achieved by preforming the foil to an initial elongation, considered next.

(b) Foil preformed to an initial elongation. For this case, the foil stress is given by:

$$\sigma = \frac{p \ell}{\sqrt{6\epsilon_0}}$$

(21)

Where ϵ_0 is the preform elongation. These results are also shown in Figure 21. About 2 percent is a reasonable preform elongation. For aluminum at an elevated temperature the maximum foil free span would be slightly over a millimeter, but for titanium, the foil support spacing can be > 1 cm based on the static stress. For the conduction cooled foil, cooling places the constraint on the maximum foil free span. For phase-change cooling, the initial evaporation of the liquid layer on the foil, which leads to high pressure on the liquid layer, also leads to high pressure on the foil. This can cause impulsive loading of the foil and additional stresses.

2.3.5. Summary

The results indicate that either conduction or phase change cooling can be used for the e-beam foil. Because of the stress considerations the conduction-cooled foil requires high strength as well as conductance which indicates that a laminate should be selected. For phase-change cooling, if water is used, the foil will be initially at the saturation temperature of the coolant, but then will be heated by the pulse. The resulting temperatures for aluminum make it marginal. Titanium, even though its pulse temperature increase is larger, has both a higher strength and higher service temperature. Thus, a titanium alloy is indicated for the base foil material selection. For the preliminary design, analyses are recommended for the dynamic stresses caused by the sudden pressure increase of the cavity gas at each pulse.
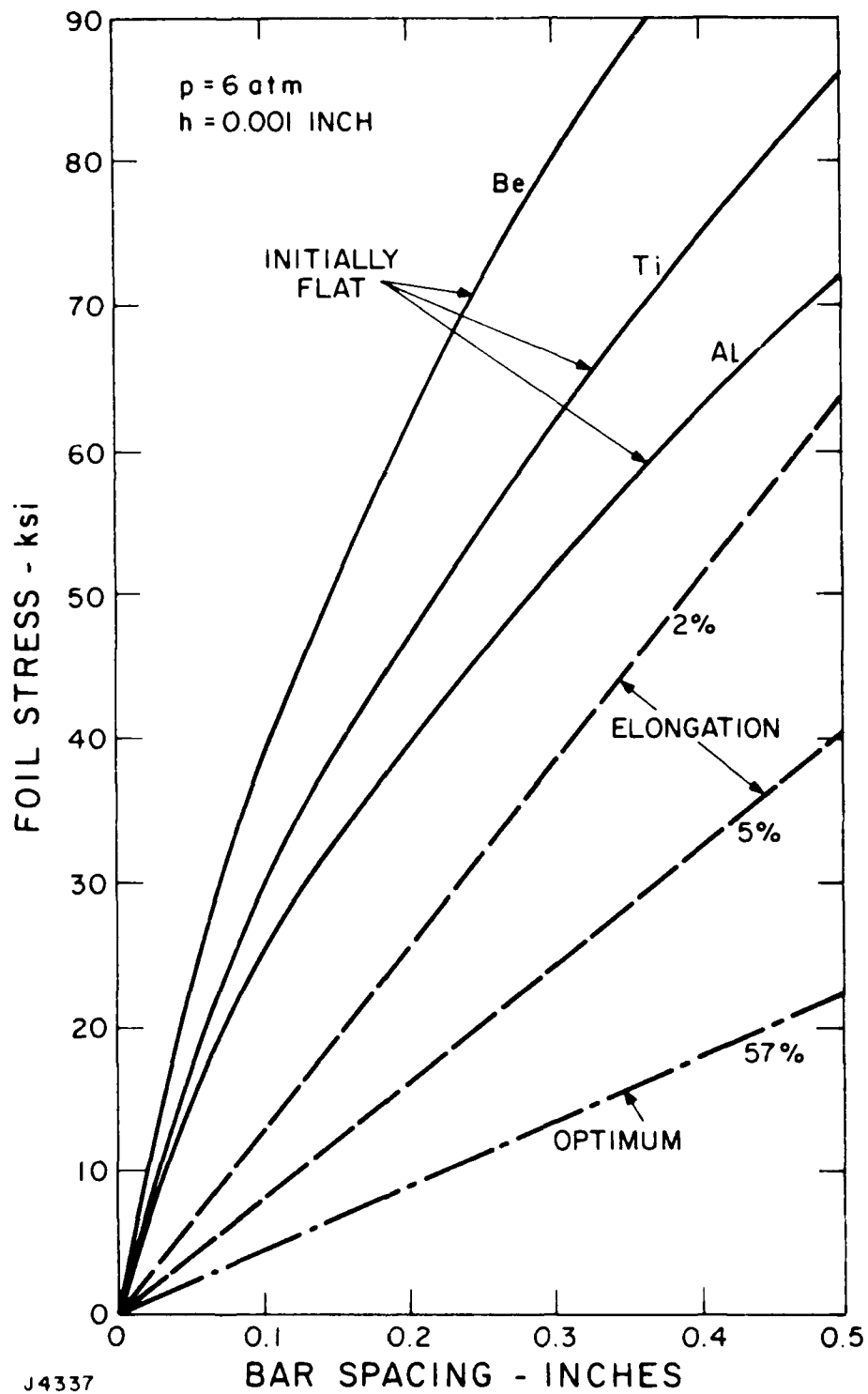
Figure 21.   Static Foil Stresses

TABLE 8.   NOMINAL FOIL HEATING PARAMETERS

Avg Heating   50-150 W/cm^2

PRF   100 S^{-1}

Pulse Time   1-4 μs

2.4 ACOUSTICS AND CAVITY HOMOGENEITY ISSUES

2.4.1 Cavity Medium Homogeneity

Cavity medium density inhomogeneity gives rise to phase aberration of the output beam in accordance with

$$\delta\phi_{rms} = \frac{2\pi L}{\lambda} \sqrt{\frac{\Omega}{L}} \, \beta \, \frac{\rho}{\rho_s} \left(\frac{\delta\rho}{\rho}\right)_{rms} \tag{21}$$

where Ω is the integral scale size for random disturbances and $\Omega = L$ for ordered disturbances. In turn, the Strehl ratio

$$I/I_0 \sim \exp\left(-\delta\phi^2_{rms}\right) \tag{22}$$

and a measure of beam quality for small $\delta\phi$ is $\sqrt{I_0/I}$. Note that L is greater than the cavity optical length because light rays typically make several passes before leaving the resonator. This, together with the fact there are other contributors to loss of beam quality, means that the medium homogeneity requirements are very stringent in order to achieve a 1.3 XDL output beam from a larger device.

The total cavity medium inhomogeneity budget adopted for the baseline design point is

$$\sqrt{\sum \frac{\Omega}{L} \left(\frac{\delta\rho}{\rho}\right)^2_{rms}} \lesssim 3 \times 10^{-5} \tag{23}$$

where the summation includes all sources related to the XeF laser gas. This level of density uniformity has been demonstrated experimentally in blowdown, room temperature systems under flow/acoustics technology efforts sponsored by DARPA. It is possible that we can do even better if necessary, but the bound given in Eq. (23) is reasonable for the integrator conceptual design. The Phase I-A device involves a closed-cycle system operating at elevated temperature.

71

There are a number of sources contributing to the summation in Eq. (23); e.g., ordered velocity nonuniformity, turbulence, thermal effects, flow noise, boundary layers on optics, residual acoustics from previous pulses, and entropy waves. Those that are related to compressibility effects scale as cavity Mach number squared. To illustrate, ordered velocity nonuniformity gives rise to density nonuniformity in accordance with

$$\frac{\delta\rho}{\rho} \sim KM^2 \frac{\delta u}{u} \tag{24}$$

where K is a constant of order one which depends on the particular thermodynamic process assumed. An upper bound for the constraint on turbulence intensity, $(u'/u)_{rms}$, can also be inferred from Eq. (24) provided the $\delta\rho/\rho$ requirement is relaxed by the factor $\sqrt{L/\Omega}$ since the disturbance is random. Standard low speed wind tunnel design techniques can be used to suppress these. Flow noise can arise, for example, from fan blades and repetitive interaction of hot gas slugs with the heat exchanger. These again scale as M^2 and should be easily manageable in the Phase II system with proper design.

The primary thermal effects are going to be relatively insensitive to Mach number for the recommended Phase I-A operating regime. For example, in a thermal wake

$$\frac{\delta\rho}{\rho} \sim \frac{\delta T}{T} \tag{25}$$

Care will be required to avoid ordered thermal disturbances entering the cavity. Random thermal disturbances are more easily tolerated provided they have sufficiently small-scale size Ω. Discussion of how adequate temperature uniformity is to be achieved requires consideration of the entire flow loop and thermal conditioning systems. This will be deferred to the following section. A plausible goal for the baseline design point is to achieve an effective ordered $(\delta\rho/\rho)_{rms} \leq 2 \times 10^{-5}$ for a root-square-sum of all flow and thermal sources, including entropy waves from the flow conditioning elements. That is a demanding goal, but then so is the DARPA specification of a 1.3 XDL output beam for a full scale device.

The medium homogeneity budget for residual acoustic waves and entropy waves from the primary attenuators is an effective ordered $(\delta\rho/\rho)_{rms} \leq 2 \times 10^{-5}$, so that the total budget in Eq. (23) is not exceeded. It is quite conceivable in a fixed rep-rate machine that rms tilt removal is possible with preset optical correction, at least within 10 percent pulse to pulse. In that case stronger residual acoustic waves are acceptable if they are of sufficiently long wavelength, and the attenuator system can be smaller. This applies to the Phase I system, on the other hand, tilt removal in a variable rep-rate of the sort envisaged in the Phase I-A study, machine will require dynamic correction and appears less straightforward. We have adopted the position that only static or slowly varying tilt will be removed. The $\delta\rho/\rho$ requirement above is to be understood accordingly.

2.4.2 Acoustics Design Concept

Acoustic attenuators can be divided into two broad categories: flow-through arrangements and absorbers mounted outside the flow channel (e.g., in the sidewalls). When applied upstream of the laser cavity, a flow-through absorber will cause a velocity wake and can also generate thermal inhomogeneity. This is inconsistent with the high medium homogeneity required for the Phase I-A system. Sidewall mufflers can be designed to avoid such deleterious effects, as established in the flow technology programs sponsored by DARPA. A similar attenuation system downstream of the cavity makes sense because a flow-through absorber will generally involve greater pressure drop due to its larger wetter area. That in turn impacts system efficiency.

Sidewall muffler systems of the sort outlined above have been implemented in two distinct ways in DARPA sponsored flow technology programs. These are shown schematically in Figure 22. The approach taken at AERL involves mufflers immediately upstream and downstream of the laser cavity where the flow channel hydraulic diameter is small. This allows the use of smaller muffler volume, as discussed in the following subsection. The approach taken by Poseidon Research, Inc. involves a close-in muffler downstream of the cavity and a very disperse attenuation system upstream. The main driver in this case is to avoid defining a strong acoustic resonator which "traps" waves in the laser cavity.

The choice between these two configurations involves judgment at this stage because the final results of the flow technology programs are not yet available. Based on the experimental results that are available at AERL as well as theoretical projections, we feel that wave trapping is not a serious concern in a well designed close-in dual muffler arrangement. Moreover, nominal amounts of suction have been demonstrated to control the impact of boundary layer growth in the upstream muffler section on usable cavity volume. Therefore, since minimizing the ratio of loop volume to cavity volume is a prime concern for a large XeF laser system, the acoustics system for our design concept is based on the AERL arrangement depicted in Figure 22. These points are expanded in what follows.

2.4.3 Longitudinal Wave Clearing

A key point concerning sidewall mufflers is that their size scales with the local hydraulic diameter of the flow channel. This was first evident in the correlation of experimental data[8] for an infinite capacity muffler shown in Figure 23. In this case the shock attenuation distance, and hence the muffler length, increases linearly with D. Similar results hold more generally. Another thing evident in Figure 23 is that the shock attenuation distance decreases as α increases. There is a counterbalancing consideration in the case of finite capacity mufflers as will be seen below.

Several stages are involved in displaying the effects that must be considered for a good close-in muffler design. A good starting point is quasi-1D weak wave theory for an isolated finite capacity muffler, which has been shown to be in reasonable agreement with experiments[9] for the regime of interest in excimers. The main advantage of weak wave theory is that it involves fewer parameters and so an overview of the design strategy is more easily displayed.

8.   Szumowski, A.P., "Attenuation of a Shock Wave Along a Perforated Tube," Proc. 8th Intl. Shock Tube Symp., Chapman and Hall, 1971, Paper No. 15.

9.   Tong, K., Knight , C. and Srivastava, B., "Pressure Wave Attenuation in Mufflers with Finite Backing Volume," AIAA Paper No. 79-0602, March 1979.

MUFFLERS

FLOW →

CAVITY

AERL CONCEPT

MUFFLERS

CAVITY

FLOW →
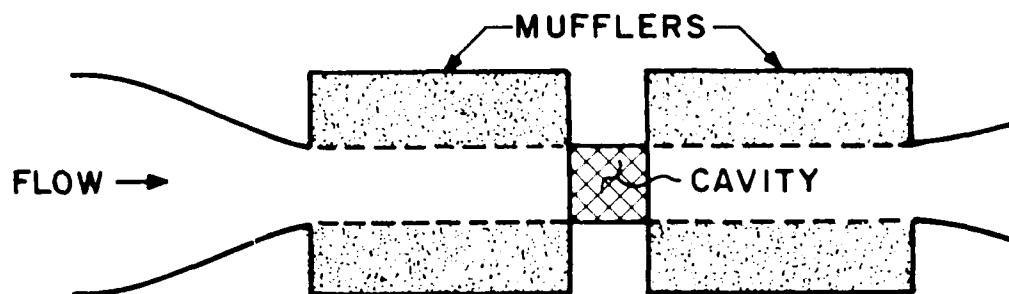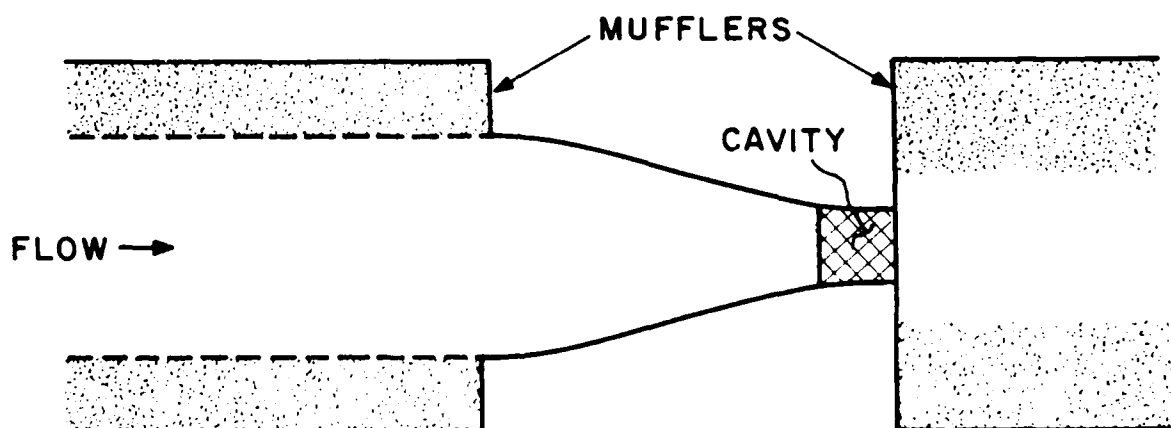
POSEIDON CONCEPT

K2828

Figure 22.   Two Acoustics Design Approaches
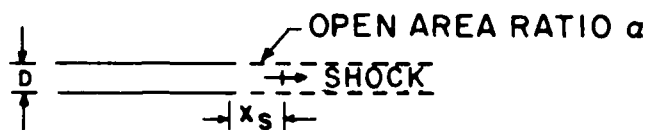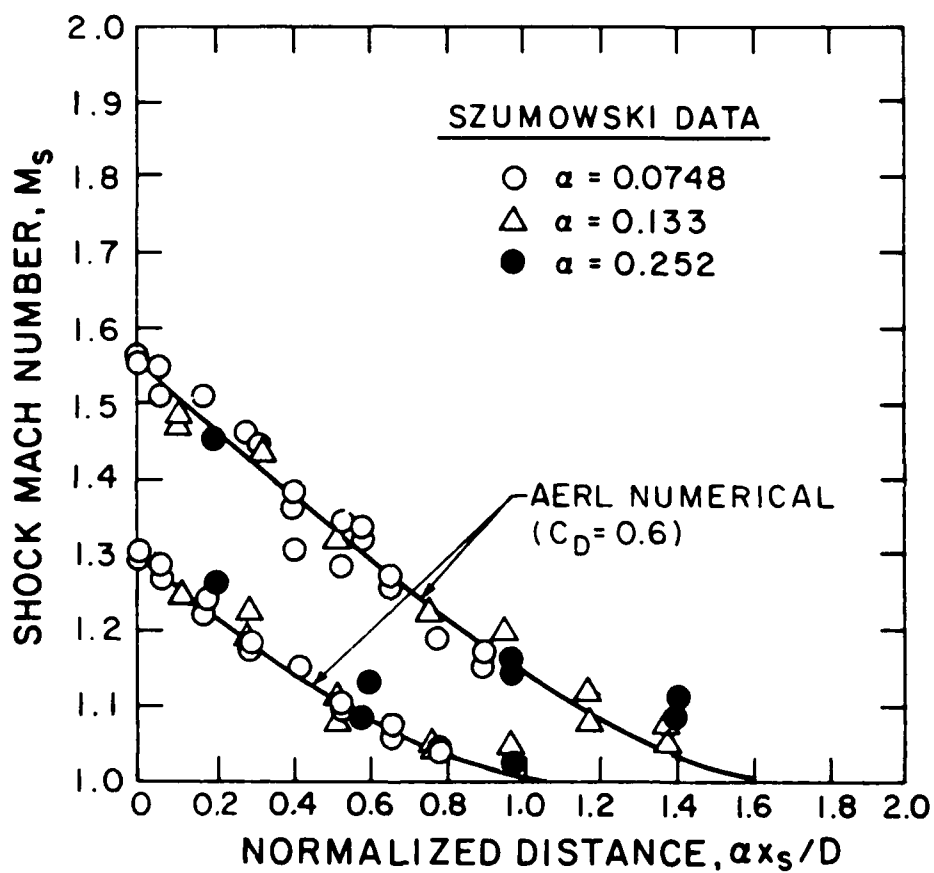
Figure 23. Shock Attenuation in an Infinite Capacity Muffler Based on AERL Correlation of Szumowski Data

Note that $H\lambda/2h^y{}_M$ can be interpreted as the ratio of the cavity volume to the backing volume of the muffler. The configurations considered for Figure 24 involve constant α and h throughout the muffler section. Other studies have been done with variable α and h to find that Eq. (27) gives a good representation more generally. The optimal configurations are not strongly affected if the goal is maximizing acoustic energy dissipation within the muffler rather than minimizing transmitted wave strength.

The attenuation process is altered by several effects in a real system. A linear component of sidewall resistance can arise from an acoustic liner over the perforated plate (for efficient suction) and from grazing flow effects. This leads to exponential shock decay at later times which is characterized by the parameter $\beta = \alpha C_D \zeta_w \sqrt{\gamma p / 2\Delta p_i}$ where ζ_w is a normalized (linear) sidewall impedance. Fluid inertia within the perforations causes a delay in achieving the steady-state mass exchange process assumed in weak wave theory. In consequence, rarefaction waves produced by that process start behind the shock and must catch up by nonlinear wave overtaking. That is characterized by the parameter $K = (\gamma + 1)L\Delta p_i / 8\gamma p d$, where d is the hole diameter and L is the attenuation distance defined in Figure 24. So long as the system is designed with $\beta < 0.2$ and $K > 2$, these effects are not of great importance. Compressibility effects can generally be overlooked to first order for excimer lasers.

Mufflers immediately upstream and downstream of the cavity have been implemented on the Humdinger, Jr system shown schematically in Figure 25. The following relationships for this sort of arrangement can be derived for zero baseline flow, and are approximately true more generally,

$$L_c \Delta p_c / \bar{a} = \int_0^\infty P_t dt = \int_0^\infty Q_t dt$$

$$(28)$$

$$L_c (\Delta p_c)^2 / \bar{a} = \int_0^\infty P_t{}^2 dt + \int_0^\infty Q_t{}^2 dt + D_M$$

77

PARAMETERS ENTERING STUDY
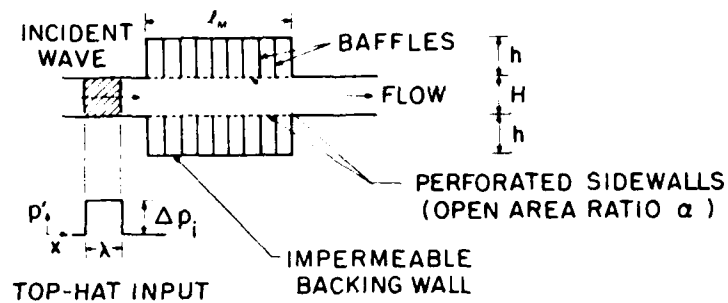
PEAK PRESSURE TRANSMISSION
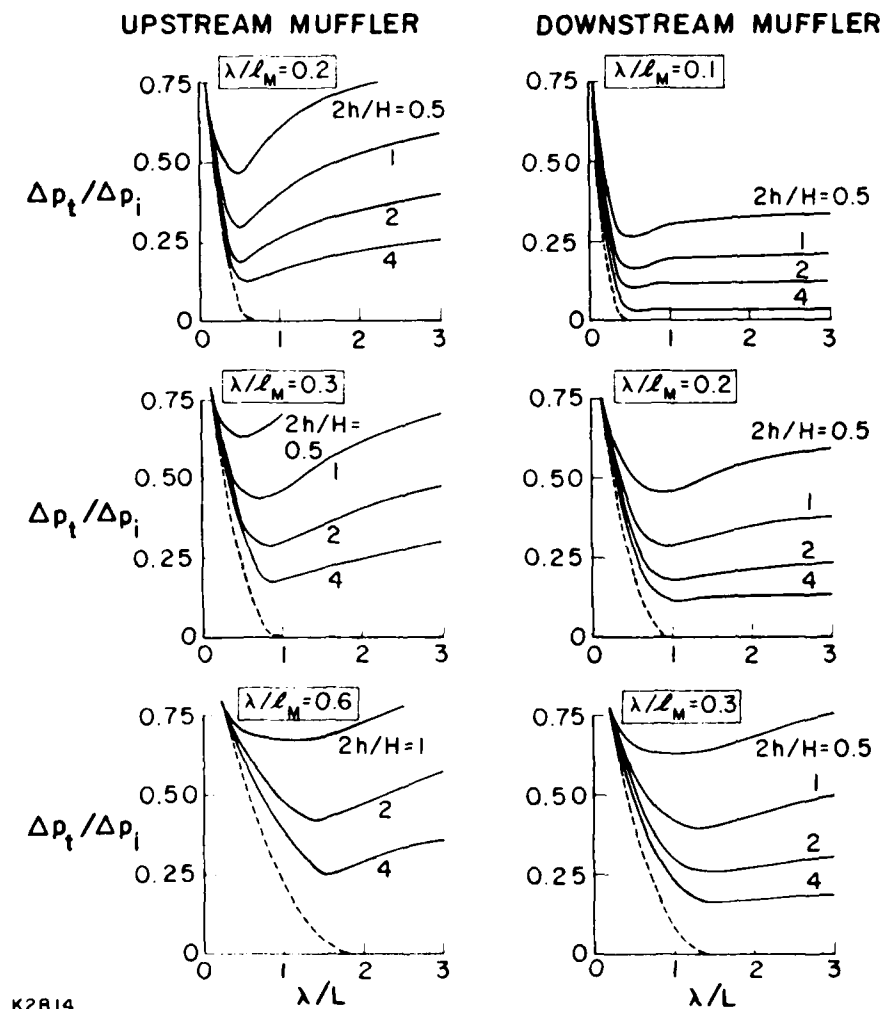
Figure 24.   Muffler Theoretical Trade-Off Study for M = 0.2
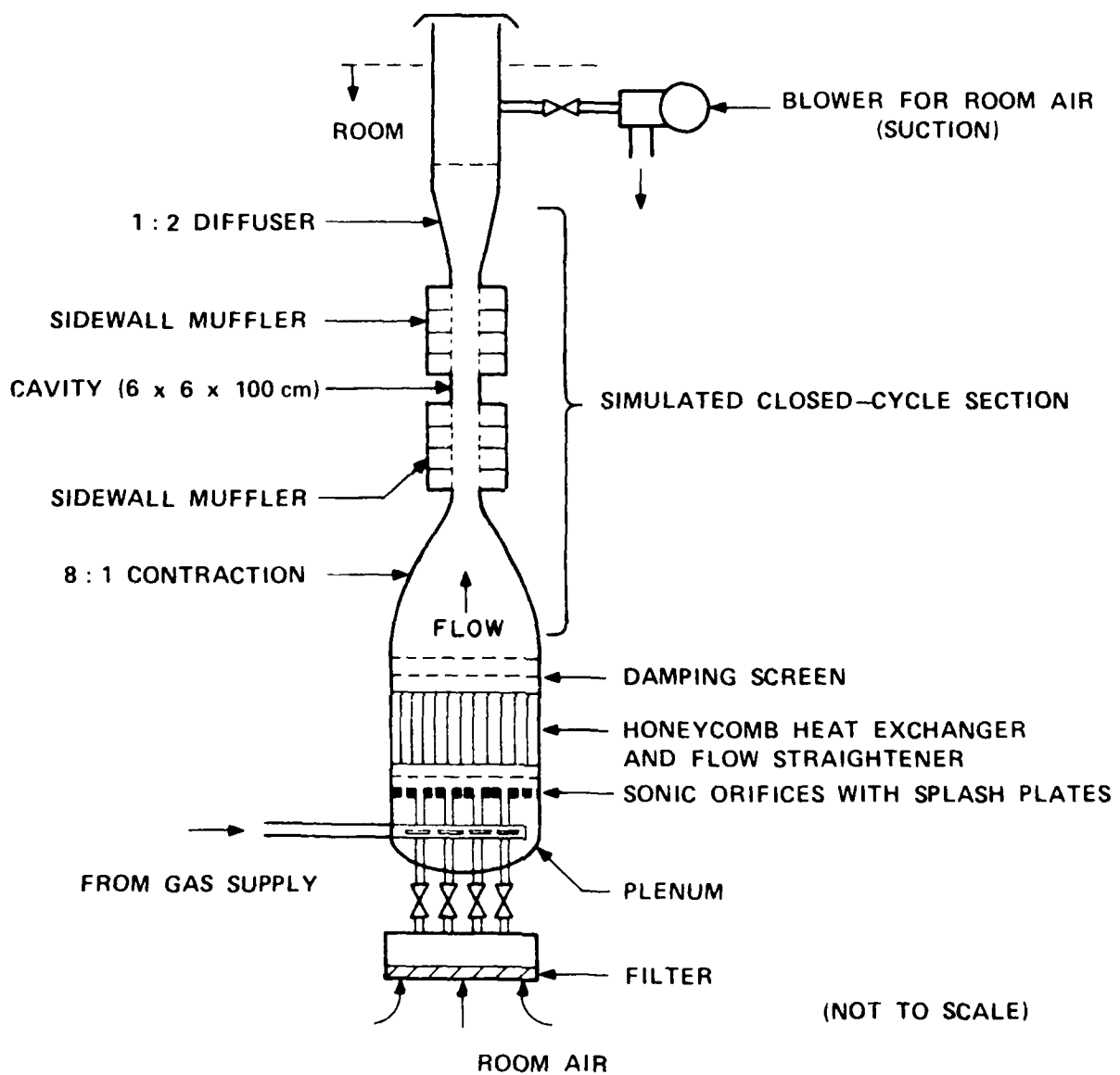
Figure 25.   AERL Flow/Acoustics Facility

H6675

where Δp_c is the initial cavity overpressure, L_c is the cavity length, P_t and Q_t are the linearized Riemann invariants for waves transmitted outside the muffler system, and D_M is the acoustic energy dissipated within the mufflers. It is never possible to prevent waves from getting into the rest of the closed loop system. It is possible with proper design to assure that 5 percent or less energy transmission occurs and that the transmitted waves have long wavelength compared to L_c. The first is achieved by suitable choice of the average open area ratio and the total volume of the mufflers; the second by careful impedance matching. Impedance matching in Humdinger, Jr involved tailoring the open area ratio as shown in Figure 26. That together with variable flow channel area and backing depth was considered for the conceptual design.

The predicted performance for the Humdinger, Jr flow/acoustics system is shown in Figure 27 for a top hat energy loading over the 6 x 6 x 100 cm cavity. This is a fully nonlinear calculation including all elements shown in Figure 25 from the sonic orifice plate through the diffuser. Entropy wave production within the upstream muffler, arising from pressure wave interaction with it, is included in the $\delta\rho/\rho$ estimate and that has substantial impact on flow clearing time. More about that later. The best instantaneous rms tilt correction has been removed for Figure 27. This appears feasible for the Phase I conceptual design, which involves operation at fixed rep-rate. In the case of the Phase IA conceptual design, which involves variable rep-rate within a run, feasibility is less likely, and the muffler size would have to be increased to assure acceptable tilt error for the range of possible inter-pulse times.

Thus far Humdinger, Jr has not operated with a confined discharge. The modifications to implement a magnetically guided e-beam, and hence a confined discharge, are now near completion. With an unconfined discharge, the energy spreads over a region 2-3 times larger than the 6 cm e-beam aperture. For $L_c \sim 15$ cm in Figure 27, the experimental results that have been obtained with an unconfined discharge are in reasonable agreement with Figure 27. Experimental results with a confined discharge are expected during the summer of 1982.

ANODE SIDE

OPTICAL FLOW
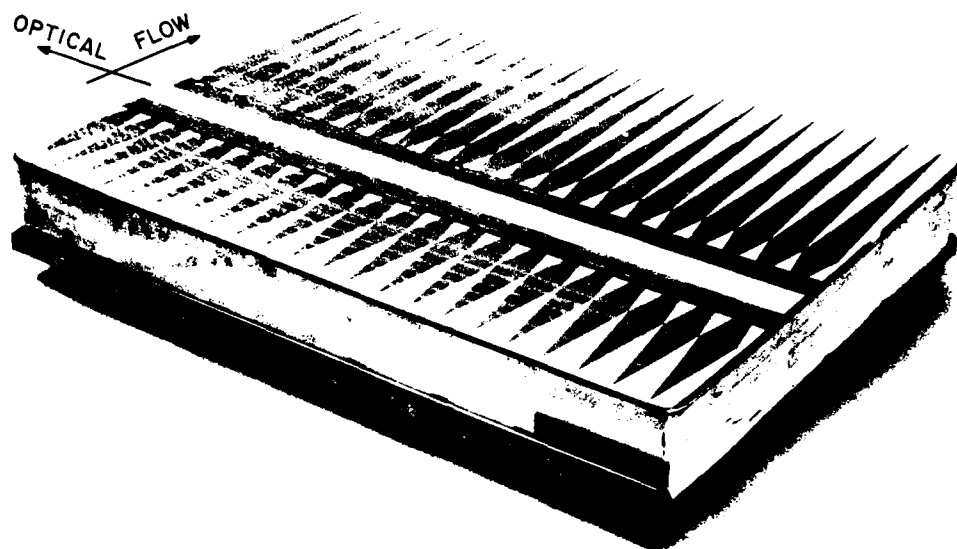
CATHODE SIDE
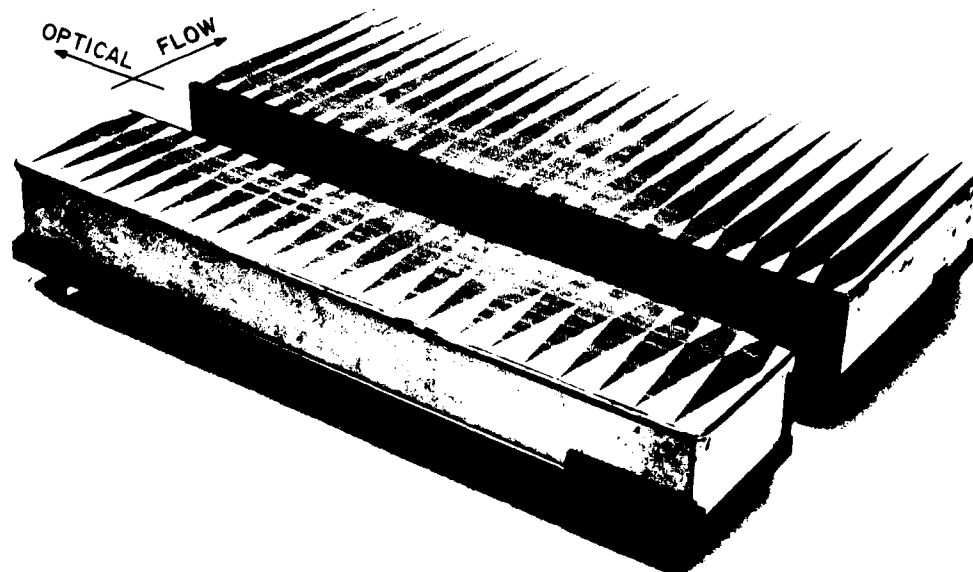
OPTICAL FLOW

J2901

Figure 26.   Variable Open Area Ratio for Impedance Matching

AVCO EVERETT
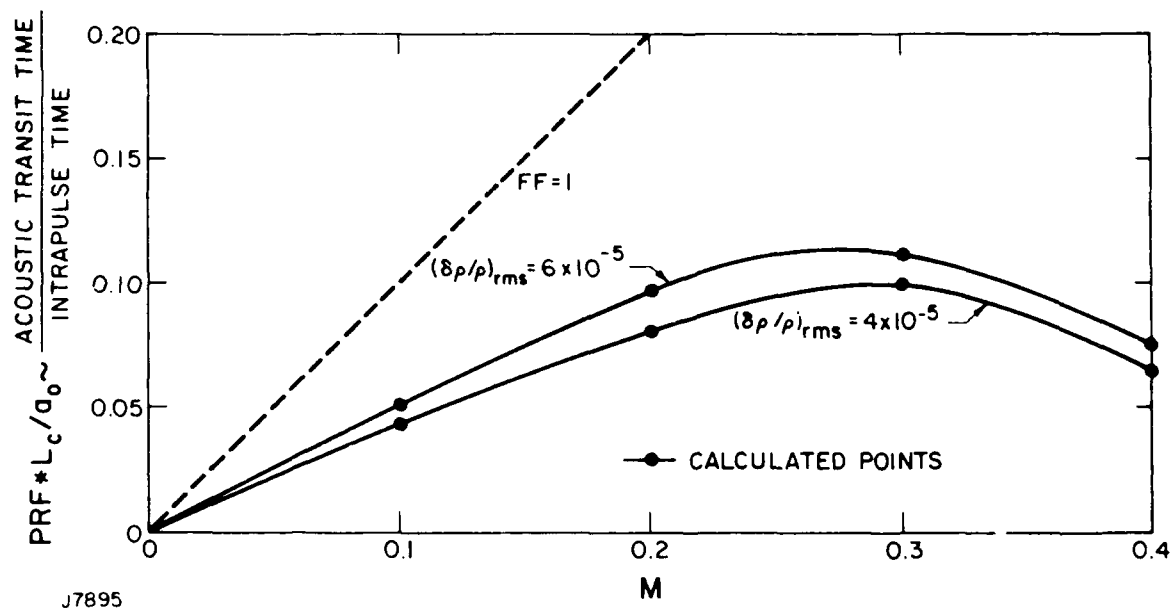
Figure 27.   Theoretical Flow Clearing Map

Entropy disturbances from the muffler arise when gas in the upstream flow channel is recompressed after passage of the rarefaction wave from the cavity. A key question is whether those disturbances can be confined outside the optical mode volume so they will not impact flow clearing time. This has been addressed experimentally, as part of an AERL IRAD program, in the shock tube arrangement shown schematically in Figure 28. Schlieren photos in Figure 29 show that entropy production is not a bulk process in the flow channel. Rather it is only associated with laser gas that has undergone irreversible processes in going into and returning from the backing volume. The penetration depth is around 1 cm in these experiments because a relatively strong shock wave ($\Delta p/p_i \sim 0.4$) is employed to assure good resolution. There appears to be a real possibility of confining entropy waves to the vicinity of the sidewalls and hence approaching the ideal flush factor of one. Further study on Humdinger, Jr is planned.

2.4.4 Transverse Wave Clearing

Acoustic waves also arise which move predominantly transverse to the flow direction. There are several sources: initially nonuniform energy deposition in the cavity, interaction of longitudinal waves with the nearby sidewall mufflers, and re-radiation of acoustic energy from the impulsively loaded e-beam foils. While these waves are relatively weak initially, they also decay quite slowly without acoustic treatment ($\sim t^{-1/2}$) and can be of dominant importance later in the intrapulse clearing process. Their treatment is made less straightforward by the use of two opposed e-beams because this removes the possibility of placing an efficient absorber within the cavity. Transverse waves must get out of the cavity by radiation.

One simple way to speed the radiative process is to cant the sidewalls with respect to the flow axis. This belongs to a more general class of flow channel and variations which will "walk" transverse waves out of the laser cavity. To avoid boundary layer separation this is best done by converging the flow channel. In order to assess the utility of this scheme a theoretical model has been constructed[10] for the idealized configurations shown in Figure 30, involving no baseline flow. Typical results for decay of

---

10. Knight, C., "Transverse Acoustic Waves in Pulsed Lasers," AIAA Paper 81-1283, 14th Fluid and Plasma Dynamics Conf., June, 1981.
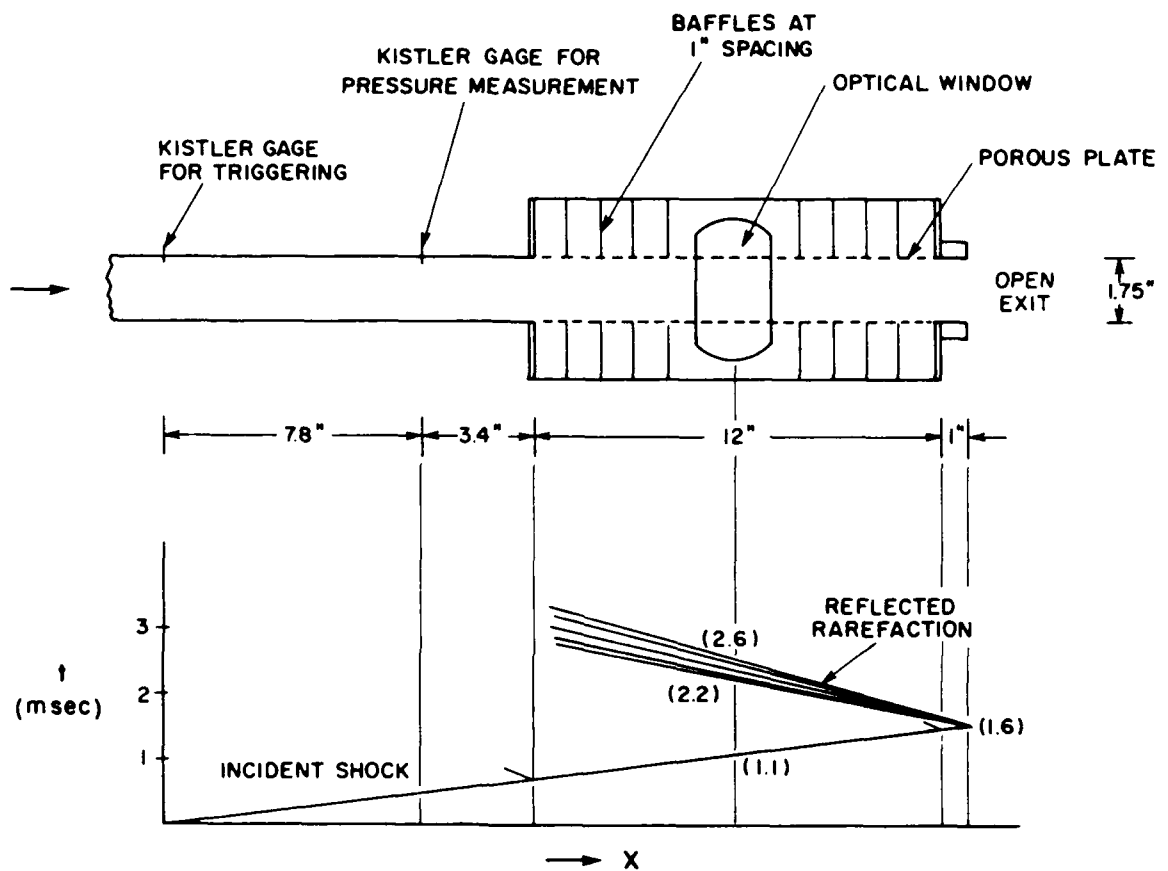
Figure 28.   Schematic of Experiment and Wave Diagram (AERL IRAD, 1981)

(OPEN AREA = 4% , HOLE DIAMETER = 50 MIL)

2.6 msec   3.0   3.5   4.0

4.5   5.0   5.5   6.0
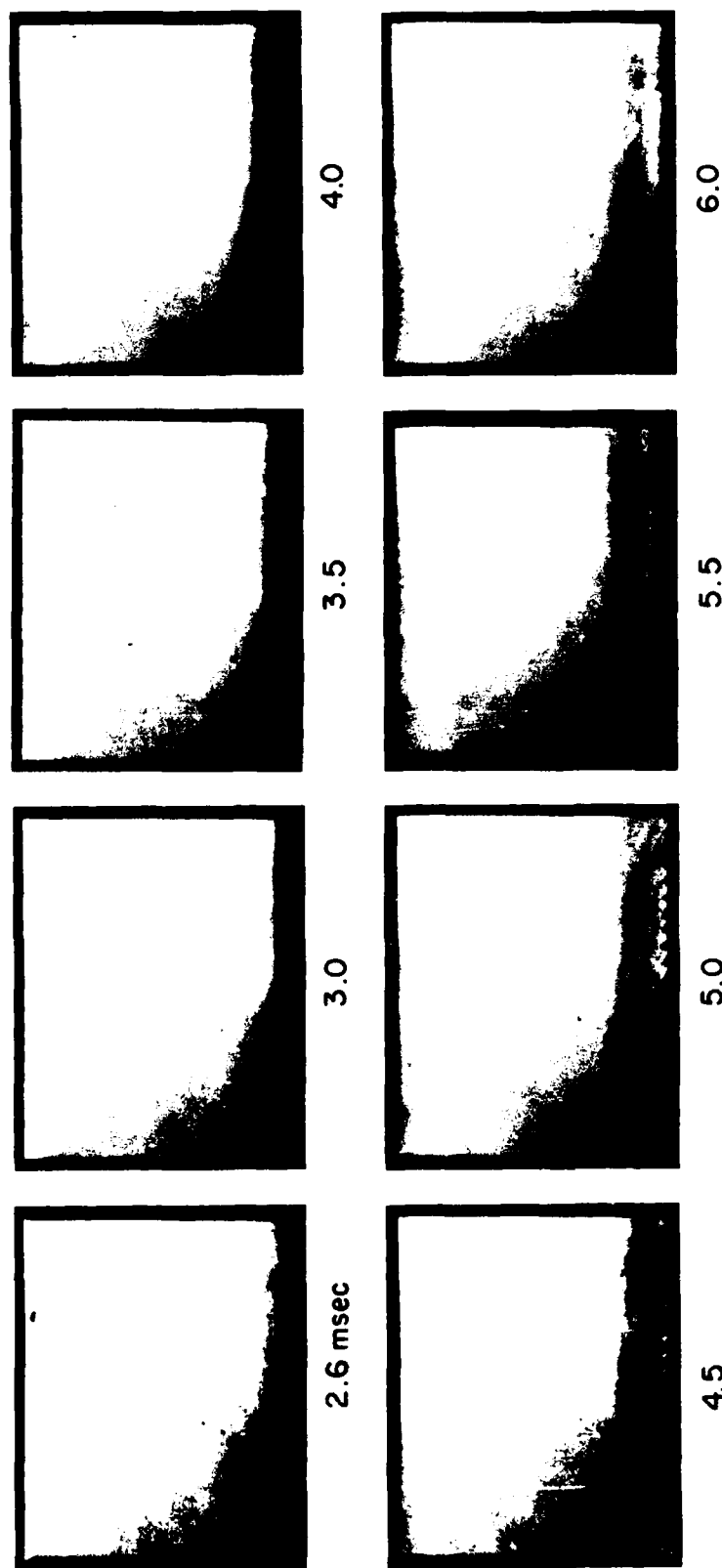
Figure 29.   Shock Tube Study on Entropy Wave Confinement (AERL IRAD, 1981)

K1488

85

AVCO EVERETT
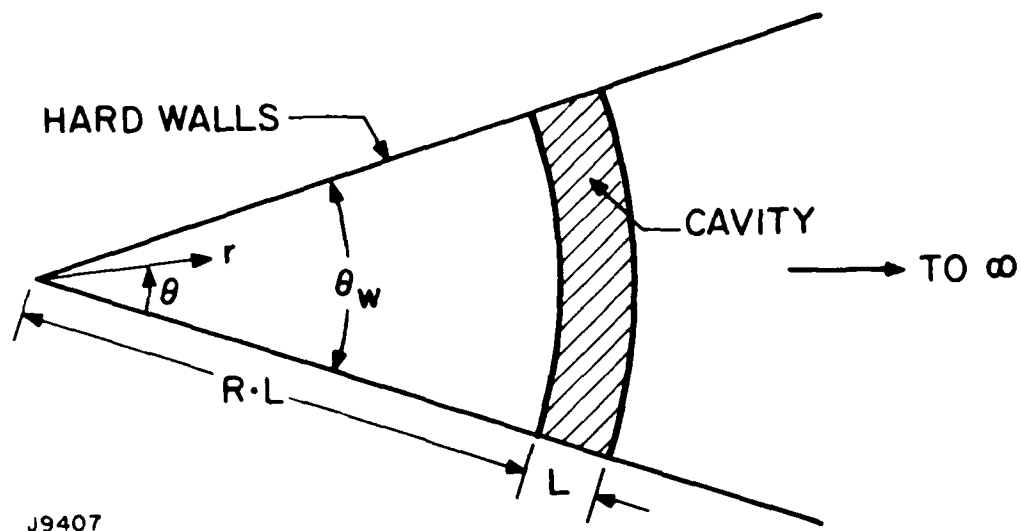
Figure 30.   Idealized Configuration with Canted Sidewalls

J9407

transverse wave energy within the "cavity" are given in Figure 31 for a repre-
sentative nonuniform energy deposition initially, with θ_w in radians.
Fairly large sidewall cant angle is necessary to have a strong effect on
transverse wave clearing. Canted sidewalls will generate baseline flow in-
homogeneity involving higher order spherical aberrations which would not be
easy to correct optically. This scheme is thus not a panacea, and it is prob-
ably preferable to employ a constant area flow channel near the laser cavity
if possible.

The sidewall mufflers can be designed to rapidly attenuate transverse
waves once they are in the muffler section. In the Humdinger, Jr system this
is accomplished by packing and backing volume with porous acoustic absorbing
material of suitable resistivity. That also minimizes transverse reverbera-
tions when a longitudinal wave interacts with the muffler, as seen in Figure
32. It is an open issue whether radiation with parallel sidewalls in the cav-
ity together with close-in mufflers will assure adequate transverse wave decay
for the Phase I-A device. Experimental results from the modified Humdinger,
Jr system are expected during the summer of 1982.

Ordinary acoustic absorbers cannot be used in the XeF laser system due
to material compatibility considerations. Yet from the preceding discussion
it is clear that a treatment of some sort is desirable to achieve good
acoustic performance, especially in terms of transverse wave damping. This is
an issue which has not been addressed in prior technology efforts and will
require further study in the near future.

2.4.5 Acoustics System Synthesis

Boundary layers within the laser cavity reduce the optically usable
volume and hence impact system efficiency and utility. Boundary layer control
in the Phase I-A device can be accomplished by a combination of flow channel
contraction and suction in the upstream muffler. Boundary layer suction has
been studied at AERL as part of the flow technology program, with typical re-
sults shown in Figure 33. About 7 percent mass removal through the perforated
sidewalls is required for $_M/H \sim 5$ to assure negligible boundary layer
thickness at the upstream muffler exit. The boundary layer re-establishes it-
self downstream in the cavity, but the total thickness is much less than it
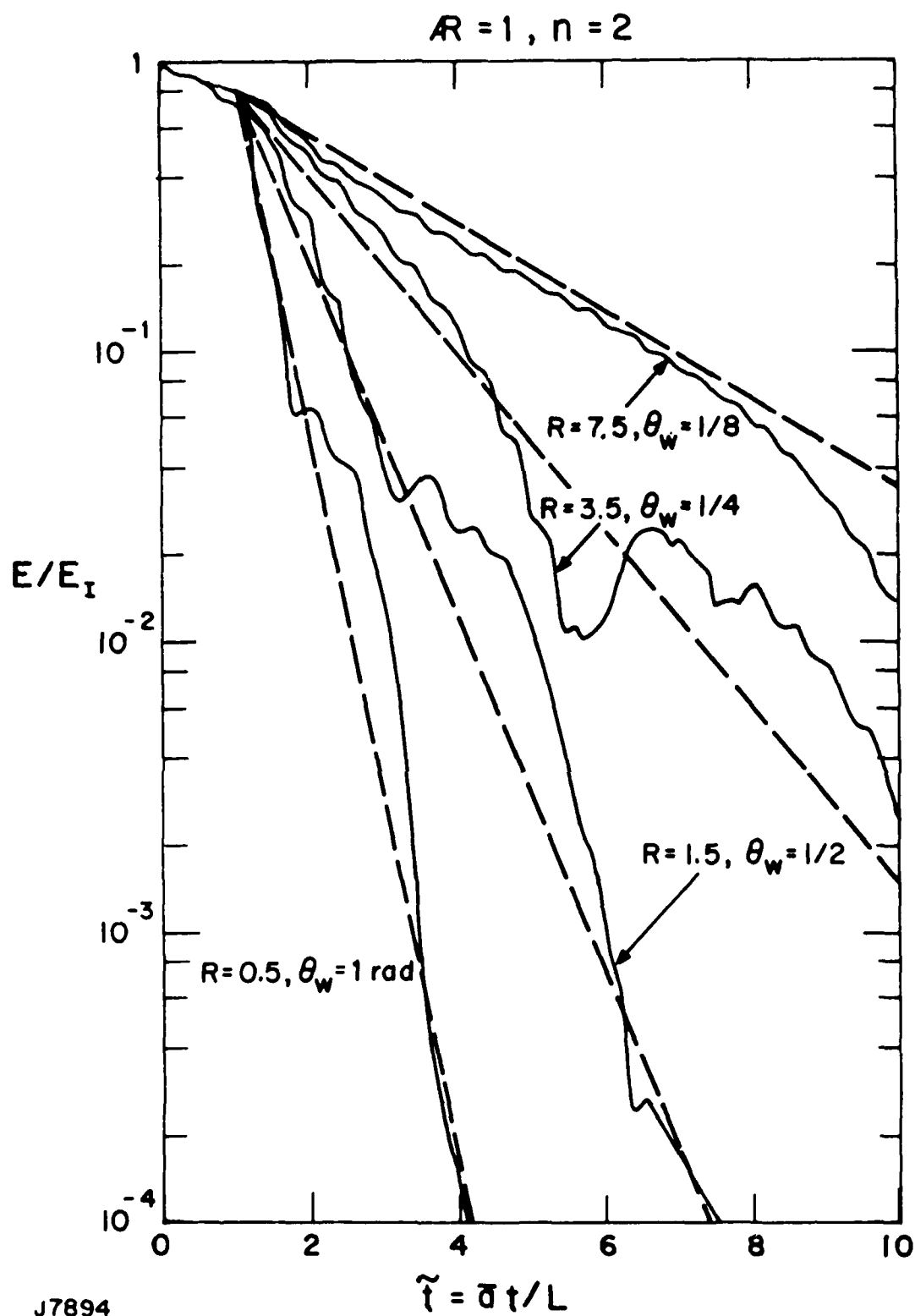
Figure 31.   Transverse Acoustic Energy Decay between Canted Sidewalls

IMPROVED PERFORMANCE WITH ABSORBER IN BACKING VOLUME

$$\left(\frac{\Delta pi}{\bar{p}} = 0.4, \quad \alpha = 0.27, \quad \frac{2h}{H} = 1.6 \right)$$

SHADOWGRAPHS WITHOUT POROUS ABSORBER
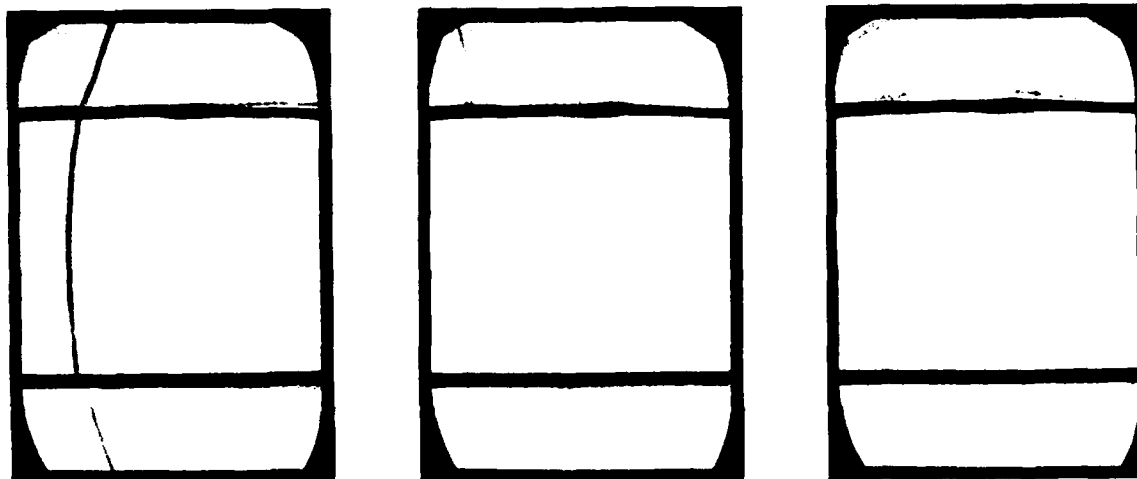
SHADOWGRAPHS WITH ABSORBER IN BACKING VOLUME
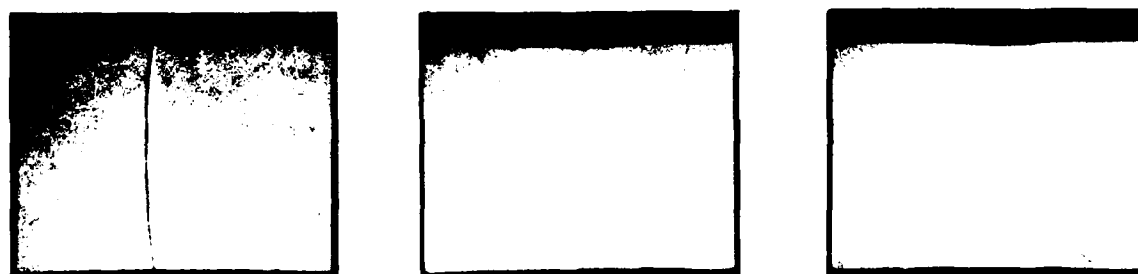
| 1.1 msec | 1.3 | 1.5 |

K1489

Figure 32.   Shock Tube Study on Sidewall Muffler Design (AERL IRAD, 1981)

BOUNDARY LAYER THICKNESS vs SUCTION RATE
(24% OPEN WITH BRUNSMAT)
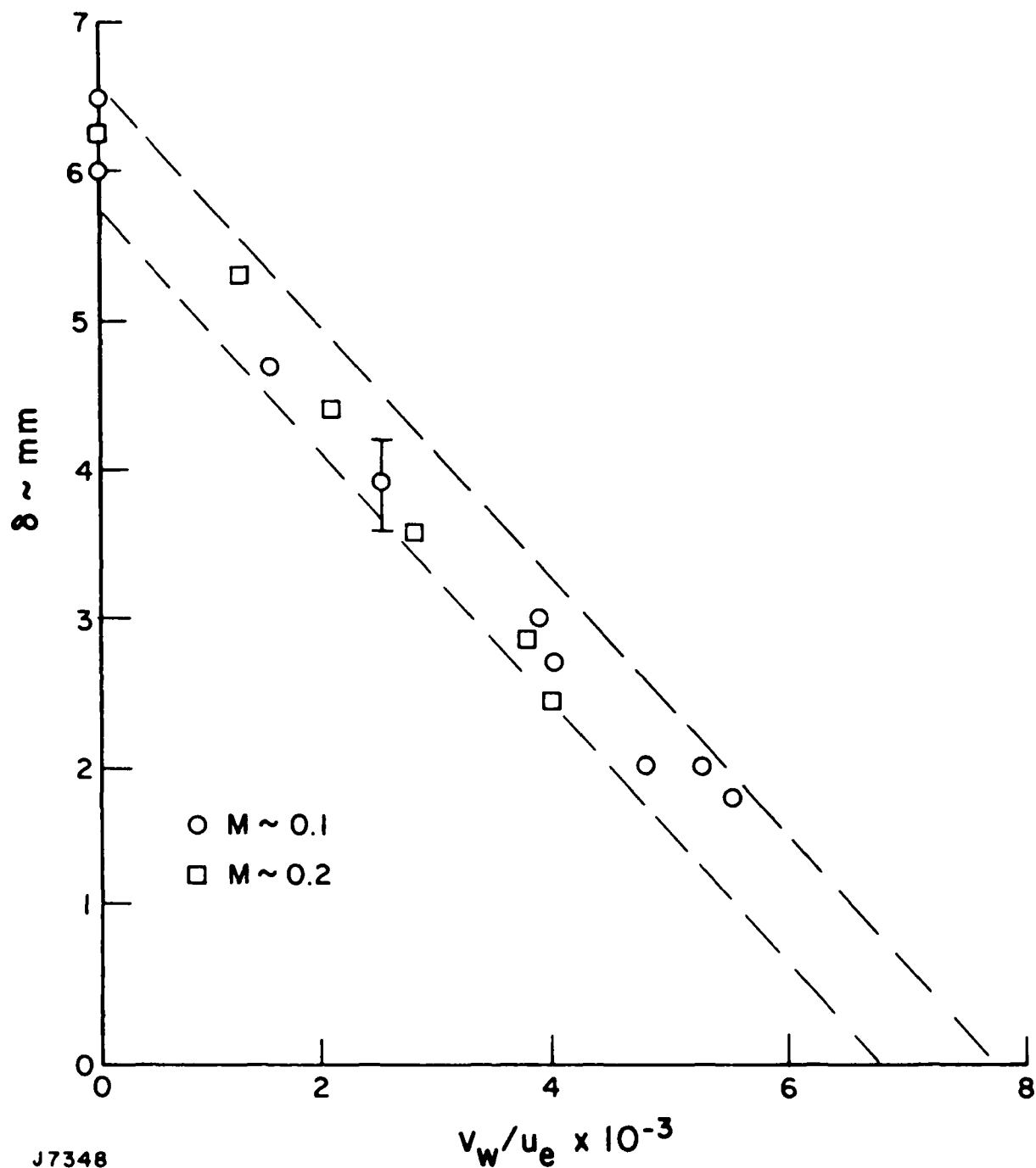
J7348

Figure 33.   Subscale Experiments on Suction at AERL

90

would be without suction. The mass removed through the upstream muffler could be diverted into the gas regenerator system before returning to the flow loop, if that is deemed appropriate for the overall laser system.

A schematic of the overall acoustics system contemplated for the Phase I-A device is shown in Figure 34. The primary mufflers have been extended into the contraction and diffuser sections in this design concept to render the overall system more compact. It also avoids having a long constant area duct upstream of the cavity which would increase the required suction mass flow for boundary layer control. Boundary layer control is also shown in the upstream portion of the diffuser section, followed by vanes. This sort of arrangement was demonstrated experimentally in the Phase "0" ALS system at AERL, sponsored by AFWL.

Flow bypass through the mufflers has the benefit of removing a portion of the acoustic energy dissipated within the mufflers. A combination of that and active cooling elements within the backing volume would be needed for long term operation. Another benefit upstream is the reduction in thickness of the entropy-disturbed region, discussed earlier, before it reaches the laser cavity.

Acoustic waves will be transmitted outside the primary mufflers. This leads to two considerations. First, they can interact with upstream flow conditioning elements such as screens and the thermal stabilizer. The resulting entropy disturbances must be kept below tolerable levels because their origin is far from the cavity. That will be addressed more later. Attenuators on the return leg can be employed to assure no deleterious pressure waves make the circuit around the flow loop. These could also deal with flow related acoustic noise such as that arising from the fan. The secondary attenuator would presumably be tuned to handle longer wavelengths. Effective shielding of the cavity by the primary mufflers has been demonstrated in Humdinger, Jr for shorter wavelength components.

FLOW/ACOUSTICS IN A CLOSED-CYCLE DEVICE
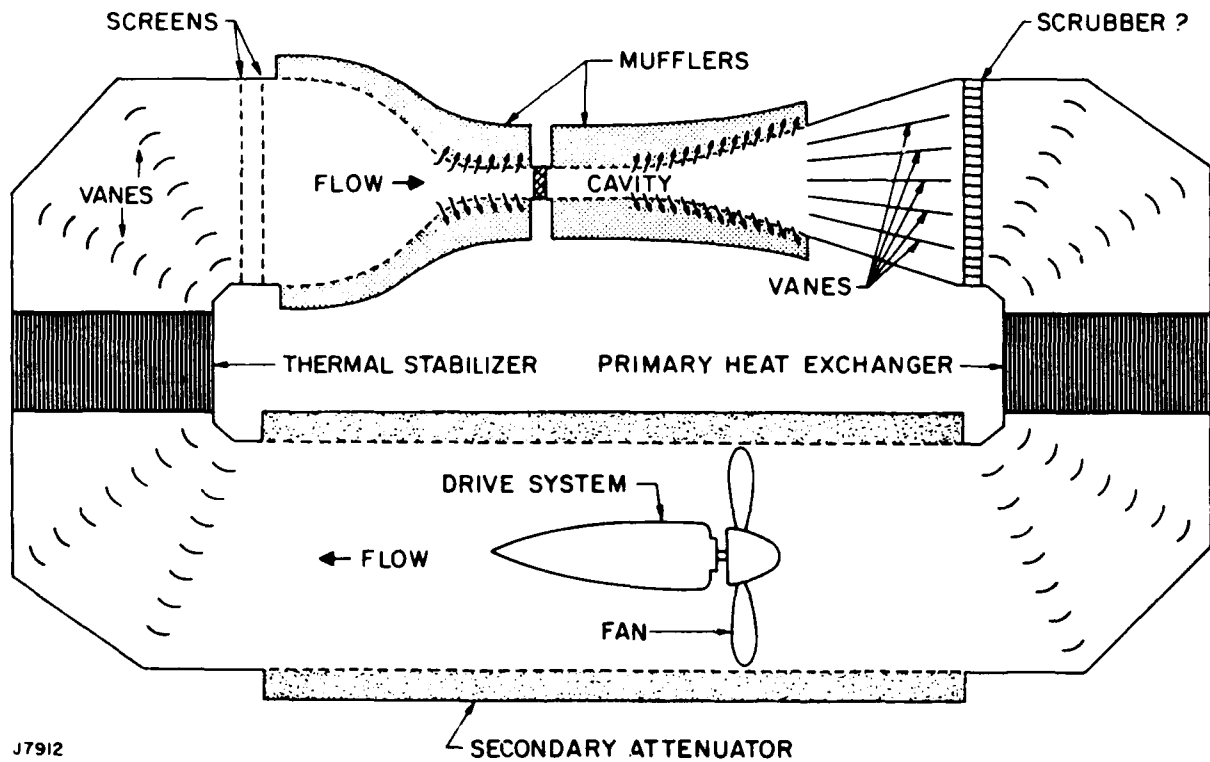
J7912

Figure 34. Overall Acoustics Design Concept

2.5 GAS RECIRCULATOR

The gas recirculator supports cavity requirements by providing gas flow to the cavity subsystem with adequate thermal and velocity uniformity to meet cavity medium homogeneity requirements. This will be done in a manner consistent with minimum flow power requirements, minimum flow-loop volume, tunability of loop components, access for easy serviceability and high reliability. The gas recirculator will also provide suitable cavity gas chemical composition through a gas processor subsystem.

The baseline design consists of a single 1.012 pressure ratio, elevated temperature, 6 atm neon circulating fan; an excimer gas heat exchanger; an excimer gas thermal equalizer; a wire grid velocity equalizer; and various ducts, diffusers, bellows and vaned turns.

The flow system interfaces with the cavity upstream of the flow stabilizer and downstream of the vaned cavity diffuser. The flow loop is a modular design, all welded construction with a minimum of flanged joints. Only those sections requiring tuning and maintenance employ flanges for accessibility. The bends and diffusers are vaned to minimize volume, head loss and fluid turbulence.

Component arrangements and sizing are designed in view of trade-offs between flow loop volume and fan power requirements. Modular component design will allow system tuning. For example, the thermal equalizer will be composed of several self-contained modules so that the required degree of equalization may be determined during testing.

Acoustic attenuators may be required in the flow loop to augment primary mufflers. These wall absorbers will serve to suppress long pressure waves ($\sim$ 1.0 to 10.0 m) emanating from the cavity and shorter waves generated by the fan and other flow loop components.

Flow loop control requirements and technical approach will vary as a function of the stages of development which are identified as follows:

1. Component testing
2. Subsystem assembly testing
3. Integrated system shakedown
4. System operation

Many diagnostics will be used during stages 1 through 3 and then be greatly reduced as we proceed to an operating system in stage 4.

In the subsystem assembly test phase, required data acquisition rates of the order of seconds or longer in most cases will suffice. Certain temperature measurements that relate to thermal conditioning control will require time resolution of the order to 100 ms. Shakedown testing of the integrated system will require additional temperature diagnostics related to system fault protection.

2.5.1 Flow Loop Requirements

The gas recirculator subsystem must be designed to meet the cavity medium homogeneity and gas composition quality requirements ($\Delta\rho/\rho \leq 3 \times 10^{-5}$ and ≤ 20 percent performance degradation in 1 min) with a minimum of fan power (to meet overall efficiency requirements) and minimum volume (for cost effectiveness and ease of operation). The system must also be designed for easy maintenance and serviceability, and test operation flexibility.

The main flow loop controls must control the loop pressure, temperature, and velocity. The loop pressure, supplied from the pressure maintenance subsystem, will be controlled to ± 0.068 atm within an adjustable range of 3.5 to 6 atm. The laser gas temperature, controlled by the thermal maintenance subsystem, can be maintained to within $2.5°C$ over a range of 300 to $450°K$. The laser gas velocity, controlled by the variable speed two-stage axial fan, will be maintained to within 2.5 percent of the set point over an operating Mach number range from 0.05 to 0.11 at the entrance of the cavity.

The cavity gas homogeneity requirement ($\Delta\rho/\rho < 3 \times 10^{-5}$) is the critical requirement of the loop. All components in the loop affect the gas homogeneity and therefore each must be designed to minimize the nonuniformities in the cavity. The thermal equalizer and the velocity equalizer located just upstream of the acoustics subsystem interface, are the primary homogeneity control devices in the loop.

2.5.2 Flow Loop Arrangement

The XeF gas flow loop has been broken down into 21 separate components and their arrangement is shown in Figure 35. The loop will interface with the

94

THERMAL EQUALIZER

PLAN VIEW

THERMAL EQUALIZER
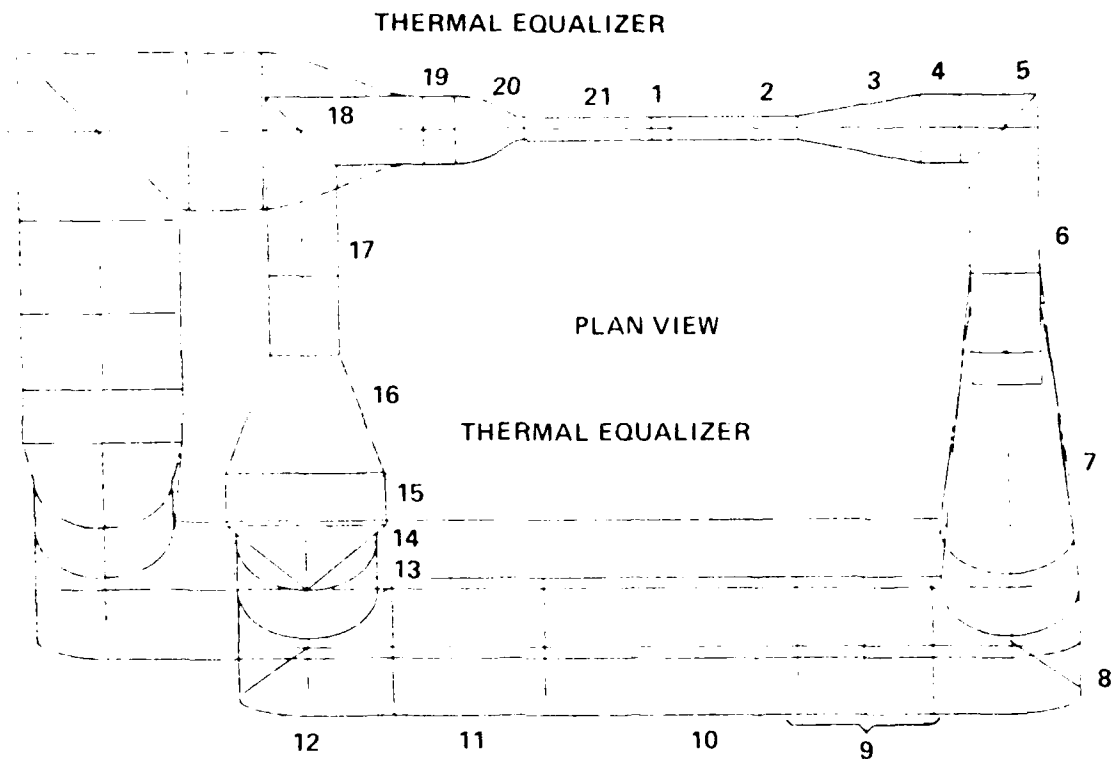
FLOW LOOP ELEMENTS

1 CAVITY	8 BEND (CIRC)	15 EQUALIZER
2 D/S MUFFLER	9 BELLOWS & MUFFLER	16 TRANSITION
3 DIFFUSER	10 FAN	17 BEND (VERT)
4 HEAT EXCHANGER	11 FAN DIFFUSER	18 BEND (HOR)
5 BEND (HORIZONTAL)	12 BEND (CIRC)	19 FLOW STABILIZER
6 BEND (VERTICAL)	13 BELLOWS	20 NOZZLE
7 TRANSITION (RECT–CIRC)	14 TRANSITION (CIRC–RECT)	21 U/S MUFFLER

K2965

Figure 35.   Flow Loop Configuration Options

cavity upstream of the converging nozzle (20) and downstream of the cavity diffuser (3). The bends and diffuser are vaned to minimize system head loss and to provide maximum gas homogeneity through the loop.

Loop component sizes are dictated by cavity gas homogeneity requirements and by flow power considerations. The lengths of the legs of the loop are dictated by component sizes such as the bellows, round to rectangular transitions, the thermal equalizer, and convergent and divergent transition sections. Final location of the thermal equalizer is yet to be determined.

Two peripheral gas handling subsystems are connected directly to the flow loop: the gas processor system, and the pressure maintenance system. The gas processor system will remove gas from the discharge of the fan, pass it through the scrubber, and return it to the loop upstream of the heat exchanger. The pressure maintenance system will be attached upstream of the heat exchanger.

2.5.3 Loop Assembly, Accessibility and Serviceability

The loop will be fabricated in sections with provisions to allow components to be removed for service. Connections will be made with flanges with metal seals backed by viton seals. All of the components can be individually removed from the system for maintenance. Since the cathode and foil assemblies may require considerable maintenance, they will be mounted on wheels so they can be easily rolled back on rails. An entire e-beam assembly including foil, cathode, vacuum box and pumps will move as a unit. The fan and fan drive assembly will also be removable as a unit. Modular component design will be stressed to allow system tuning. For example, the thermal equalizer will be composed of several self-contained modules so that the required degree of equalization may be determined during subsystem testing.

2.5.4 Loop Materials

Two classes of materials will be considered for the walls of the loop. The two material classes are aluminum alloys and 18-8 CRES steels (300 series steels). From the fabrication cost standpoint, 18-8 CRES steels are the preferred materials. Aluminum alloys will only be used if the diffusion rate of carbon in 18-8 steels at the operating temperature of 450K is high enough for the carbon in the 18-8 steels to be a source of laser gas contamination.

2.5.5 Thermal Conditioning

Cavity medium homogeneity is influenced by gas recirculator thermal conditioning in three ways:

1. Degree of thermal equilibration between gas heated by the e-beam and that which is not heated.

2. Degree of temperature balance between the gas and solid surfaces in the loop.

3. Entropy disturbances resulting from the interaction of pressure waves with flow loop components.

These consideration influence design and arrangements of flow loop components.

Gas thermal conditioning will be achieved by two heat transfer components with separate functions. A compact heat exchanger, located directly downstream from the flow channel diffuser, will remove all energy deposited in the gas. This heat exchanger will control average gas temperature but will leave substantial differences in gas temperature between gas slugs that are heated by the e-beam and gas which passes through the cavity unheated. A second heat exchanger of much larger size will remove no net energy from the gas but will serve to equalize temperature both temporally and spatially between the e-beam heated and unheated gas slugs. This thermal equalizer will be located downstream from the fan and thereby diminish gas temperature variations introduced by the fan itself. Entropy disturbances are introduced by pressure waves at the discharge end of the thermal equalizer. The required dwell time for subsequent turbulent dissipation of those disturbances may dictate its precise location.

The thermal equalizer will be made up of several independent segments stacked in the flow direction. This approach allows rapid reconfiguration of the equalizer if early testing indicates changes are desired. Average power removal (100 pps operation) by the heat exchanger requires a mean gas temperature reduction of 13.3°C. Temperature variation between e-beam heated gas slugs and unheated slugs is 49°C. After passage through the heat exchanger this heated to unheated gas Δ T is reduced to 36°C.

To meet the beam quality requirement of 1.3 XDL at the output aperture ordered thermal inhomogeneities in the XeF laser cavity must be held to

97

$$(\Delta T/T_c)_{RMS} \leq 2 \times 10^{-5} \qquad (28)$$

This corresponds to an RMS temperature variation of < 0.01 C for a cavity gas temperature of $450°K$. For randomly distributed disturbances on a mean spatial scale Λ, requirements are met if this magnitude of thermal fluctuation is held to

$$(\Delta T/T_c)_{RMS} \Lambda^{1/2} \leq 2.4 \times 10^{-4} \; cm^{1/2} \qquad (29)$$

Peak variations between heated and unheated gas slugs at the heat exchanger exit of $36°C$ correspond to RMS variations of $\sim 12.7°C$. Turbulence introduced by the heat exchanger will cause both a reduction in magnitude of these variations and a change in their spatial scale in transit from heat exchanger exit to cavity entry. By analogy with measurements by Sreenivasan[11] et al., of decay of temperature fluctuations downstream from a heated grid, it is conservatively estimated that mixing alone will reduce the magnitude of these temperature variations by a factor of 0.06 with an attendant length scale of < 13 cm.

Thus, if there were no additional means of thermal equilibration, cavity conditions would be

$$(\Delta T/T_c)_{RMS} \Lambda^{1/2} \leq 6.1 \times 10^{-3} \; cm^{1/2}$$

In comparison with the requirements of Eq. (29), one sees the need for an additional reduction in fluctuation between heated and unheated gas slugs of possibly a factor of 0.04.

The thermal equalizer, described above, serves to provide the required additional reduction in magnitude of temperature fluctuations. Since this equalizer will be built up as segments, a conservative example of ten segments

11. Sreenivasan, K.R., Tavoularis, S., Henry, R., and Corrsin, S., J.F.M. Vol. 100, p 597 (1980)

is considered. For reasons of flow power reduction the inlet area of the
thermal equalizer is chosen as seven times the cavity flow cross section.
This will allow operation with all equalizer segments installed with a moder-
ate pressure drop of 0.65 cavity dynamic heads. Performance calculations show
a predicted reduction in temperature fluctuations between inlet and outlet of
the thermal equalizer of a factor of 0.007. This greatly exceeds the required
factor of 0.04 and suggests that subsystem tests will demonstrate that fewer
segments are required.

Temperature differences between the gas and solid walls in the gas re-
circulator may introduce thermal inhomogeneities through turbulent wall bound-
ary layers. The thermal equalizer will wash out such disturbances which may
occur upstream from its entry. Consequently, the region of primary considera-
tion is the gas recirculator outside wall between the thermal equalizer and
the nozzle entry. This boundary layer will become part of the main core flow
after rapid acceleration through the nozzle; hence associated thermal fluctua-
tions can not be removed by boundary layer suction in the upstream muffler.

On the basis of local flow conditions and studies reported by Schlicting[12],
turbulent boundary layer growth from the thermal equalizer exit to the nozzle
entry reaches a thickness of 4.4 cm. The associated mean scale for turbulent
temperature fluctuation is $\sim \Lambda = 0.9$ cm and the magnitude of RMS temperature
fluctuations is ~ 0.078 times the total temperature difference across the
layer, $(T_g - T_w)$.[13] At a gas temperature of $450°K$ one can thus evaluate
the parameter

$$\left(\frac{\Delta T}{T}\right)_{RMS} \Lambda^{1/2} \simeq 1.64 \times 10^{-4} |T_g - T_w|$$

in terms of $(T_g - T_w)$. If this is equated with the cavity medium homo-
geneity requirement Eq. (29) one establishes the maximum allowed gas/wall
temperature difference

12. Schlicting, H., Boundary Layer Theory, Pergamon Press, N.Y., 1955.

13. Hinze, J.O., Turbulence, McGraw Hill, N.Y., 1975

$$|T_g - T_w| \leq 1.5°C$$

which will satisfy cavity homogeneity requirements. This analysis is conservative (stringent) since it ignores decay of temperature fluctuation in transit from nozzle entry to cavity.

A velocity equalizer, likely consisting of a series of screens, will be located between the final flow turn and the entry to the converging nozzle. This velocity equalizer will serve to suppress turbulent velocity fluctuations and also ordered velocity variations in the laser cavity.

Density nonuniformity in the cavity may be influenced by flow velocity variations through compressibility effects. Flow turbulence will introduce density fluctuations according to the relation[13]

$$\left(\frac{\delta\rho}{\rho}\right) = 0.7 \, M_c^2 \left(\frac{\delta u}{u}\right)^2 \tag{30}$$

where M_c is flow Mach number.

Ordered velocity variations in the inviscid core flow will introduce density variations through the condition of constant stagnation enthalpy as,

$$\frac{\delta\rho}{\rho} = M_c^2 \, \frac{\delta u}{u} \tag{31}$$

The total optics budget for XeF cavity medium homogeneity is $\delta\rho/\rho < 3 \times 10^{-5}$ (rms) for ordered disturbance. Here we assign a portion of 1.0×10^{-5} (rms) to effects of ordered velocity variations. At XeF integrator baseline operation, $M_c = 0.086$, hence the allowed variations in cavity flow velocity is, from Eq. (31)

$$\left(\frac{\delta u}{u}\right)_c \leq 1.35 \times 10^{-3} \text{ (rms)}$$

This is related to allowed ordered velocity variation at the nozzle entry through Bernoullis Equation as

$$\left(\frac{\delta u}{u}\right)_n \le 1.22 \times 10^{-2} \text{ (rms)} = 3.4 \times 10^{-2} \text{ (PTP)} \qquad (32)$$

for a nozzle contraction ratio of 3.0. This provides one basis for selection of velocity equalizer performance. Measurements by Schubauer, et al.[14] show effects of screens on reduction of highly ordered incident velocity variations for a variety of screen loss factors K (K = screen pressure drop normalized to incident dynamic pressure). A loss factor of K > 1.5 will reduce ordered velocity variations by a factor of < 0.2. With this baseline design criterion and the requirement of Eq. (32), the allowed ordered velocity variation at the exit to the final turn is,

$$\left(\frac{\delta u}{u}\right)_T \le 0.17 \text{ (PTP)}$$

This criterion may be satisfied by reasonably careful installation of turning vanes of good design.

Flow turbulence will persist on a length scale of the order of the spacing of vanes on the final upstream turn. For the XeF integrator baseline system this spacing will be ~ 2.5 cm. Associated density distrubances are random, thus a budget for the phenomenon may be taken as

$$\left(\frac{\delta \rho}{\rho}\right)_{rms} \le 1.0 \times 10^{-5} \left(\frac{150}{2.5}\right)^{1/2} = 7.7 \times 10^{-5}$$

where 150 cm is the distance between cavity windows in the baseline design. The magnitude of allowed turbulent velocity fluctuations in the cavity thus is obtained from Eq. (30) as

14. Schubauer, G.B., and Spangenberg, W.G., and Krebanoff, P.S., N.A.C.A.T.N. 2001, (Jan. 1950).

$$\left(\frac{\delta u}{u}\right)_c \leq 1.5 \times 10^{-2}$$

Decay of turbulent fluctuations in transit from the final turn to the cavity may be inferred from grid turbulence measurements of Sreenivasan[11] to yield a conservative estimate.

$$\left(\frac{\delta u}{u}\right)_c \leq 1.4 \times 10^{-2}$$

A velocity equalizer with a loss factor, $K > 1.5$, will further reduce the turbulence fluctuation by a factor of order 0.5.

Control and reduction of ordered velocity variation is concluded to be the primary criterion for velocity equalizer design. These ordered velocity variations may be controlled to meet cavity homogeneity requirements by using established turning vane design and testing procedures and by use of a velocity equalizer with a pressure loss factor > 1.5.

Thermal conditioning must deal with the reentry of gas from the gas processor. This gas return will be located upstream from the heat exchanger along the non-diverging walls of the main channel diffuser. Consideration must also be given to temperature variations which may be small in magnitude but highly ordered. Gas flow between the cavity windows and the region of e-beam deposition undergoes no deposition heating and thus has a lower average temperature at entry to the heat exchanger. Heat exchanger operation may compensate for these effects by restricted coolant flow near the non-diverging walls of the main channel diffuser. Coolant temperature increase between entry and exit to the heat exchanger will introduce minimal ordered temperature variation in the gas if counterflow operation is employed.

2.5.6 Flow Conditioning

Cavity medium homogeneity may be influenced by gas recirculator flow conditioning. Acoustic disturbances produced in the flow loop may degrade cavity medium homogeneity.

There are several sources of acoustic noise within the closed-loop XeF flow system. Turbulent boundary layers produce significant pressure fluctuations, especially in the high velocity sections, and wake noise will arise from high blockage elements such as the heat exchangers. Flow noise can also be expected from the blades of the vane-axial fan, especially if it is exposed to gas slugs with somewhat variable temperature. There are also disturbances associated with the laser cavity. Residual acoustics will also be transmitted outside of the primary mufflers. Finally, loop surge phenomena can arise which excite organ pipe modes between large Δp elements in the flow loop.

The cavity should be well shielded from shorter wavelength acoustic components by the primary mufflers immediately upstream and downstream of the laser cavity. At the other end of the spectrum, extremely long wavelength components (compared to the cavity) should not be of optical concern because only a small segment of them will be in the cavity at any given time. Intermediate wavelength components (comparable to or somewhat longer than the primary mufflers) are the ones that must be dealt with. They will be relatively slowly damped by the mufflers. Also, although they are long compared to the cavity, they can still introduce significant beam jitter.

The secondary acoustics system will have to assure that the amplitude of acoustic components with wavelengths in the range of 1.0 to 10.0 m does not become excessive. For the XeF laser mix, this translates into a frequency regime of 50-500 Hz. The amplitude of the lower frequency components can be allowed to be larger for the same effect on beam quality, so some loss of effectiveness at lower frequency can be tolerated.

The flow loop will be designed for minimum head loss and thus maximum efficiency. The total loop $\Delta p/q_c$ is < 2, leaving margin in the fan for the addition of velocity equalizer segments and/or the relocation of the thermal equalizer if it is required.

Commercial fans and motors are not designed to operate under these temperature, pressure and hazardous fluid conditions. Modifications of the seals, *bearings and motor will be required. The fan will deliver 24,000 ft^3/min neon flow at 27 in H$_2$O pressure rise at an efficiency > 78 percent. The elbows, both rectangular and round, and diffusers will be vaned to reduce the head losses and to maximize the gas homogeneity. The precise number and shape of the vanes is yet to be determined during PDR. The fan exit will have a diffuser with a 1:3 area ratio, minimum loss, design.*

2.5.7 Gas Recirculator Controls and Diagnostics

During full system operation there are only three data features of the gas recirculator which relate to laser device performance, cavity gas temperature and pressure, and gas flow rate as it relates to flush factor. Other diagnostics, as required, will relate to gas recirculator subsystem control, operational control, and fault protection.

Four flow features will be controlled at the subsystem level:

(1) Gas Flow Rate

(2) Cavity Gas Temperature

(3) Gas Temperature Uniformity

(4) Cavity Gas Pressure

Gas flow rate will be measured with a calibrated pitot static pressure probe. The control signal (dc voltage) from the signal conditioner of its differential pressure transducer will be compared to a set reference voltage provided by operational control. This voltage difference will drive a proportional speed regulator in the fan drive system. This feedback circuit will provide stable fan operating speed at any preset value over its operating range within $\pm$ 2 percent.

Cavity gas temperature control will be maintained by control of operation of the heat exchanger at subsystem level. The average gas temperature at the heat exchanger exit will be measured by a series of thermocouples. Signal conditioner output (dc voltage) will be compared to a set reference voltage provided by operational control. The voltage difference will act as the control signal. Liquid coolant will continuously circulate from a reservoir through a three-way valve which directs a portion of the flow to the heat exchanger and the remaining portion back to the reservoir. The valve setting will be adjusted by an electric drive which responds linearly to the input control signal. Since liquid side heat transfer rate varies approximately as flow speed, this system will respond to variations in flow loop gas temperature in < 100 ms. Gas temperature will be held to $\pm$ 0.5°C during a run. Long term drift in reference voltage, however, is permitted to be as large as $\pm$ 2-1/2°C.

Gas recirculator wall temperature will be controlled by active wall heating and wall thermal insulation. Wall temperature must match closely to gas temperature in the region between the downstream end of the thermal equalizer and the converging nozzle to satisfy cavity homogeneity requirements. This is achieved by the circulation of liquid through the thermal equalizer and through wall heater loops from a common reservoir.

The flow loop will be initially pressurized from vacuum with pure neon to the desired density dictated by operational control. Gas fill will continue until it reaches the upper set point of operational control. At this time, slow flow fill and bleed control will take command at subsystem level. On-off fill will occur between upper and lower set points of span of 0.5 psi. On-off bleed will take over above the upper fill set point and will operate over a span of $\pm$ 0.5 psi.

Flow loop warm up employs the thermal equalizer liquid flow loop. An electric heater will be located in the coolant reservoir. Heat capacity of the entire flow loop is $\sim 7 \times 10^6$ J/°C. Consequently a warm up time of 1 hr from room temperature to 450°K requires an average power of 290 kW. The flow loop fan will provide $\simeq$ 100 kW and the warm up heater will provide the remaining $\simeq$ 190 kW. Heater start-up will be initiated by master control. Heat up procedure will be managed at subsystem control level.

Various, safety and system protection related features will be monitored at subsystem level. Upper limit red lines at subsystem level will relay shutdown command to operational control. Cavity gas pressure will also command system shutdown if rate of decrease exceeds a red line indicating large system leakage.

E-beam startup may occur with no further control communication to the gas recirculator subsystem. After arrival of e-beam heated gas to the exit of the heat exchanger the control loop automatically increases the coolant flow rate to maximum pump rate. Cool down of the compact heat exchanger will occur rapidly enough so that transients in gas temperature will be removed by the thermal equalizer.

System cool down will employ a water coolant loop in the liquid reservoir of the thermal equalizer. Cool down to 40°C will be achieved in $\sim$ 1 hr.

105

System emergency shutdown will follow a variety of procedures at system control according to the nature of the red line failure. Flow loop pump down and evacuation, cool down, and fan operation are the major features of this subsystem which are available for us in emergency procedures.

2.6 GAS REGENERATION SYSTEM

2.6.1 Introduction

Laser output will decrease during operation due to contaminants formed by gas phase reactions in the excitation volume and by contaminants from wall reactions. To maintain a specified output level, under repetitively-pulsed conditions, contaminants will have to be continuously scrubbed from the gas mix. This section first describes a system model designed to predict which contaminants will have to be scrubbed and the rates at which they must be removed for both one-minute and ten-hour operation. The results of this model, using the parameters from the conceptual design of the laser identified under this program, will then be presented.

2.6.2 Model

The allowed decrease in output during a run is specified to be no greater than 20 percent. This is translated into allowable levels of specific contaminants by determining their effects on laser performance. The model itself includes the important chemical reactions in the system and their rates, system loop volume and gas flow rates, pulse repetition rate, and the rates at which contaminants can be removed by scrubbers. The output of the model is the predicted level of species concentrations in the excitation volume of the laser as a function of time. The level and type of gas makeup and the level and type of scrubbing are adjusted until the concentrations of the contaminants are below their estimated tolerable limits at a time corresponding to the end of a run.

The model itself is divided into two sections and is shown schematically in Figure 36. The primary section describes the chemical kinetics within the laser itself, both during and after the e-beam excitation, assuming that the gas plug under consideration maintains a constant volume as it flows. This includes the dissociation of the halogen donor by electron attachment and the recombination of various radical species during the relatively long period following the excitation and before the next pulse. This primary section integrates a set of stiff nonlinear equations given the initial species concentrations. The second section of the model is a linear set of equations

107
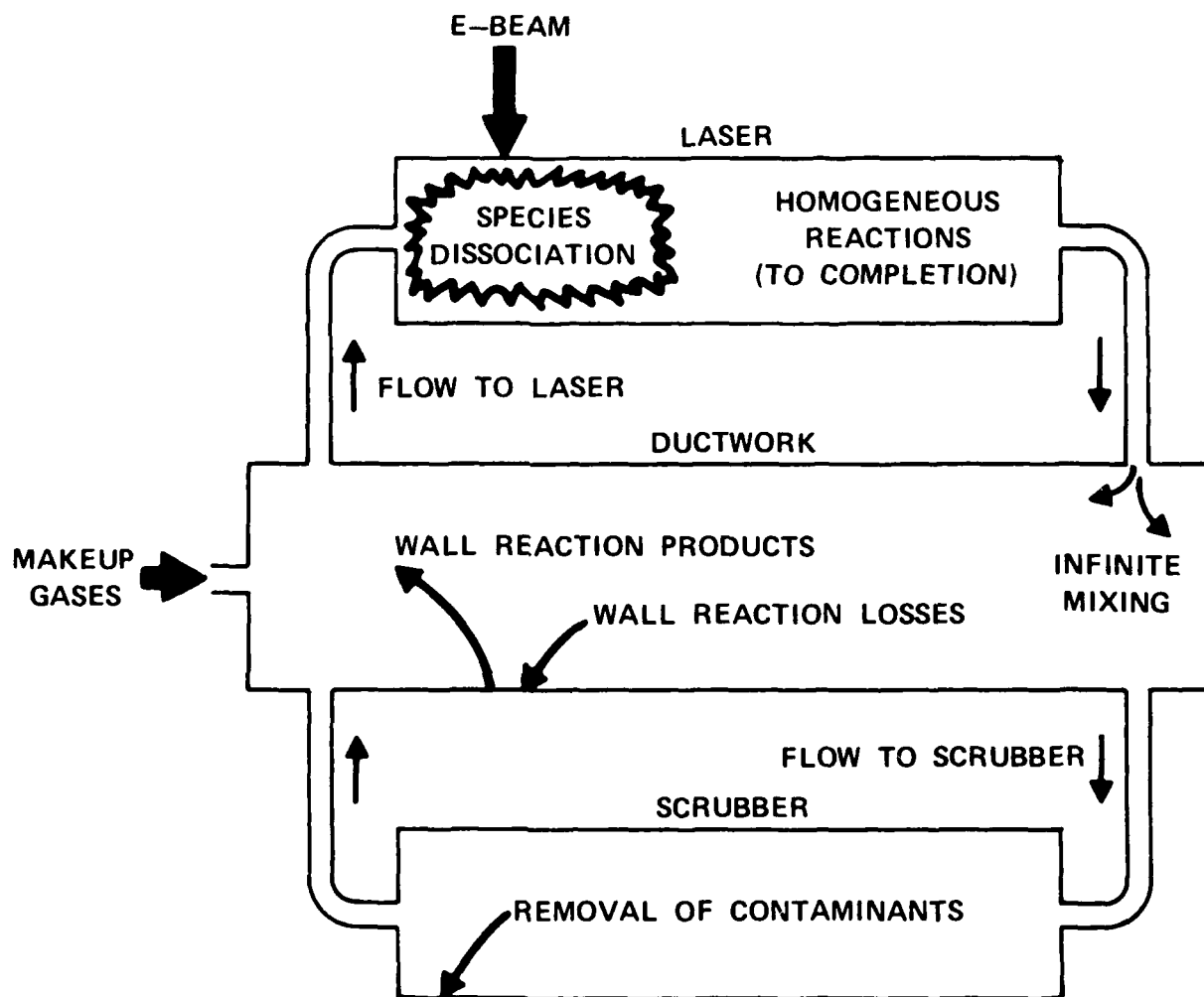
K1414

Figure 36.   Recyclability Model Schematic

which describe the rest of the system as two volumes, ductwork and scrubber, with flow rates connecting them. The gas within these two volumes is assumed to mix infinitely quickly. Provision is made for introducing constant flows of makeup gas into the ductwork.

In the primary section of the model, the following set of reactions is assumed to describe the halogen donor dissociation and the following homogeneous chemistry.

Dissociative Attachment

1.	$NF_3 \rightarrow NF_2 + F^-$	Ref. 15
2.	$NF_3 \rightarrow NF + F^-$	Ref. 16
3.	$NF \rightarrow NF + F^-$	Ref. 16
4.	$F_2 \rightarrow F + F^-$	Ref. 15

Homogeneous Reactions

5.	$NF_2 + F \rightarrow NF_3$	Refs. 17, 23
6.	$F + F \rightarrow F_2$	Refs. 18, 24
7.	$NF + F \rightarrow NF_2$	Ref. 22
8.	$NF + NF \rightarrow N_2 + F + F$	Refs. 19, 25
9.	$NF_2 + F_2 \rightarrow NF_3 + F$	Refs. 20,26,27
10.	$NF + F_2 \rightarrow NF_2 + F$	Ref. 22
11.	$NF + NF_2 \rightarrow N_2F_2 + F$	Refs. 21,28

Wall Reactions

12.	$NF_3 + Wall \rightarrow NF_2$	
13.	$NF_2 + Wall \rightarrow NF$	
14.	$NF + Wall \rightarrow N$	
15.	$F_2 + Wall \rightarrow -$	

15. Trainor, D.W. and Jacob, J.H. Appl. Phys. Lett. 35, 920 (1979).

16. Trainor, D.W. private communication.

17. Tang, K.Y., Hunter, R.O. and Huestis, C.L. to be published in J. Appl. Phys.

18. Ultee, C.J., Chem. Phys. Lett. 46, 336 (1977).

19. Chea, C.T. et al., J. Chem. Soc. Far. Tr. 11, 76, 711 (1980).

20. Avco IRAD (1981).

21. Collins, R.S. and Hussain, D., J. Photochem. 2, 459 (1972).

22. McGeoch, M. private communication.

23. Smith, G.P and Huestis, D.L., J. Appl. Phys. 52, 6041 (1981).

24. Breshears, W.D. and Bird, P.F., J. Chem. Phys. 58, 5176 (1973).

25. Diesen, R.W., J. Chem. Phys. 41, 3256 (1964).

26. Levy, J.B. and Copeland, B.K.W., J. Phys. Chem. 69, 3700 (1965).

27. Diesen, R.W., J. Phys. Chem. 72, 108 (1968).

28. Chow, W., Stoke, M and Schafer, F.P. Appl. Phys. 13, 1 (1977).

Rates for these reactions have been drawn primarily from the literature referenced. Information for wall reaction rates was drawn from previous work.[29] In the model results to be presented, the wall rates were set to zero. This was justified by assuming relatively nonreactive nickel walls.[29] Homogeneous reactions dominate in the short (60 sec) runs. All long runs will obviously require some level of total contaminant scrubbing which should remove both wall and homogeneous reaction contaminants. During the e-beam irradiation, the model assumes that the electron density is constant and an appropriate value is used to give a 50 percent dissociation of NF_3.

2.6.3 Model Results

The result of the primary section for the case in which NF_3 is the sole species is given in Figure 37. Note that in this case NF is produced by reaction 2 during the e-beam irradiation. Following the e-beam, the radicals recombine and reaction 8 indicates that some NF is converted to N_2 and F_2. Most of the NF_2 produced recombines with F by reaction 5 to reform NF_3 within about 10^{-4} sec. The excess F atoms recombine by reaction 6 to form F_2 within about 10^{-2} sec. The net effect of this set of reactions and initial conditions is that about 4 percent of the NF_3 in the cavity is converted to N_2 during the pulse.

It is obvious that by choosing the proper scrubbing rates and gas makeup composition the initial conditions can be varied to advantage. For instance, if the F_2 concentration is allowed to rise to about half the NF_3 concentration, then the predicted NF_3 consumption rate is reduced to about 2.5 percent per shot because the importance of reactions 7 and 10 is increased compared to that of reaction 8. By using NF_2 makeup instead of NF_3, the net rate of F_2 production is reduced because of reaction 3.

Results of the complete model using the design point system volumes, pulse rate and flow rates are given in Figures 38 through 41. The case of no scrubbing and no gas makeup for a 60 sec run is shown in Figure 38 which

29.   Mandl, A., Slater, R. and Trainor, D.W., "Recycliability Issues in XeF Lasers," Final Technical Report, June 1980, Contract F33615-80-C-2060.

111
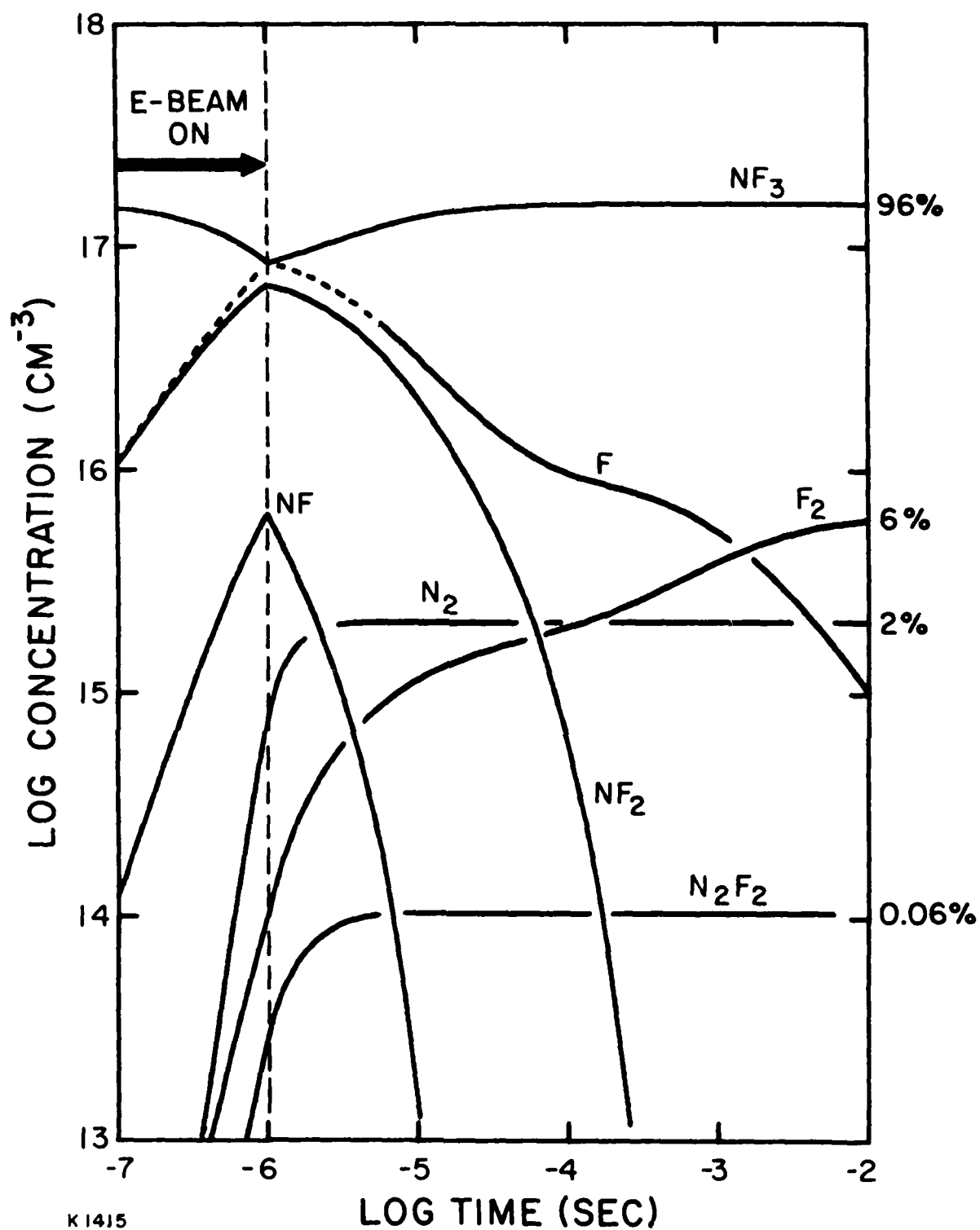
Figure 37.   Single Pulse, Laser Cavity Kinetics

112
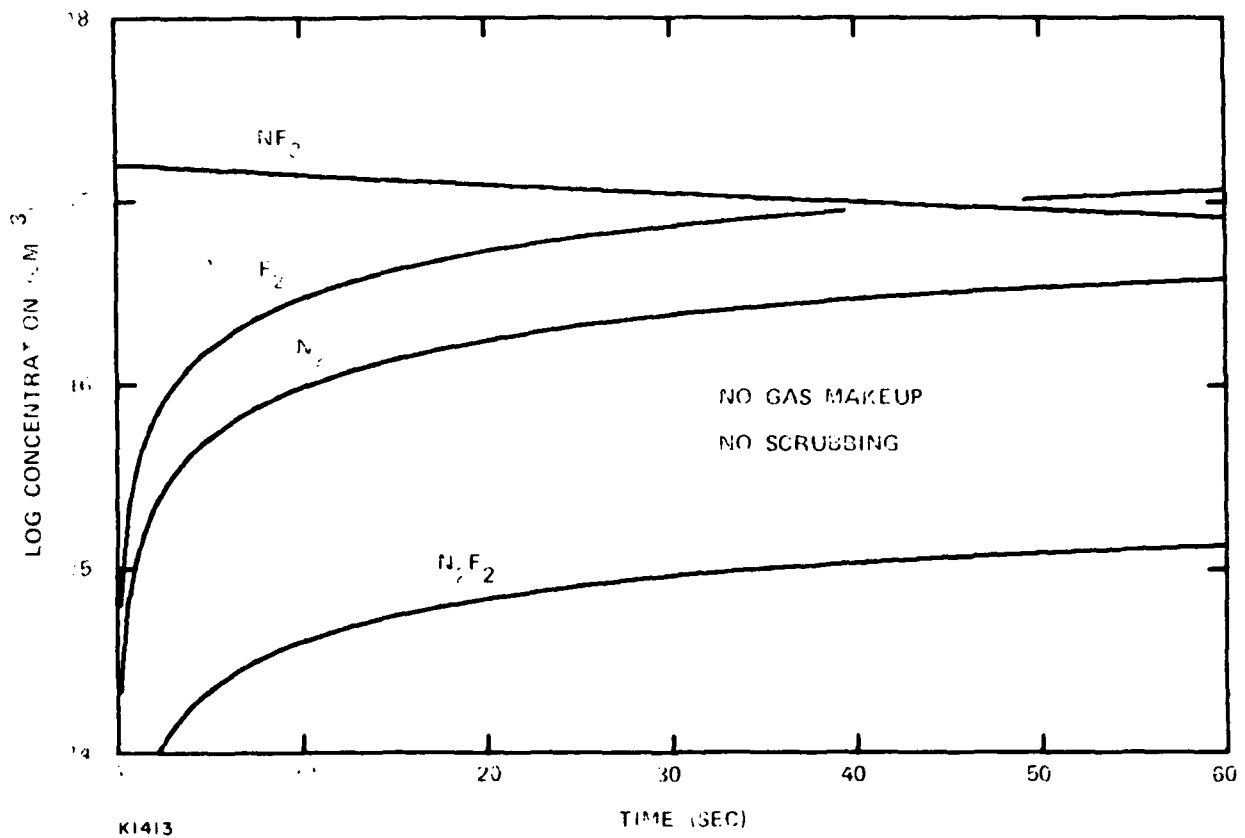
Figure 38.   Model, No Gas Makeup, No Scurbbing

113

RECYCLABILITY MODEL
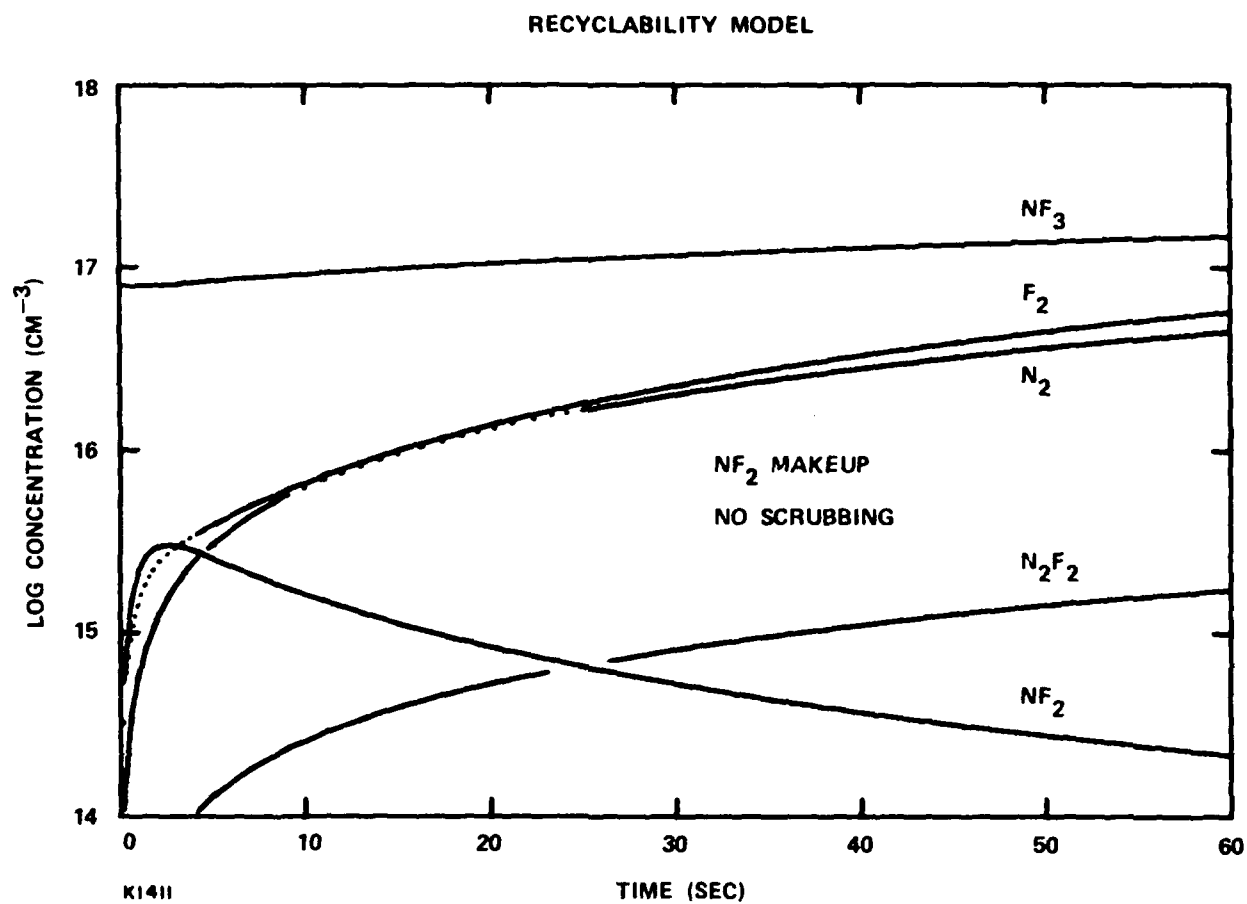
Figure 39.   Model, NF$_2$ Makeup, No Scrubbing

RECYCLABILITY MODEL
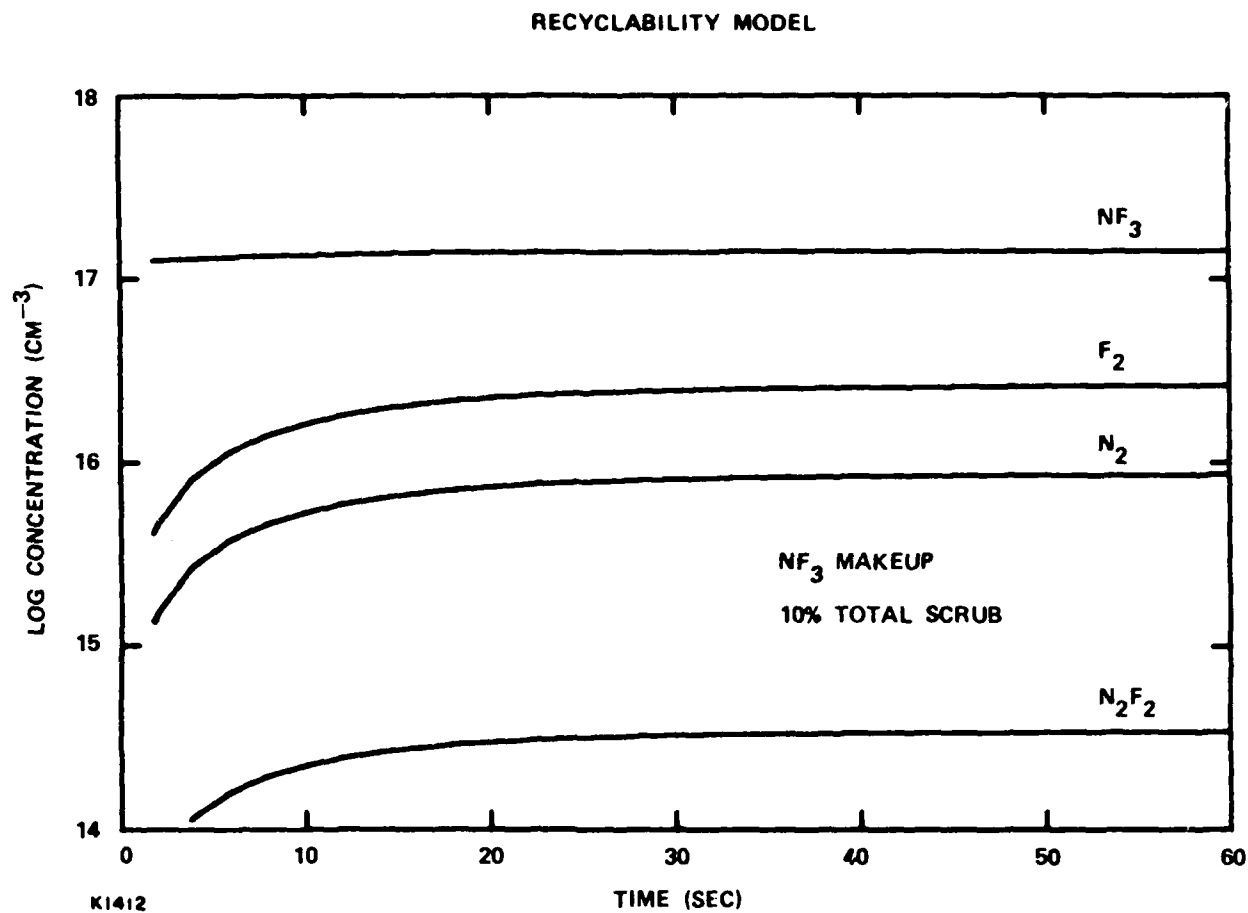
Figure 40.   Model, NF$_3$ Makeup, 10 Percent Total Scrubbing

AVCO EVERETT
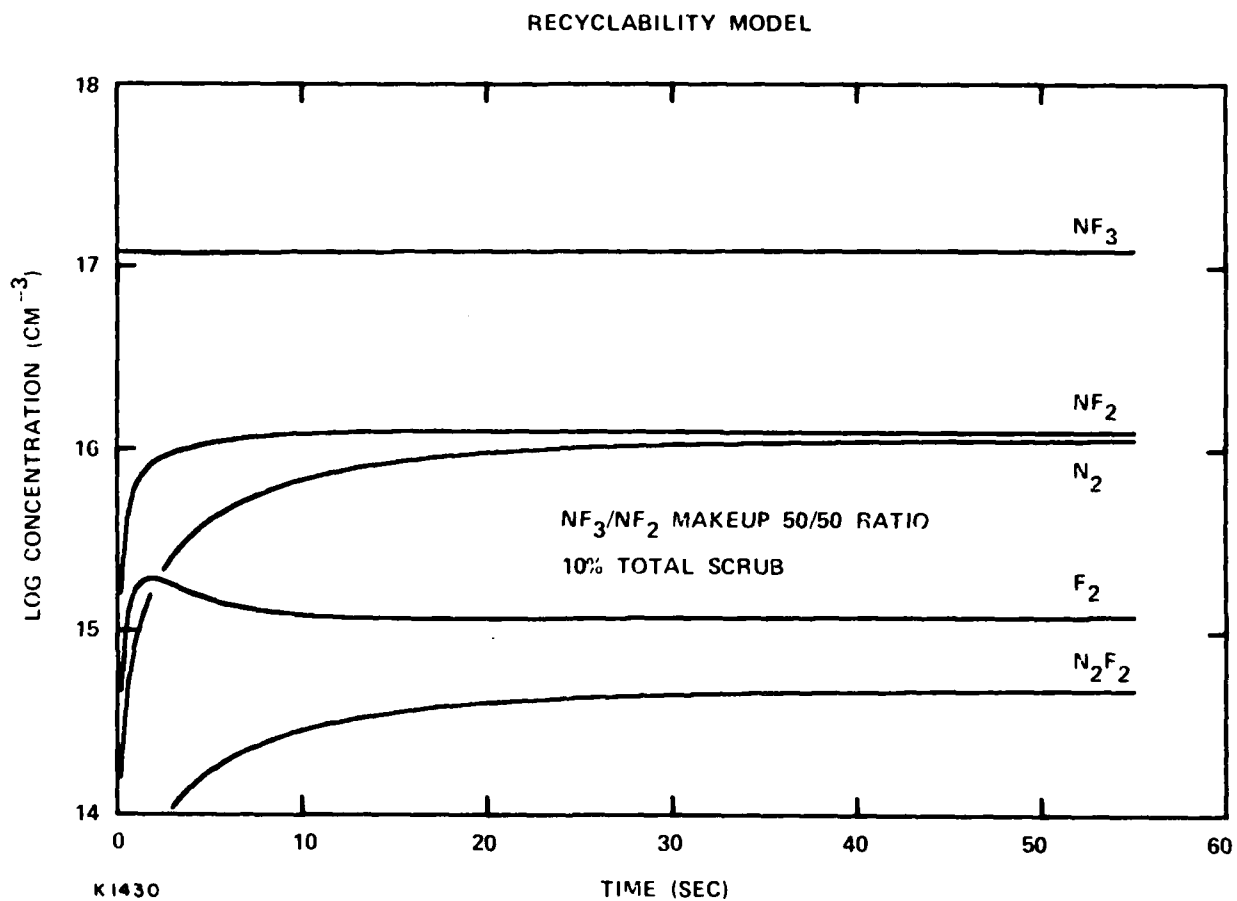
Figure 41.   Model, 50/50 NF_2/NF_3 Makeup, 10 Percent Total Scrubbing

predicts considerable NF_3 loss and excessive F_2 production. It is estimated that F_2 concentration should remain below about 5×10^{16} cm^{-3} to minimize the effect of the 351 nm absorption which has a cross section of about 8×10^{-21} cm^2. Figure 39 shows that NF_2 makeup reduces the concentration of F_2 at the end of 60 sec but must be limited to avoid excessive production of NF_3. Other runs indicate that limited NF_2 makeup combined with a selective scrubbing of F_2 from the gas stream at about a 5 percent diversion of the total flow will keep F_2 at acceptable levels for a 60 sec run. For longer runs, a complete scrubbing of a portion of the gas stream of all constituents other than the rare gases will be required to hold down concentrations of N_2, F_2, N_2F_2 and other contaminants. Figure 40 shows the model prediction assuming NF_2 makeup and a total scrubbing of 10 percent of the total gas flow. Figure 41 shows that a 10 percent total scrub and gas makeup with a 50/50 ratio of NF_2 and NF_3 will hold all contaminants down to acceptable levels in the steady state.

2.6.4 Gas Regeneration Conclusions

The model developed under this program predicts that one minute operation of the laser system should be possible given selective total F_2 scrubbing from about 5 percent of the total gas flow with limited NF_2 makeup. Selective F_2 scrubbing could be achieved with systems employing hot titanium.[29] Steady-state operation should be possible with a total scrub of all gas constituents other than Ne and Xe from 10 percent of the total system flow given proper NF_2/NF_3 gas makeup. Total scrubbing could be accomplished with liquid lithium systems.

2.7 OPTICS DESIGN

This optics design was conducted concurrently with a system integration update as discussed in Section 1.0. Consequently this design applies to a cavity configuration which meets system requirements but is of lower average power than the final baseline design concept. Since the conclusions of this section are not substantially altered by these changes in cavity characteristics, a rework of these design details was not felt to be warranted.

In this section we present the optical analyses and the resulting optical system concepts that will provide the desired 1.3 times diffraction-limited output, both for the laser output itself and the output of the Raman conversion optics. The requirements of most concern for the optical design are the total power and the 60-sec-run time.

The possible configurations and the optical tolerances are described first. The major technical issues are considered to be the dynamic and thermal response of the optics for the repetitively-pulsed 60-sec-run laser.

Solutions to the dynamic and thermal problems are presented. They are simple for the 60-sec run for which thermal equilibrium is not reached; substantially different approaches are needed for the full-power, long-duration system.

There are only a few good options for the optical configuration of the laser resonator. The most promising are shown in Figure 42. The 10 x 15 cm dimensions are determined by the flow and e-beam parameters; the active cavity length of 75 cm then comes directly from the desired 10 kW output. Maximum output is obtained with an output coupling of 65 percent, magnification of 1.67. For this geometry the equivalent Fresnel number of 820 will be well above the critical value of 90 needed for mode separation at this magnification. Thus a simple confocal unstable resonator provides a good solution.

With windows defining the cavity, as shown in the upper illustration, the mirrors are removed from blast effects, simplifying the dynamic problem. H and C represents the hot and cold windows, probably with an evacuated space for best beam quality. Brewster angle windows would not be used because they would significantly increase the optical path length in glass, and thus would increase the optical distortions from heating. Anti-reflection coatings and small tilts will prevent reflections from focusing in the cavity or on optical elements.

118
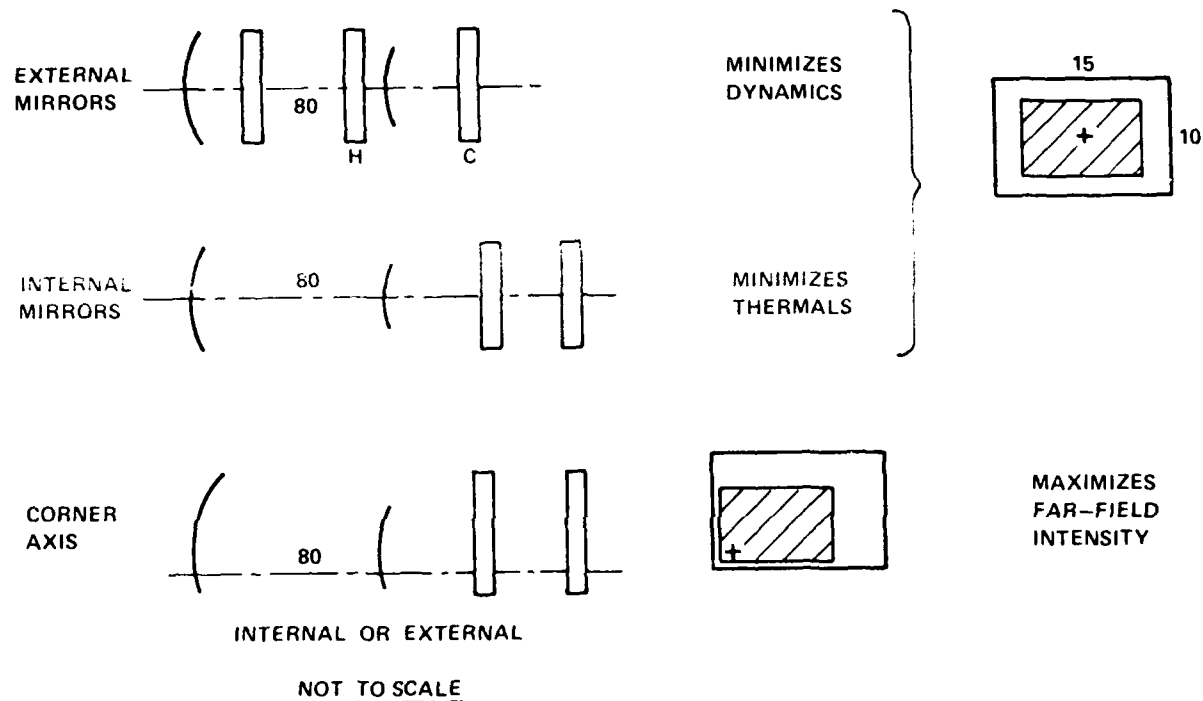
Figure 42.   Configuration Options - Resonator

Windows outside the cavity are exposed to less heating and with mirrors inside there are four fewer window-ray-passes. Thermal effects are then minimized, but bending of the mirrors under repetitive loading is important.

Although an off-axis resonator increases the equivalent Fresnel number and decreases the far-field diffraction, there appears to be no reason to favor it for the breadboard system.

The system configuration shown in Figure 43 will include an injector to decrease the line width of the laser. For the breadboard, the resonator will provide the needed output. For a full-scale system, consideration would be given to an oscillator-amplifier approach that would give an unobscured aperture and minimize window thermal effects.

Conversion to blue-green will be accomplished by two stages, each including a beam-splitter, a reducing telescope, and a hydrogen cell. The reducing telescopes provide the maximum flux, at each wavelength, allowed by the damage threshold of the window material. An expander at the end serves to reduce the flux on following optics.

Uncoated lenses will be used for the conversion in order to allow the maximum flux and minimum length. There are additional possible beams-splitter-telescope approaches that will be given further consideration.

Dimensional tolerances as shown in Figure 44 for the resonator can be taken from equations developed for Cassegrain telescopes. These then represent the single-pass sensitivities. The equations give the allowable axial displacement for a given amount of defocus, and the allowable lateral displacement of the two mirror axes for a given amount of coma.

Care should be used in applying the coma formula as it refers to a displacement of a point called the neutral point, (the focus for a confocal system) with the center of curvature held fixed. It does not refer to the actual displacement of the mirror itself. For the breadboard resonator, however, the mirror f-number is so large (15) that the confocal mirrors are spherical and there will be no coma contribution.

The multipass resonator increases the aberrations by the multiplier as shown, related to the inverse magnification (ϵ), and the order (k) of the aberration. The multiplier is 1.54 for defocus (k = 2). The combined tolerance on spacing is quite tight and will require a carefully designed structure, but is not unreasonable.

120

INJECTOR — RESONATOR — EXPANDER — AMPLIFIER

INJECTED BEAMS

COLD WINDOW

FIRST RAMAN

SECOND RAMAN

EXPANDER

K1452
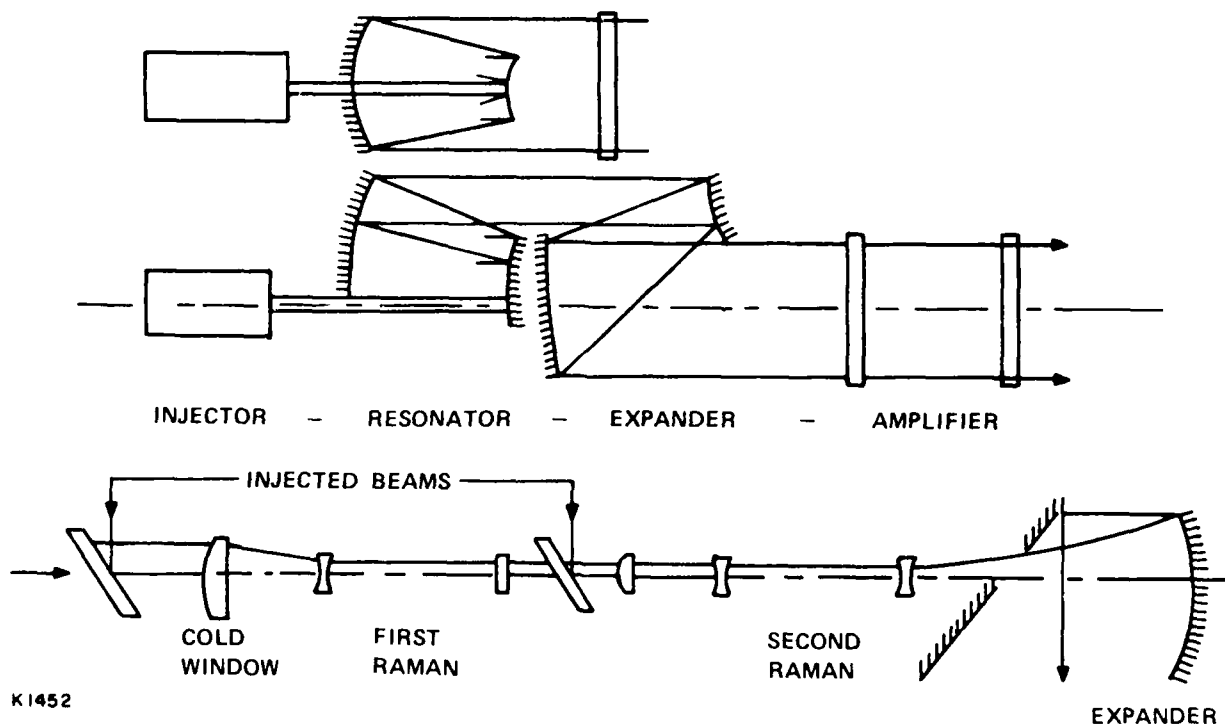
Figure 43.   Configuration Options - Systems

121

SINGLE—PASS

- DEFOCUS $\quad \delta_a = \dfrac{16 \sqrt{3} \, \sigma_w \, F_p^2}{1 - \epsilon^2}$

- COMA $\quad \delta_y = \dfrac{270 \, \sigma_w}{(1 - \epsilon)^3} \cdot \left(\dfrac{d}{D_p}\right)^3$

MULTI—PASS

$$\frac{\sigma}{\sigma \, (1)} = \frac{1}{1 - \epsilon^k}$$

COMBINED
- DEFOCUS $\quad \delta_a = \quad 93 \, \mu m$
- COMA $\quad \delta_y = \quad 4.3 \, mm$

K 1457

σ_w = rms PHASE ERROR = 20 nm

F_p = PRIMARY F—NUMBER = 14.2

$(1 - \epsilon^2)$ = OUTPUT COUPLING = .67

ϵ = 1/M = 2/3

σ_a = ALLOWABLE AXIAL DISPLACEMENT

d = AXIAL SPACING = 1.04 m

D_p = PRIMARY DIAMETER = .15 m

k = ORDER OF ABERRATION

Figure 44. Dimensional Tolerances - Resonator

The pressure loads in each space, as shown in Figure 45 may be different for the cases where the laser is used alone and when it is used with the conversion optics. Both cases are shown in this figure. The laser operates at 5.8 atm and the dynamic over-pressure is 1.6 atm. For beam quality, the space between hot and cold windows would be evacuated. The window thicknesses are based on a safe working stress limit of 7 MPa (1000 psi).

For the conversion system, window thicknesses will be minimized by having all spaces at the same pressure, using helium in the inactive spaces to reduce turbulent wavefront distortions. The thicknesses of the small conversion elements are set at one centimeter as a convenient value for optical figuring. They have no stress limitation. The third large window is relatively thick (2.5 cm) to allow for the rather steeply curved front surface when it is formed into a lens.

Figure 46 shows the calculated dynamic response for the windows and mirrors. For the given pulse frequency (100 Hz) and the expected pulse length and structural or mirror resonant frequencies, there could be some resonant excitations. However, with $f_p \ll f_s$, the worst case dynamic load factor is 4. It is difficult to avoid all resonances because of the complex nature of the mirror and support structure. To be safe, in sizing window thicknesses we have used the factor of 4. However, assuming that the worst resonances are avoided by careful design, a lower factor would be safe.

For the window at each end of the cavity, the deflections can be large and the thickness is set based on maximum stress. For mirrors, the deflections must be held to very small values, requiring that they be very thick. These mirror thicknesses are perfectly reasonable for the breadboard, but they scale approximately linearl, with diameter (shear deformation) and may become unwidely for a large system.

Figure 47 shows the geometry and equations used for an approximate calculation of mirror distortion.

For a 60-sec run the thermal mass of the mirrors is enough to absorb the heat load, and by using low-expansion mirror substrates the deflection can be held to acceptable values. As long as the mirror thickness is greater than the thermal diffusion length for 60-sec (about 10 mm), the surface temperature can be analyzed by the equation for heating of a semi-infinite slab. Using

123

GAS   AIR   LASER   —   AIR

ATM.   1   5.8   0   1

    + 1.65

THICK (cm)   3.5   3.5   1.0

THESE VALUES FOR
LASER ONLY, NO
CONVERSION

THICK (cm)   1.7   1.7   2.5   1.0   1.0   1.0   1.0

ATM.   5.8   5.8   5.8   5.8   5.8   5.8   5.8   1.0

    + 1.65

GAS   He   LASER   He   He H_2 He H_2 AIR

K1451

THESE VALUES FOR LASER
WITH RAMAN CONVERSION CELLS
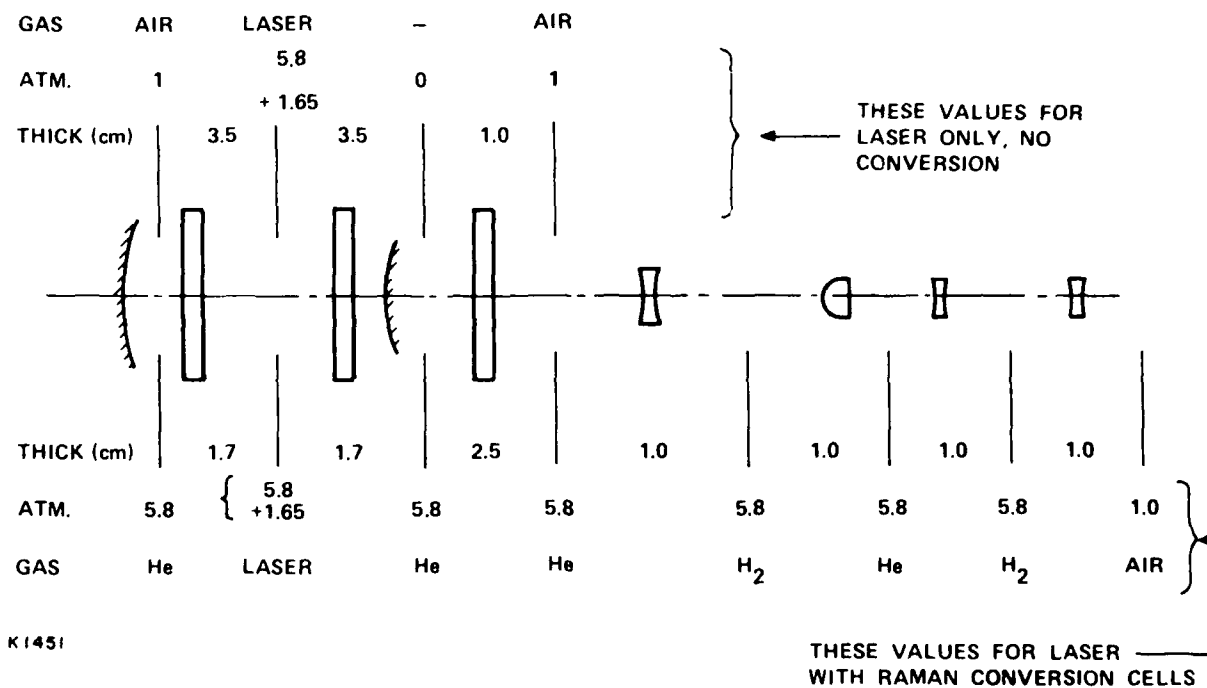
Figure 45.   Pressure Loads - Static and Dynamic

124

f_p (PULSE) $=$ 100 Hz

f_s (STRUCTURE) $\geq$ 1000 Hz

τ (PULSE LENGTH) $=$ 0.2 ms

RESONANT GAIN $\leq$ 4X

$$\frac{\Delta \text{ (DYNAMIC)}}{\Delta \text{ (STATIC)}} \leq 4$$

		THICKNESS	MAXIMUM DYNAMIC DEFLECTION
WINDOW		3.5 cm	$\pm$ 5 μm
		1.0 cm	$\pm$ 40 μm
MIRROR —	LARGE	20 cm	$\pm$ 50 nm
	SMALL	14 cm	$\pm$ 50 nm

K 1460

Figure 46.   Dynamic Response

125
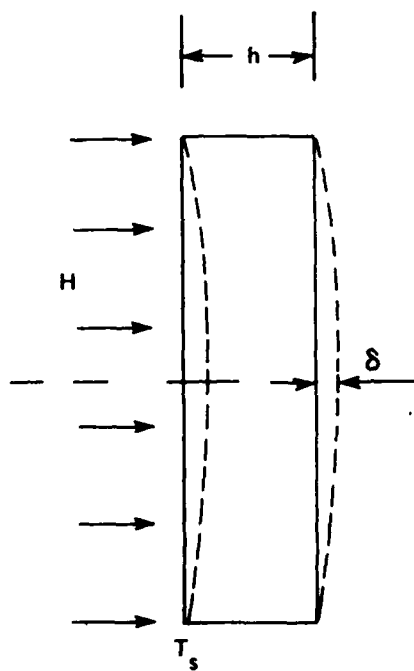
for $h > 10$ mm

$$T_s = \frac{2H\beta_s \sqrt{t}}{\sqrt{\pi C \rho k}}$$

$\beta_s = .005$

$$T_s = 36 \ K$$

$$\delta \leq \frac{\alpha D_s^2 T_s}{8h}$$

$\alpha = 3 \times 10^{-8} \ k^{-1}$

$$\delta \leq 233 \ nm, \ DEFOCUS$$

- **LOW EXPANSION, UNCOOLED MIRROR IS ADEQUATE**

K1459

Figure 47.   Thermal Effects - Mirrors

the properties for ultralow-expansion fused silica from Corning (ULE) gives a temperature rise of 36°. The mirror bending will be less than that for a uniform gradient with the same T_s, and therefore will be < 230 nm. Thus there will be some focus change that must be compensated during the run. There will be little, if any, beam quality degradation, however, since the deformation will be almost entirely spherical.

The thermal effects on the windows are analyzed first by considering the properties of possible window materials, then analyzing the heat loads, and then calculating the temperature gradient and the resulting optical path differences. Figure 48 shows important properties for a few likely materials.

Fused silica is a useful material because it is available in pure form and in large sizes. It has relatively low absorption at 350 nm, and a very low coefficient of expansion. Unfortunately, it has a relatively high change of index with temperature so that the coefficient, z, which combines these factors is not particularly low. It also has a rather low conductivity, so that gradients in the window will tend to be large.

Calcium fluoride has a low absorbtion, and a negative dn/dt that just cancels the effect of thermal expansion. It is available in diameters to about 20 cm, just adequate for the breadboard device. Gradients through the piece would cause severe bending, but this should not be a problem for our application where the absorbtion is uniform throughout the piece.

Saphire has a rather high absorbtion at 350 nm, making is useful only where its high conductivity is a requirement.

As shown in Figure 49, the most complex thermal loads occur for the windows within the laser cavity. The window terminology and heat loads are defined in this figure. Given F as the output flux (W/cm^2) then the exit window is exposed to that flux over the outer, rectangular, annulus, and twice that flux in the center. The flux at the primary window is reduced by the one-way gain (approximately equal to M) but it is doubled by the two passes. The cold window sees the same flux as the annulus of the exit window, and this is increased in proportion to the reduced beam area at the Raman optics. These differing but uniform flux loads were applied to a thermal model of each window to obtain the two-dimensional temperature distributions as a function of time. Since the response with time was quite linear, only the results for the end of 60 sec are presented here.

MATERIAL	α	$C\rho$	k	dn/dt	β	z
Si O_2	.41	1.7	1.4	+ 14	0.1	.84
Mg F_2	13.7	3.14	12	+ 2	0.1	.24
Ca F_2	24	2.71	10	−9.5	0.05	+ .02
$Al_2 O_3$	5.6	3.0	24	+ 17	0.6	4.3

CONSTANT	UNITS	
α	10^{-6} k^{-1}	COEFFICIENT OF EXPANSION
$C\rho$	10^{-6} $J m^{-3} k^{-1}$	VOLUME HEAT CAPACITY
k	$W m^{-1} k^{-1}$	CONDUCTIVITY
dn/dt	10^{-6} k^{-1}	INDEX CHANGE
β	m^{-1}	VOLUME ABSORBTION
z	$10^{-12} k^{-1}$	$\beta [(n-1) \alpha + dn/dt] / C\rho$

K1456

Figure 48.   Thermal Effects - Windows - Materials

PRIMARY
WINDOW

EXIT
WINDOW

COLD
WINDOW

RAMAN
WINDOW

$\frac{4}{5}$ F

2F

F

14F
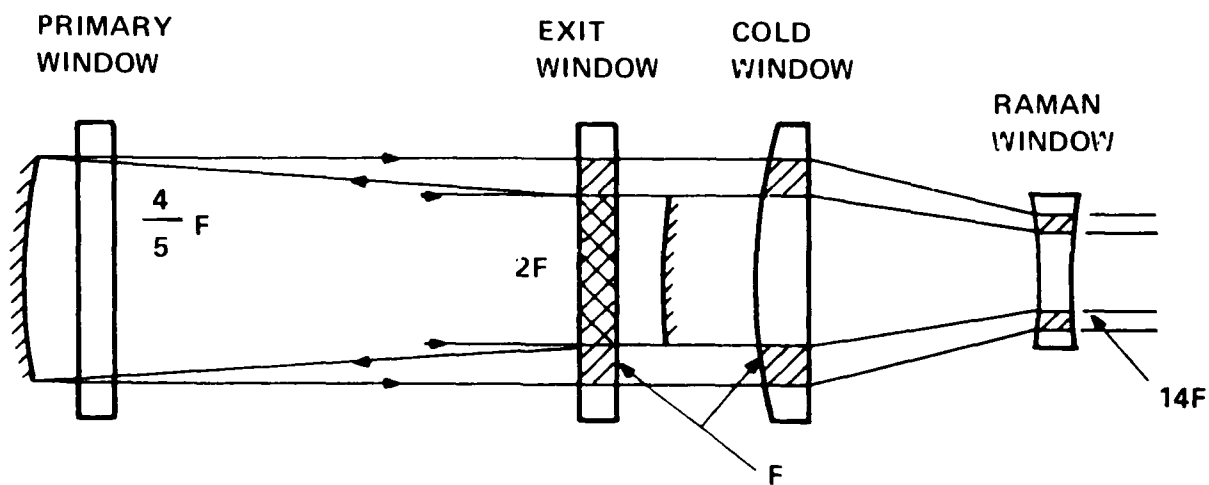
F = OUTPUT FLUX, W/m^2

$\sqrt{G}$ = ONE—WAY GAIN = 1.67 = M

K1458

Figure 49.   Thermal Effects - Windows - Loads

The analysis was done for both fused silica and calcium fluoride windows.

The results for fused silica windows are shown in Figure 50. Temperatures are shown for the long axis of the rectangular aperture. The gradients are plotted separately for the central aperture and the annulus since the wavefront errors add. For comparison, the gradients for a CaF_2 Raman window are also shown.

The table shows for each window, the number of ray passes and the total optical path difference (QPD) between rays traversing the coldest and warmest parts of the aperture. Data are given in nm.

The exit window (center and annulus) and the primary window have the greatest OPD at the outer edge, so the OPD values are added linearly. Since the cold window has a different distribution we have added that to the other effect by taking the root-sum-squares (rss) instead of combining the detailed distributions. The result is an estimated peak to peak variation of 2900 nm, which, based on a typical 5:1 ratio, would give an rms value of about 600 nm. To bring this to a reasonable value of about 30 nm would require the use of adaptive optics correction to reach a residual level of about 5 percent. That is an achievable value, but would result in a rather complex system.

The table shows that a single Raman window introduces 1100 nm of OPD. For three elements (one stage) this would give about the same OPD as for the laser and would require the same level of correction.

If calcium fluoride is used, the thermal distortions are very small, as shown in Figure 51, even after 60 sec. The temperature gradients are very small and optical distortions are almost negligable. It is the best material for the breadboard laser.

Whether it can be used for the Raman hydrogen cell will depend on its laser damage threshold. If it is not as high as that for fused silica, compromises must be made between distortions in the window and increased distortions in a longer cell. Since window distortions can be compensated by corrective optics, it will be better to use the material with the higher damage threshold.

WINDOW	# PASSES	TOTAL OPD
PRIMARY	2	900 nm
EXIT		
CENTER	2	1030
ANNULUS	1	920
COLD	1	690
RAMAN	1	1120
LASER p–p	p–p	2900 nm
	RMS	600 (1.7λ)

NEEDS CORRECTION
TO 5%
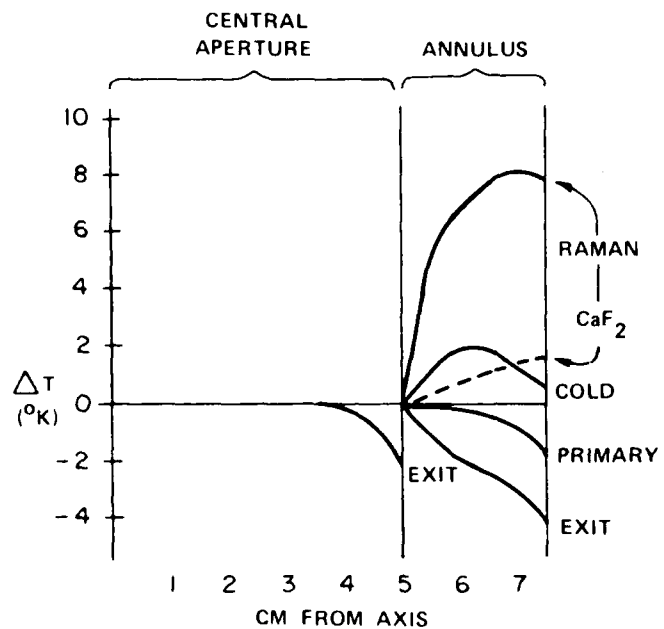
ALL SiO$_2$ EXCEPT AS NOTED

K1463

Figure 50.   Thermal Effects - Fused Silica Windows - OPD

131
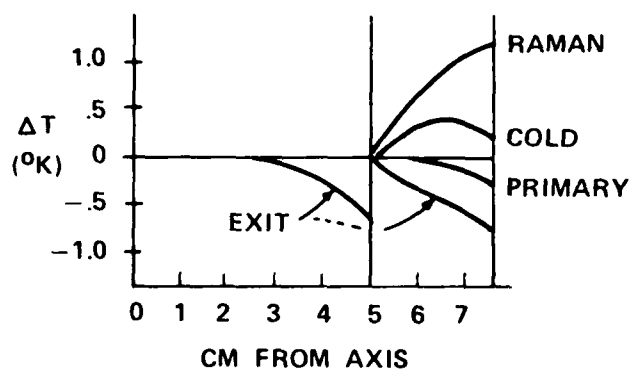
WINDOW	PASSES	TOTAL OPO, nm
PRIMARY	2	7
EXIT		
CENTER	2	24
ANNULUS	1	15
COLD	1	8
RAMAN	4	40

	LASER	RAMAN
p–p	47	40
rms	10	8

K5026

Figure 51.   Thermal Effects - Windows - CaF$_2$

From the preceding analysis it follows that the simplest laser config-
uration includes a calcium fluoride windows, with the mirrors external to the
cavity. This is shown in Figure 52. A third window provides the hot-cold
interface. For use with the Raman conversion optics, the cold window will
also be the first lens of the beam-reducing telescope.

One stage of the conversion optics includes a beam splitter, an injected
beam, a reducing telescope and a hydrogen cell. The negative lens will form
the first window on the cell. Two such stages plus a final expander section,
as shown in the system concepts illustration, will form the conversion optics.

The phase front error budget shown in Figure 53 provides an estimate of
system performance. Wavefront errors are given for the laser alone and for
one conversion stage. For the latter, it is assumed that the wavefront qual-
ity of the pump beam is not important, so only the last conversion stage needs
to be considered.

It must be noted that all these numbers are extremely small. The values
have to be considered only as estimates, and they should be used to help de-
fine the most critical areas.

The gas inhomogeneity numbers are taken from the flow analyses. Window
heating distortions are based on the use of calcium fluoride windows; these
values and that for mirror distortions are taken from the preceeding
illustrations.

The figuring errors are based on values of 1/60 wave rms (visible) for
the mirror surface and 1/40 wave rms for the windows in transmittance. These
values can be achieved for large optical elements, and it is reasonable that
somewhat lower values could be reached at the 20 cm diameter needed here.
However, these numbers must include the effects of mounting and strains intro-
duced in the mirror-mount interface as the system temperature is raised to
150°C. These figuring errors are the dominant part of the error budget - an
encouraging situation because they can, if necessary, be reduced, if suffi-
cient time is available.

The Strehl ratio is calculated by the approximation $Sr = \exp [-(2 \pi\sigma/\lambda)^2]$
where σ is the rms wavefront error and λ is the wavelength. The number of
times-diffraction-limit is here defined as $1/\sqrt{SR}$.

133

HOT WINDOWS

COLD WINDOW/LENS

OUTPUT COUPLING 65%
CaF_2 WINDOWS

LASER

CONVERGING
LENS

1 STAGE
OF RAMAN
CELL

H_2

COLLIMATING
LENS

BEAMSPLITTER
FOR INJECTOR
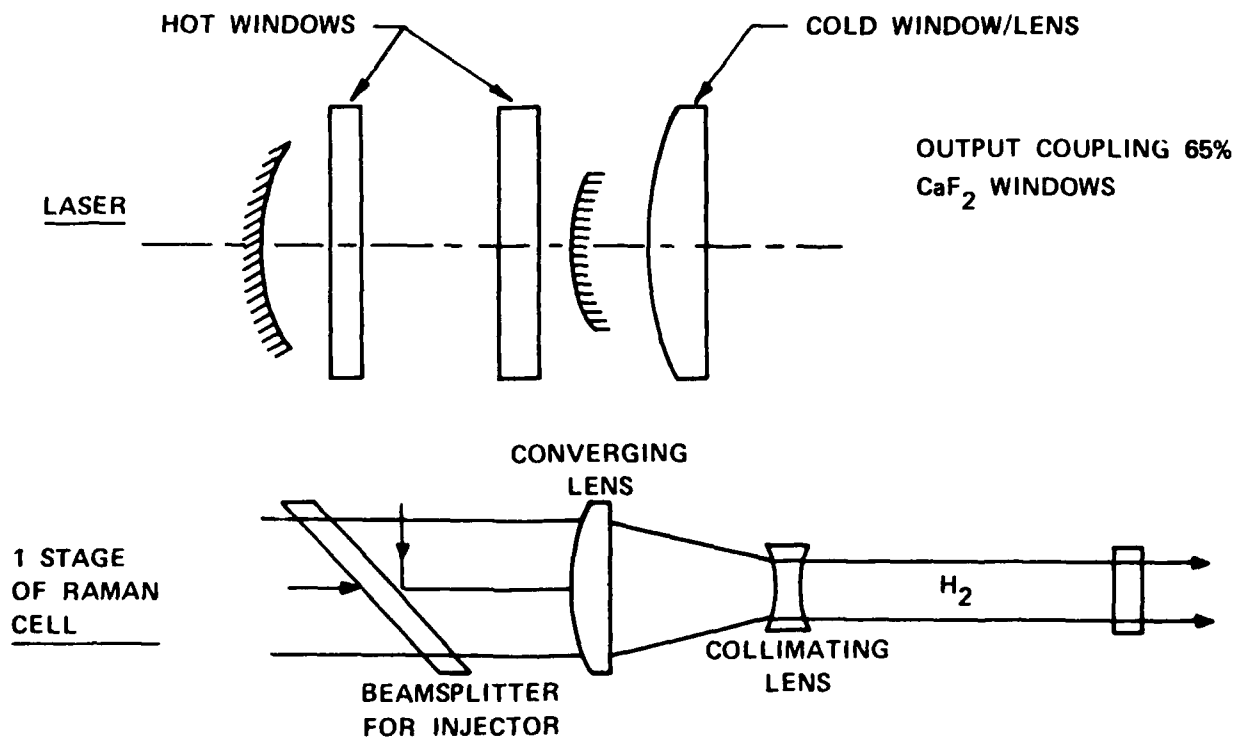
K1450

Figure 52.   Selected Optical System Concept

	LASER	1-STAGE RAMAN	NOTES
LASER GAS, 6 ATM	20	30	
WINDOW HEATING	10	10	WITH CaF$_2$
MIRROR HEATING	7	–	
*FIGURING, MIRRORS	28	–	10 nm PER SURFACE
*FIGURING, WINDOWS	26	30	15 nm IN TRANSMITTANCE
BEAM–SPLITTER REFL	–	20	10 nm SURFACE
MISALIGNMENT	10	10	
RSS	46	49	*INCLUDES MOUNTING
STREHL RATIO	.50	.68	
XDL	1.4	1.21	

K1461

Figure 53.   Phase Front Error Budget (nm rms)

These error budget numbers are reasonable, but so small that there is little possibility of directly measuring most of the contributions with any accuracy. To provide a margin for error, the breadboard system might include low-frequency active correction. Low frequency means there would be no attempt to correct pulse-to-pulse variations; but initial errors and changes developing over periods of several seconds would be compensated. With this inclusion, there is high confidence of reaching an rms wavefront quality on the order of 40 nm.

2.8 E-GUN AND MAGNETIC FIELD

2.8.1 Introduction

The e-gun assembly for the baseline design consists of several components which are compatible with both field emitting (carbon felt) and thermionic (barium dispenser) cathodes. The principal components are:

The Vacuum Chamber - is constructed of stainless steel with metallic seals and an oil-free pumping system (turbo and/or cryo) designed to maintain a base pressure of $\sim 10^{-8}$ torr. Outgassing rates will be reduced by a combination of e-beam cleaning, chemical cleaning, and a moderate bake-out of $\leq 300°C$. The pumping system is sized to handle the outgassing load caused by electron desorption during emission for the desorption rates and maximum operating pressures of both hot and cold cathodes.

The High-Voltage Bushing - is made of ceramic rings brazed to metal rings which are electrically graded for pulsed operation and is commercially available. The ceramic-metal construction allows a high-temperature bake-out and permits operation of the thermionic cathodes with no bushing cooling necessary. Electrical and cooling connections are passed through a coaxial tube within the bushing with high pressure SF_6 providing high voltage isolation between the coaxial structures.

The Cathode Structure - consists of a smoothly faired surface (for minimum electrical stress) at the end of the high-voltage bushing. In the baseline design, the carbon felt cathode material is directly mounted on this surface with a mechanical clamping arrangement avoiding the use of organic adhesives. At a later time, this surface can be replaced with a hollow box of similar profile inside of which is contained an array of dispenser cathode modules, heater structure, cooling tubes and electrical connections for grid pulse control.

The Anode Structure - provides a ground plane for the e-beam and will have low stress concentration and high electron transmission. A field-free-drift region between the anode plane and the foil support structure is provided to allow for the space occupied by the acoustic suppression apparatus. Grounded parallel planes are provided in the drift space to short out any space charge induced electric fields. All structures which are intercepted by the beam will be actively cooled. The foil support structure is described in detail in Section 2.3.

137

The Magnetic Field Coil - pair generates an axial guide field of sufficient strength to ensure uniform energy deposition within the laser gas and confine the gain volume without the use of material shields. With thermionic cathodes, the magnetic field can increase e-beam efficiency by providing guided electron trajectory for operating in a non-intercepting mode. The coil is powered by a standard dc supply and is water-cooled for continuous operation.

2.8.2 Cathode Design

2.8.2.1 Baseline Selection

Carbon-felt cathodes are chosen for the baseline design because of their simplicity and low technical risk. These cathodes have been used on several laser device at AERL and provide reasonably uniform emission over large areas for pulse lengths up to ~ 1 μs and for beam energies and current densities both in excess of 300 kV and 12 A/cm^2, respectively. Carbon-felt cathodes operate via field emission with each of the many fine carbon fibers serving as a separate emission site. Hence, no heaters are required and the gun structure is not subject to radiant heat loads thereby simplifying their design. The high-voltage bushing is also simplified since no filament current leads or coolant tubes need pass through. Carbon-felt cathodes have been repped as high as 50 Hz[30] although outgassing effects limit their use to ~ 1 min duration bursts. For longer duration runs, however, thermionic cathodes appear to be the most viable solution..

2.8.2.2 Diode Closure

The baseline design for the carbon-felt is strongly influenced by diode closure which limits the useful pulse length. During the field emission process, the fine carbon fibers vaporize giving rise to local plasma emission sites. Electrons from the plasma are drawn to the anode dragging the plasma by a process similar to ambipolar diffusion. As the plasma "closes" towards the anode, the effective anode-cathode distances decreases causing an increase in current and/or decrease in diode impedance. If the pulse duration is sufficiently long, arcing can occur. For shorter pulse durations, the PFN imposes a design constraint in terms of a maximum allowable rise in current or a maximum impedance level variation.

30.   Shannon, J., Maxwell Labs., Inc., private communication.

AVCO EVERETT

For uniform emission, the cathode is operated in the space charge limited regime and the gun current and impedance vary according to the Child-Langmuir Law. The anode-cathode separation varies with time due to diode closure which is assumed constant during the pulse in agreement with AERL data as shown in Figure 54. This data shows a voltage and current trace and the predicted value of current assuming a constant diode closure velocity with applied magnetic field. A summary of the data is shown in Figure 55 for various cathode profiles. For the baseline design with B = 2 kG, a closure velocity of 1.8 cm/μs is observed. Using this value of closure velocity, the baseline design summarized below is derived.

E-GUN BASELINE DESIGN
(Carbon Felt Cathode)

Parameter	Value
Accelerating Voltage	275 kV
Time Average Current	14.5 kA
Pulse Duration	1 μs
Cathode Dimensions	12 x 130 cm
Anode-Cathode Spacing	7.0 cm
Diode Impedance Variation	1.96

2.8.2.3 Mechanical Attachment

The method of attaching the carbon-felt to the properly contoured high-voltage terminal has been with a conductive epoxy. This convenient adhesive allows for complex contours and easy spot repairs should a small area become damaged. For single pulse operation, this method is adequate. For repped operation, however, outgassing of the epoxy may limit its usefulness. An alternate method tested at AERL is to stretch the felt material over contoured surface in tension. This method will be used in the baseline design. Without conducting epoxy, it is possible that the felt is heated even in short duration bursts and large outgassing may occur either from gas absorbed on the

$$J = C \frac{V^{3/2}}{(d - V_c t)^2}$$

$$V_c = 1 \, cm/\mu s$$
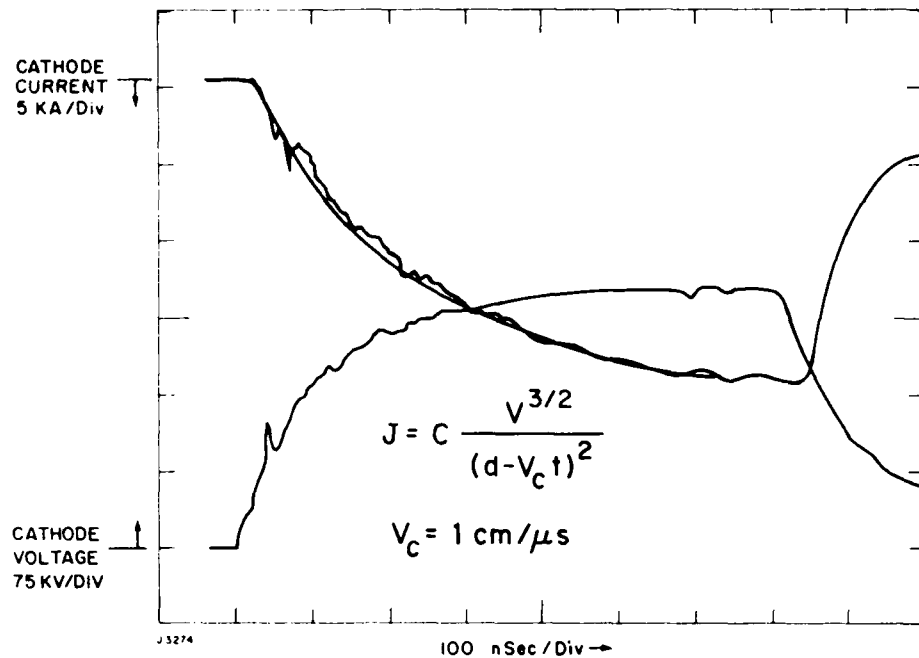
Figure 54. Volt-Ampere Characteristics for a Space Charge Limited, Carbon Felt Cathode with Diode Closure
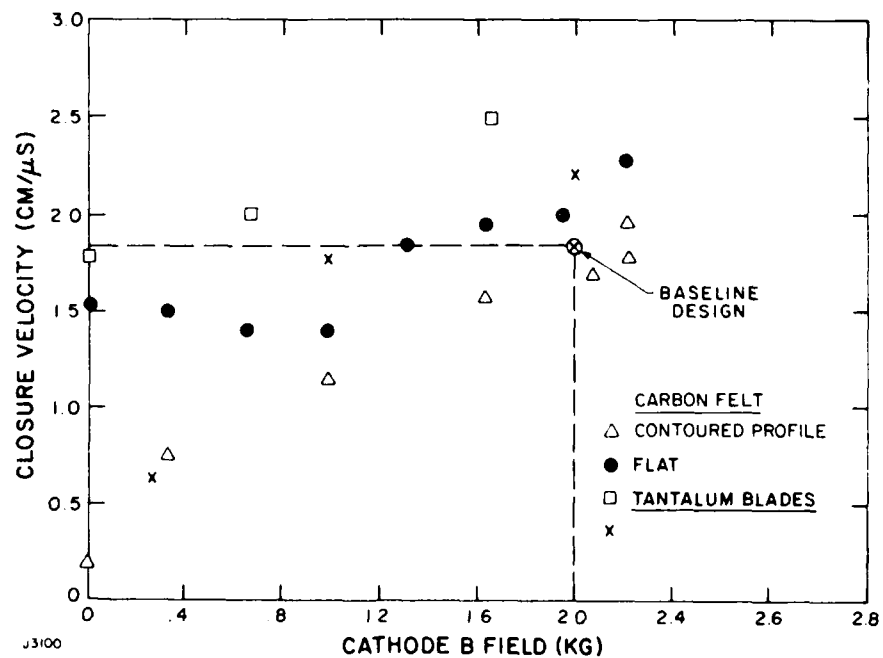
Figure 55. Diode Closure Velocity vs. Applied Magnetic Field

140

long, slender fibers or from organic binders present. Experiments at AERL have shown that carbon felt retains its structural integrity even after prolonged heating at 1000°C in vacuum. Therefore, the felt material can be outgassed in vacuum prior to installation or after installation as part of a bake-out procedure.

2.8.2.4 Ignition Conditions

The field emission requires a minimum value of dE/dt where E is the applied electric field. For the baseline design with a 1 μs pulse and 10 percent risetime, the electric field turn-on is at a rate of $\sim 4 \times 10^{11}$ kV/cm/s which has been shown to be adequate for field emission ignition. The use of a grid structure for pulse steepening would cause arcing due to diode closure and grid mask structure placed on the cathode would decrease field strength below the ignition point. Hence, operating in the non-intercepting mode for carbon-felt cathodes is not readily feasible.

The loss of ignition is probably the major cause of the limited lifetime of carbon felt cathodes. The felt cathodes rely on the field emission from numerous sharp points for uniform emission. As electrons are drawn from the density of sharp points decreases. A possible compensation for this effect is a reduction in pulse risetime and/or a rise in voltage but eventually, spatial uniformity caused by lack of ignition limits useful life. Lifetimes of $\sim$ 3000 pulses have been demonstrated,[30] and an extension of this by a factor of $\sim$ 2 to meet the present device requirements appears feasible without a major development effort.

2.8.2.5 Emission Uniformity

The emission from carbon felt cathodes can be made uniform with proper electrode shaping. An example of the emission profile from a large area felt cathode in a magnetic field is shown in Figure 56. These electrode shapes are used in the baseline design.

2.8.2.6 Thermionic Cathode Alternative

The demonstrated performance of carbon-felt cathodes is judged sufficient to meet the requirements of the integrator device, however, the overall properties of this cathode cannot be projected to meet future needs. Thus,

141
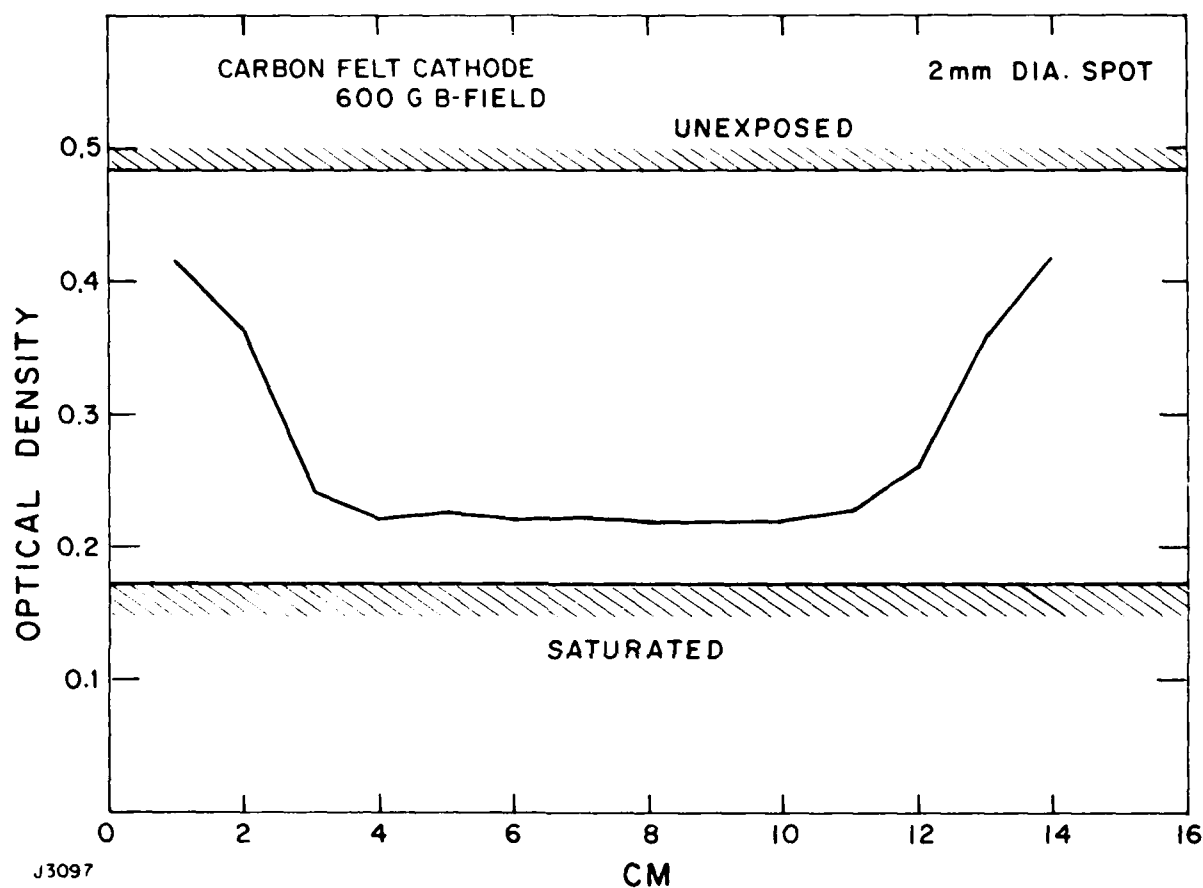
Figure 56.   Emission Profile of a Carbon Felt Cathode

for longer run durations and extended pulse lengths we have concluded that thermionic dispenser cathodes is the most viable alternative both in terms of demonstrated and projected performance.

The present e-gun is designed to be compatible with thermionic cathode installation and operation. The important features of dispenser cathodes which have been demonstrated in AERL technology programs include emission density of 30 A/cm^2, lifetime in excess of 100 hr and 5×10^7 pulses, flat current wave shapes for pulse durations of 5 μs and scalability to 1-m long arrays.[31-33]

The added complexity of thermionic cathodes compared to cold cathodes includes primarily the need for heater power and the more stringent vacuum requirements with the associated susceptibility of the cathode to poisoning. Recovery of cathode emission after exposure to laser gas has been demonstrated, however.

2.8.3 Vacuum Chamber and Pumping System

2.8.3.1 Vacuum Chamber Design

The vacuum chamber for the e-gun will consist of a stainless steel box which has openings for the foil support structure, the high-voltage bushing and ports for vacuum pumps, gauges, etc. The chamber will be designed to withstand the buckling forces that arise from the external pressure on the walls of the chamber. Inside surfaces of the vacuum chamber will be ground and polished to a smooth finish in order to minimize both electrical stress and the potential for outgassing. Final finishing will be done by a Diversey dip process which removes a small amount of the surface and produces a finish similar to electro-polishing. Continuous inside welds will be used to avoid trapped volumes. Metal seals will be used throughout the system so that the system can be baked under vacuum. Conflats and gold wire crush will be utilized. The foil will be welded to the foil support structure using standard e-beam welding techniques.[34]

31. Eninger, J.E., Friedman, H.W. and Williams, K.E., E-Gun Technology Final Technical Report Contract DAAK-40-78-C-0217, July 1981.

32. Avco IRAD, E-Gun Technology, Project 81008316, 1981.

33. Avco IRAD, Guide Magnetic Field, Project 81008316, 1981.

AVCO EVERETT

2.8.3.2 Pumping System Requirements

When an e-gun is placed in operation, gas can be released from surfaces as a result of electron and ion induced gas desorption and as thermal outgassing. The pumping system must have sufficient speed to remove the gas and to maintain the pressure in the chamber at a acceptable level. The pumping speed that is required is proportional to the product of electron desorption coefficient and average e-beam current and inversely proportional to the maximum allowable pressure.

Carbon felt cathodes can be operated at pressures up to ~ 10^{-4} torr (arcing limit). Also, experiments have shown[30] that ~ 3 molecules are released per electron when carbon felt cathodes are used in a repped mode. It is not clear what portion of this gas load is caused by electron and ion induced gas desorption and what part is due to thermal outgassing of the cathode material. In the baseline design the cathode support plate will be actively cooled, the carbon-felt will be prebaked in vacuum, and the felt will be held mechanically without the use of organic adhesives, in order to avoid excessive outgassing. Thus, conservatively assuming a value of 3 for η and a maximum operating pressure of 10^{-4} torr for carbon felt cathodes, a pumping speed of 10^4 liters/s is needed for the baseline design. The e-gun vacuum chamber will be evacuated with a turbo and/or cryopump to prevent contamination of the system with pump oil. A single 20 in. cryopump available from CTI-Cryogenics has sufficient pumping speed.

Dispenser cathodes require a base pressure < 10^{-7} torr for good activation.[32] The operating pressure, however, can be much higher without degrading cathode performance. Avco experiments have shown that a cathode emission current of 12 A/cm^2 can be achieved at an operating pressure of 3×10^{-6} torr, provided that the surfaces which electrons strike are clad with copper. The vacuum chamber and e-gun will undergo a multistep cleaning process to ensure a desorption coefficient η < 0.1 molecule/electron. Thus, assuming a value of 0.1 for η and a maximum operating pressure of 3×10^{-6} torr for dispenser cathodes, a pumping speed of 10^4 liter/s will then be sufficient for dispenser cathodes as well.

---

34. Metals Handbook, 18th Ed., Vol. 6, p. 537, Am. Soc. Metals, Metal Pk., Ohio, Diffusion Bonding Welding in titanium is also an acceptable technique.

2.8.4 Electrode Structures

2.8.4.1 High-Voltage Design

The performance and reliability of high-voltage devices are generally limited by the electrical breakdown strength of the various media involved: vacuum, gas, dielectric surfaces and bulk materials. In addition to the type of medium, the achievable stress levels depend on factors such as geometry and cleanness of electrode surfaces, associated stress concentration, and time dependence of the applied voltage. AERL's experience in this area includes e-beams where the high voltage is applied dc to guns which are grid switched, as well as to externally switched diodes.

An example of an externally pulsed system is the DARPA-Avco E-gun Test Facility, where we have demonstrated dispenser cathode operation at 300 kV for 1 μs pulse duration with 3 cm diode spacings. In this case it was found essential to maintain high current-flow conditions to avoid breakdown in the diode at the average field of 100 kV/cm.[31]

The experience of other workers include investigation especially aimed at studying breakdown under more or less ideal conditions,[35,36] as well as for design purposes perhaps more useful experience of designers of commercial high-voltage microwave tubes. Staprans[37] has reported on electron tubes in the 25-300 kV range for microsecond pulses. He derives an empirical scaling law for the tube holdoff voltage: $V_{max} = 6 \times 10^6 \times L^{0.8}$ where L is the anode - cathode spacing. For a 300 kV design this leads to L = 2.4 cm and a breakdown field of 125 kV/cm. It should be noted that these tubes generally are baked and outgassed according to standard commercial procedures. To achieve high reliability it is necessary to derate the design from the max holdoff voltages. Long term reliability may require a derating factor of about 2. This leads to design fields of 60 kV/cm for pulsed operation.

---

35. Trump, J.G. and Van deGraaff, R.G., "The Insulation of High Voltages in Vacuum," J. Appl. Phys. 18 327-332 (1947).

36. Shannon, J.P., Philip, S.F., Trump, J.G., "Insulation of High Voltage Across Solid Insulators in Vacuum," Proc. Int. Symp. on Insulation of High Voltages in Vacuum, MIT, Oct. 1964, pp. 281-303.

2.8.4.2 Electron Trajectories

In order to assess the overall electron transmission properties of the foil support grid structure one must analyze the orbit of the electrons in the diode field free drift region and support grid structure. Because the foil support bars are relatively deep (0.75 cm) compared with their separation, (0.3 cm) finite Larmor radius in the foil support structure will cause some beam electrons to impinge on the side of the support bars and be degraded in energy. To analyze this effect we must estimate the electron Larmor radius at the entrance to support structure.

A finite Larmor radius in the e-gun arise chiefly from two sources. Near the cathode the applied accelerating e-field and magnetic guide field is co-linear. However, the emitted current generates a self-magnetic field which is perpendicular to the applied e-field. This field creates a electron velocity component that is perpendicular to the resultant magnetic field and therefore imparts a Larmor radius to the electron orbits. For an e-beam which is long compared to its height the self-field is approximately one-dimensional and therefore proportional to the product of current density and distance from the e-beam centerline. The maximum Larmor radius for the baseline design where the beam energy is 275 kV and the beam height is 12 cm, is 1.1×10^{-2} cm. The maximum Larmor radius is then which is much smaller than the hibachi bar spacing and is therefore negligible.

The second contribution to the electron Larmor radius arises from the curvature in the magnetic field. In the region of the foil support grid structure, the self magnetic field of the e-beam (which only exist during the ~ 1 μs when the beam current is switched on) does not appreciably diffuse into the conducting foil support structure and therefore is excluded. The magnetic field inside the support structure must therefore remain the same as the externally applied magnetic field which is parallel to the sides of the support bars. The resultant magnetic field curvature will lead to an increase in the electron Larmor radius. If the change in magnetic field occurs in a distance larger than or comparable to the distance it takes for the electrons to complete one Larmor orbit, then the change can be considered adiabatic and the

37. Staprans, A., "Voltage Breakdown Limitations of Electron Guns for High-Power Microwave Tubes," Proc. Second Int. Symp. On Insulation of High Voltages in Vacuum MIT Sept. 1966, pp. 293-303.

electron magnetic moment is conserved. In this case the increase in Larmor radius is negligible. Taking the worst case of a sudden change in field direction, the resultant Larmor radius is given by 9.5×10^{-2} cm for the baseline design.

This is only a factor of 3 smaller than the bar spacing, however, the distance traveled by an electron while making a complete orbit is 6.5 cm. Therefore, the electrons complete only a fraction of an orbit during their transit through the support structure. With this fractional orbit, an average over the entire e-beam area and pulse duration gives an estimated reduction in foil support transmission (due to electrons impinging on the sides of the foil support bars) of ~ 1.5 percent.

2.8.4.3 Anode Structure

The anode structure must have low stress concentration and high electron transmission. The drift region which interfaces with the foil and foil support contains ground planes to short out the space-charge induced electric fields of the e-beam. Intercepting structures will be actively cooled.

2.8.4.4 Grid Structure

The grid structure is incorporated for the thermionic cathode design and serves two purposes (1) as a cathode mask in conjunction with a non- intercepting mode of operation, (2) as a means to control the waveform of the e-beam pulse, e.g., to steepen the rise and fall or ultimately, to switch the entire e-beam. Unless the cathode is segmented, the grid must be cooled to remove the heat associated with the grid current.

In the present design a magnetic field is used to guide and confine the e-beam from the cathode through the grid, foil support structures and into active laser volume. The guide field allows the use of a non-intercepting anode and foil support structure so that the effective transmission of these structurers to the high energy e-beam approaches unity. For this purpose, the grid is designed with a pattern matching that of the foil support. Thus, the electrons emerging from the grid structure are in the form of beamlets each of which is transmitted through the corresponding slot in the foil support structure (Figure 57). The e-gun anode is designed similarly except that the open area is slightly larger to allow for the slight variation in the magnetic

147

GRID MASK

- FOIL
- FOIL SUPPORT
- GRID
- CATHODE

SEGMENTED CATHODE
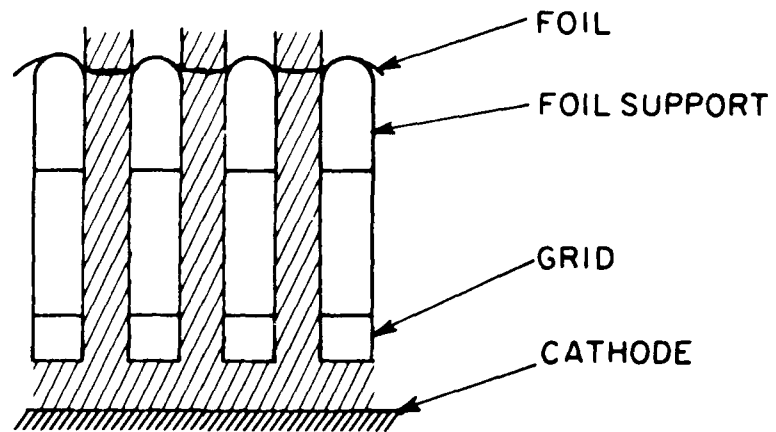
- FOIL
- FOIL SUPPORT
- NON EMITTING AREA
- EMITTING AREA
- CATHODE
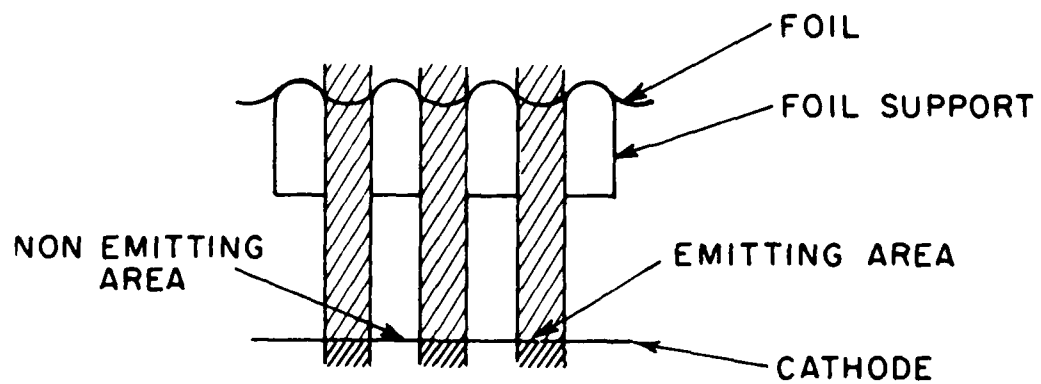
K 1542

Figure 57.   Non-Intercepting Foil Support Concepts

148

field from the anode to the foil support. For accurate alignment, fine adjustments in position and angular tilt of the magnetic field coil will be provided. This non-intercepting technique increases the e-gun efficiency by removing the geometric losses at the foil support.

2.8.5 High-Voltage Bushing

2.8.5.1 High-Voltage Design

The surface breakdown limits of pulsed insulators or bushings have been formulated[38] empirically for an optimum 45° angle stacked bushing as $E_{max} = 175\ t^{-1/6}A^{-1/10}$ [kV/cm] were t is the effective pulse duration in μs and A is the total insulator area in cm^2. For a 1000 cm^2 insulator and a 2 μs pulse this gives ~ 80 kV/cm. Typical designs are generally derated by a factor of ~ 2 which would give a reasonable design value for our particular application of ~ 40 kV/cm. This value only applies for the optimum grading configuration, and other configurations generally must be derated further.

2.8.5.2 Insulator Structure

The high-voltage bushing will be a brazed ceramic and metal ring structure which will stand off 300 kV dc, provide mechanical support for the e-beam terminal, and have sufficient temperature capability to permit bake-out. There are accelerator tube sections commercially available which have suitable characteristics, and, the present application will operate at an average electric field of 15 kV/cm which is conservative for 1-2 μs pulses.

A coaxial line from the high-voltage PFN terminates inside the bushing. This coaxial line will be made to carry heater power, control power and coolant connections inside the inner conductor as required. The bushing will be capacitively self-grading. The interior of the bushing will be filled with SF_6 at a few atm pressure to make its voltage capability at least as good as the vacuum side.

---

38.   Martin, J.C. AWRE, Aldermaston, England, unpublished.

2.8.6 Magnetic Field System

2.8.6.1 Energy Deposition

The magnetic field requirements are determined chiefly by e-beam energy deposition considerations. The desired e-beam deposition is uniform within the active volume and as sharp edge fall-off for efficient energy utilization. To analyze spatial energy deposition profiles an earlier computer code has been modified to include magnetic field and collimated beam effects.[39] The predictive capabilities of this code have been verified by experimental measurements on a number of e-beam devices at AERL. This code has been used to calculate the energy deposition contours for two face-to-face e-beams in the baseline design geometry for various e-beam voltages and magnetic fields. Figure 58 shows an example of resultant iso-deposition contours.

The laser beam requirement of $\pm$ 25 percent uniformity of the near-field intensity can be shown to imply that any e-beam energy falling outside the 50 percent contour is not effectively used. The fraction of e-beam energy transmitted through the foil which is deposited outside the 50 percent contour is plotted as a function of magnetic field intensity and e-beam width in Figure 59. For high fields, the e-beam edge fall-off is steep and the deposition fraction is high. For larger e-beam widths, the edge fringe region is smaller as compared to the central uniform region and again, the deposition efficiency is high. For the baseline design with a guide field of 2 kG, ~ 95 percent of the transmitted e-beam energy is deposited within the desired volume.

An important consideration which constrains the design of the magnetic field is the prevention of e-beam deposition upstream of the active laser volume. Deposition in this region will cause gas heating and density variations which must be convected downstream of the active volume within the interpulse time. Thus, upstream energy deposition places a lower bound on the flush factor required to achieve good beam quality. For a medium homogeneity requirement of $\Delta\rho/\rho = 3 \times 10^{-5}$, the upstream e-beam deposition must fall to < 1.5 x 10^{-4} of that in the active laser volume for an acceptable level of thermal

---

39.   Diffusion of Fast Electrons, Tekula, M.S. and Jacob, J.H., 34th Ann. Gaseous Electronics Conf. Boston, MA 1981.
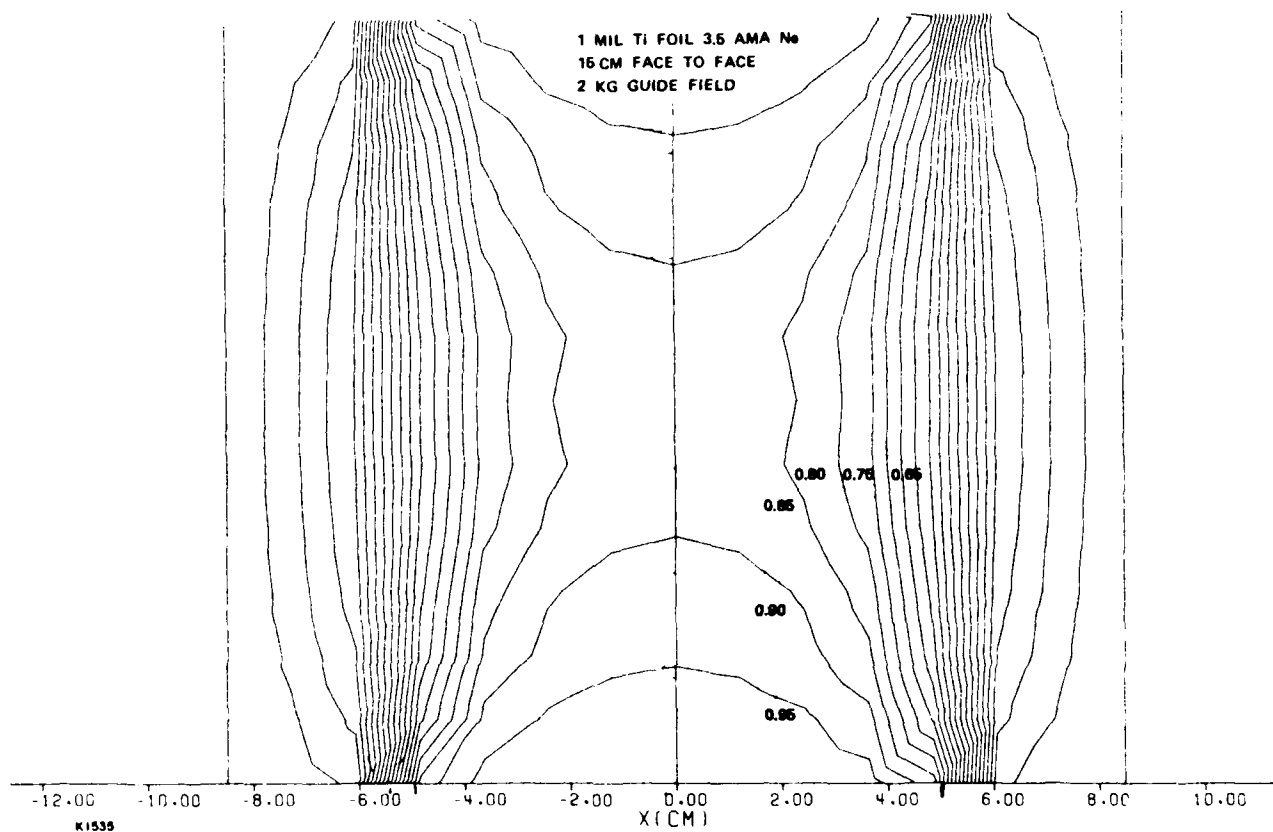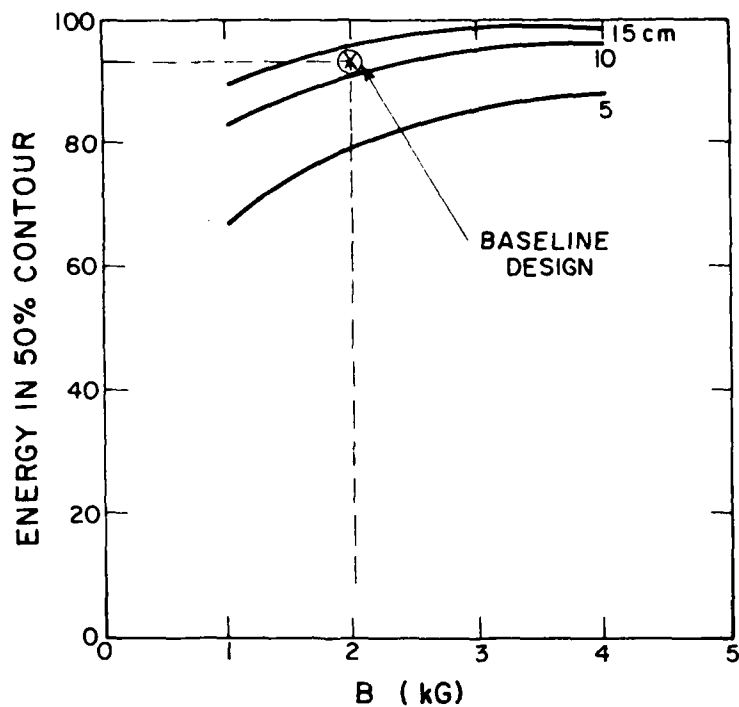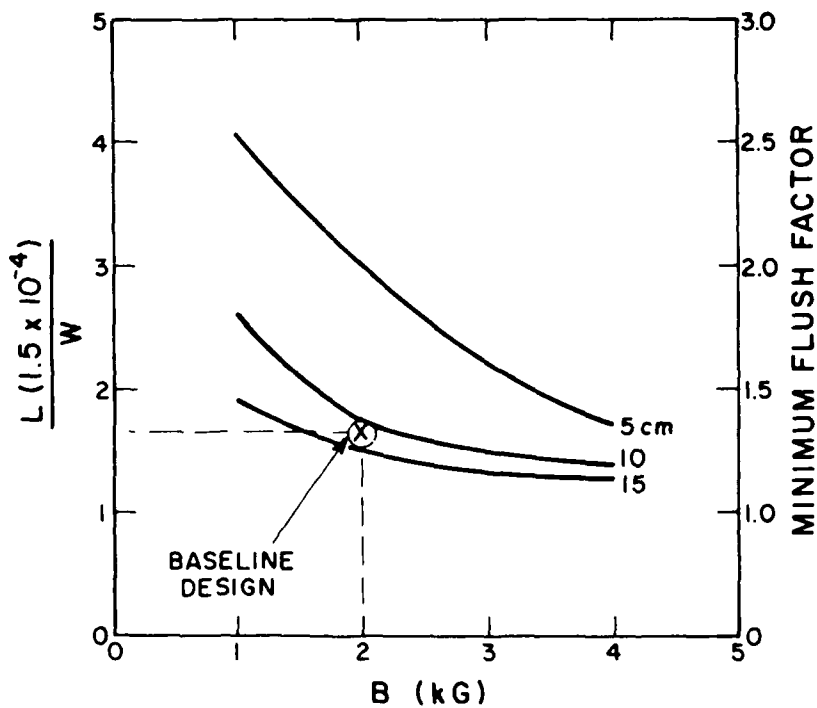
Figure 58.   E-Beam Deposition Contour Map for 275 kV, 10 cm Wide E-Guns

151

K1471

Figure 59.   Fraction of E-Beam Energy Outside the 50 percent Countour

K1472

Figure 60.   Summary of Results of Upstream Energy Deposition

disturbance. The effects of upstream energy deposition are summarized in Figure 60. On the right-hand vertical axis the corresponding maximum flush factor necessary to satisfy the $\Delta\rho/\rho$ requirement is indicated. For the baseline design values of beam width and guide field, 12 cm and 2 kG respectively, the minimum flush factor is ~ 1.3.

2.8.6.2 Magnet Configuration

The spatial uniformity of the magnetic field is determined by the required uniformity for e-beam deposition in the active volume. Any divergence of compression in the guide field will lead to a corresponding spreading or compression in the e-beam. Spatial uniformity of the guide field is determined by the design and placement of the coil set within the constraints of the e-gun and cavity structures. To minimize the magnet drive power, the coil windings are placed as close as possible to the laser cavity. One possible location for the coils is inside the muffler region. An advantage of this choice is that the resultant guide field converges from the cathode to cavity giving a compression in e-beam current. This beam compression alleviates the diode closure effect for carbon felt cathodes giving a smaller impedance collapse ratio for the 1 μs pulse. The disadvantages are the possible degradation in the performance of the acoustic muffler and the limitation of the cross sectional area of the windings.

For the baseline design, the field coils have been placed outside the flow channel and muffler structure for mechanical and thermal convenience. In this arrangement the windings have central opening of at least 55 x 180 cm in order to fit around the e-gun assembly. The minimum inside separation between the windings is > 55 cm.

For operational convenience, conventional water cooled copper windings rated for continuous operation have been chosen for the baseline design. The weight and power required to produce the 2 kG field is a function of the winding cross section a shown in Figure 61 for a square cross section. For these calculations, a conservative value of 80 percent for the copper packing fraction has been assumed. A racetrack coil shape is used in the baseline design with straight runs of 190 cm and semi-circular ends. A winding cross section of 32 x 32 cm is used. The resultant coils have a total weight of 20,000 lbs and require 120 kW to produce the 2 kG field. The cooling water requirement is estimated to be 25 gpm at 60 psi.
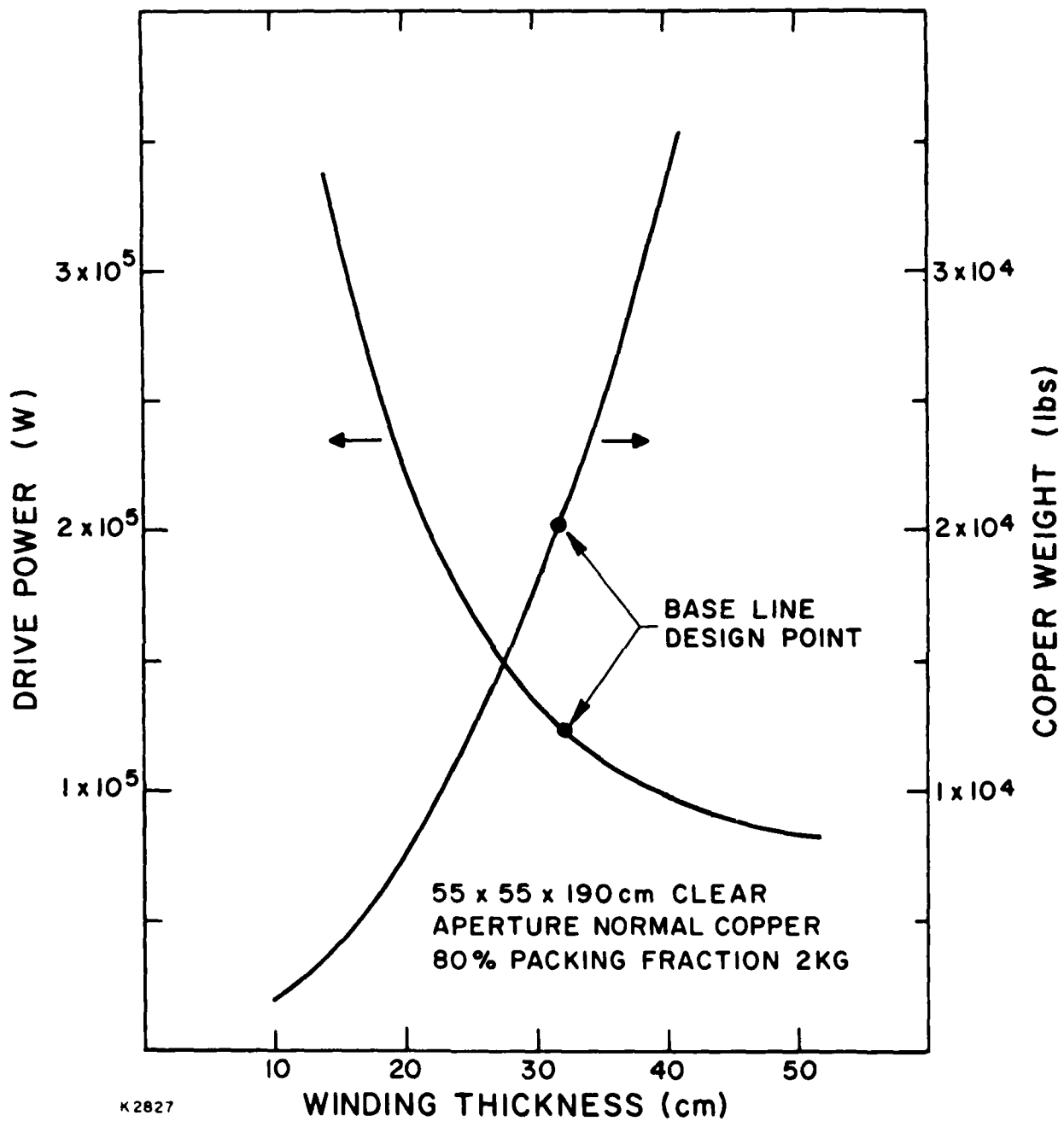
Figure 61.   Power Requirements for the Magnet Coil Set

154

The electric power required can be significantly reduced by using either cryogenically cooled copper or superconducting magnet designs. For example, a copper magnet cooled to 25°K consumes ~ 12 kW whereas a conventional Ni/Ti superconducting magnet requires 4 kW. For the present application, however, the added operational and system complexity are not justified and the baseline design uses a room temperature copper magnet coil set.

The magnetic field uniformity is calculated to be $\pm$ 4 percent within the active laser volume. The field at the e-gun cathode is ~ 20 percent higher than that in the laser cavity which results in a 20 percent expansion of the e-beam. Although this beam expansion increases the impedance collapse ratio, the baseline design falls within the factor of two constraints set by the pulsed power system.

2.9 PULSED POWER SYSTEM

2.9.1 Introduction

In this study program Physics International Company (PI) conducted a detailed assessment of pulsed power approaches to obtain a solid data base of subsystem constraints and trade-off issues. Five categories of pulsed power approaches each with several variations have been evaluated. These categories are:

1. Thyratron-switched PFN with step-up pulse transformer
2. Marx PFN
3. PFN - transformer charged
4. Blumlein network - transformer charged
5. Darlington network (N = 3) - transformer charged

The pulsed power subsystem design approaches were evaluated in terms of their ability to meet the set of requirements listed in Table 9. Sample waveform specifications are given in Figure 62.

From the assessment of viable approaches, a conceptual design has been selected which also addresses the future requirements of a communication system. The selected design combines proven technology with innovation to provide high reliability, performance, efficiency, and engineering simplicity. A review of the existing data base has been used in the selection of all components. Lessons from the successes and problems of rep-rate pulsed power systems at other laboratories have guided the design. A block diagram of the primary approach, shown in Figure 63, defines each of the major subsystem elements and illustrates the major functions and components. The selected design is described in more detail in Section 2.9.3 below.

2.9.2 Results of Concept Evaluations

2.9.2.1 Primary Design -- Balanced Pulse-Forming Network-Transformer Charged

Four primary criteria were used in selecting our pulsed power subsystem approach shown schematically in Figure 64 -- reliability, performance, efficiency, and engineering simplicity. Reliability includes system life, mean time between failures, and susceptibility and tolerance to fault modes. Performance is measured by achievable waveform (i.e., constant voltage into collapsing impedance loads, risetime, falltime, and post-pulse energy), and

156

TABLE 9. INTEGRATOR LINE PULSER PERFORMANCE SPECIFICATIONS

Parameter	Requirement
• Pulse Output Voltage (V_o)	-300 kV -5%/+10%
• Voltage Adjust	200 to 300 kV at same load impedance
• Load Impedance	8.6 Ω ±10%, may decrease by factor of 2 during pulse period
• Load Energy (each load)	5.25 kJ (10.5 kJ total)
• Voltage Pulse Length – Option:	1 μs ±10% 2 μs into constant 17.2 Ω load
• Risetime (10-90%)	< 0.1 μs
• Falltime (90-10%)	< 0.2 μs
• Tail Energy (after voltage has fallen to 0.1 V_o)	< 2% of total pulse energy
• Transients	(See Figure 62)
• Ripple (90-90%)	± 5% (See Figure 62)
• Output Jitter	< 20 ns, load to load < 20 ns, to external trigger
• Single Output Operation	Operate into only one load with other disconnected
• Pulse Repetition Rate (normal)	100 Hz (average)
• Maximum PRF	200 Hz for 1 s
• Interpulse Spacing	5 to 15 ms
• Run Time	> 1 min continuous
• Duty Cycle	5 20-s runs/day 4 1-min runs/mo

Figure 62. Line Pulser Output Waveform Definition and Limits

HIGH FREQUENCY RIPPLE (f $\geq$ 10 MHz) $\pm 5\%$ ADDITIONAL FOR 1st OVERSHOOT

1.20 V_c MAX

1.10 V_o MAX

1.05 V_o MAX

V_o = 300 kV -5% + 10%

0.95 V_o MAX

0.90 V_o MAX

0.90 V_o

$-0.90 V_o$

0.10 V_o

LIMITED ONLY BY 2% ENERGY

τ 90 - 10%

τ 90 - 90%

τ 10-90%
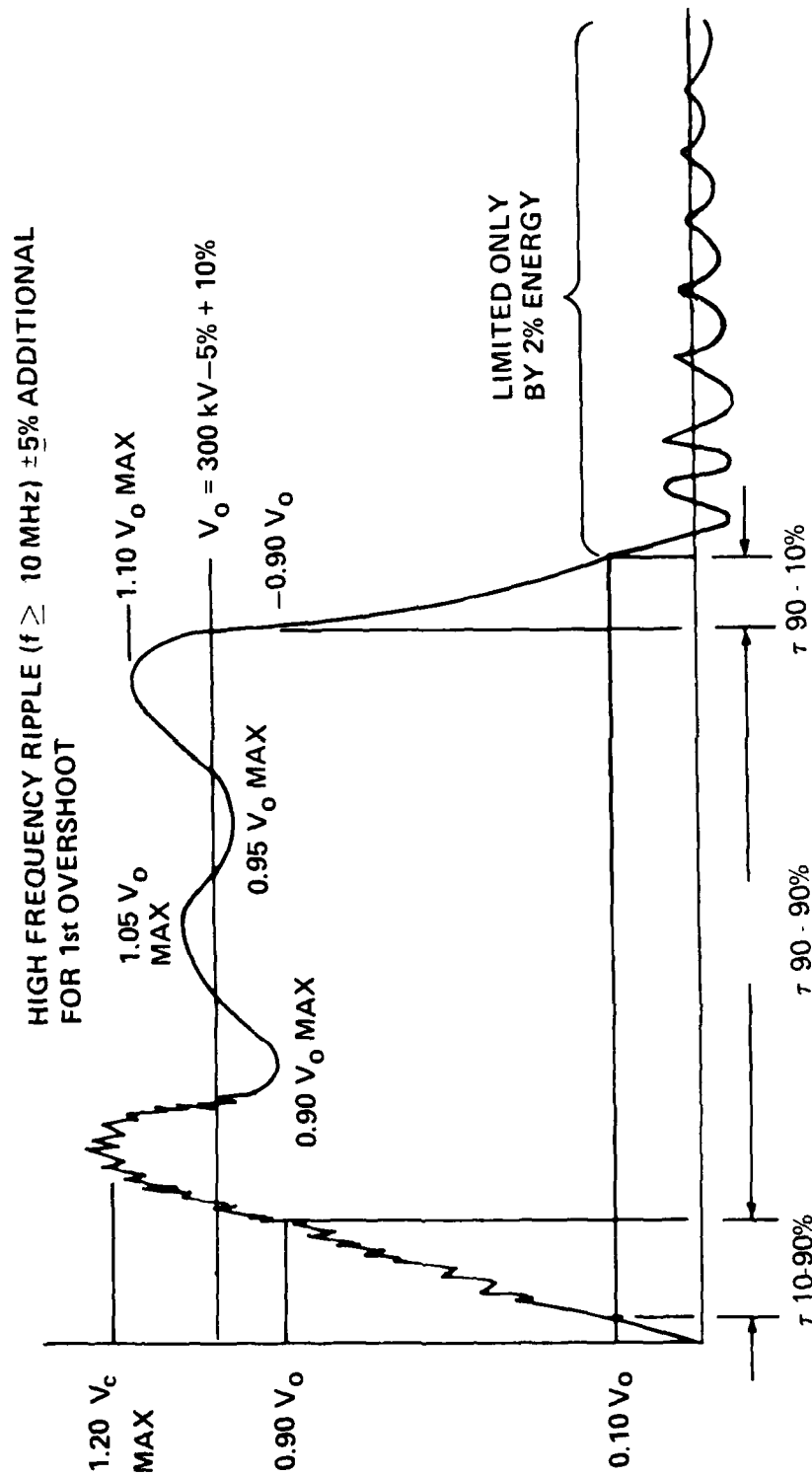
- Duration above 1.1V_o to be $\leq$ 50 ns
- Duration above 1.05V_o to be $\leq$ 0.1 μs
- Duration below 0.95V_o to be < 0.1 μs

158

Figure 63. Block Diagram of Primary Approach for Integrator Pulsed Power Subsystem
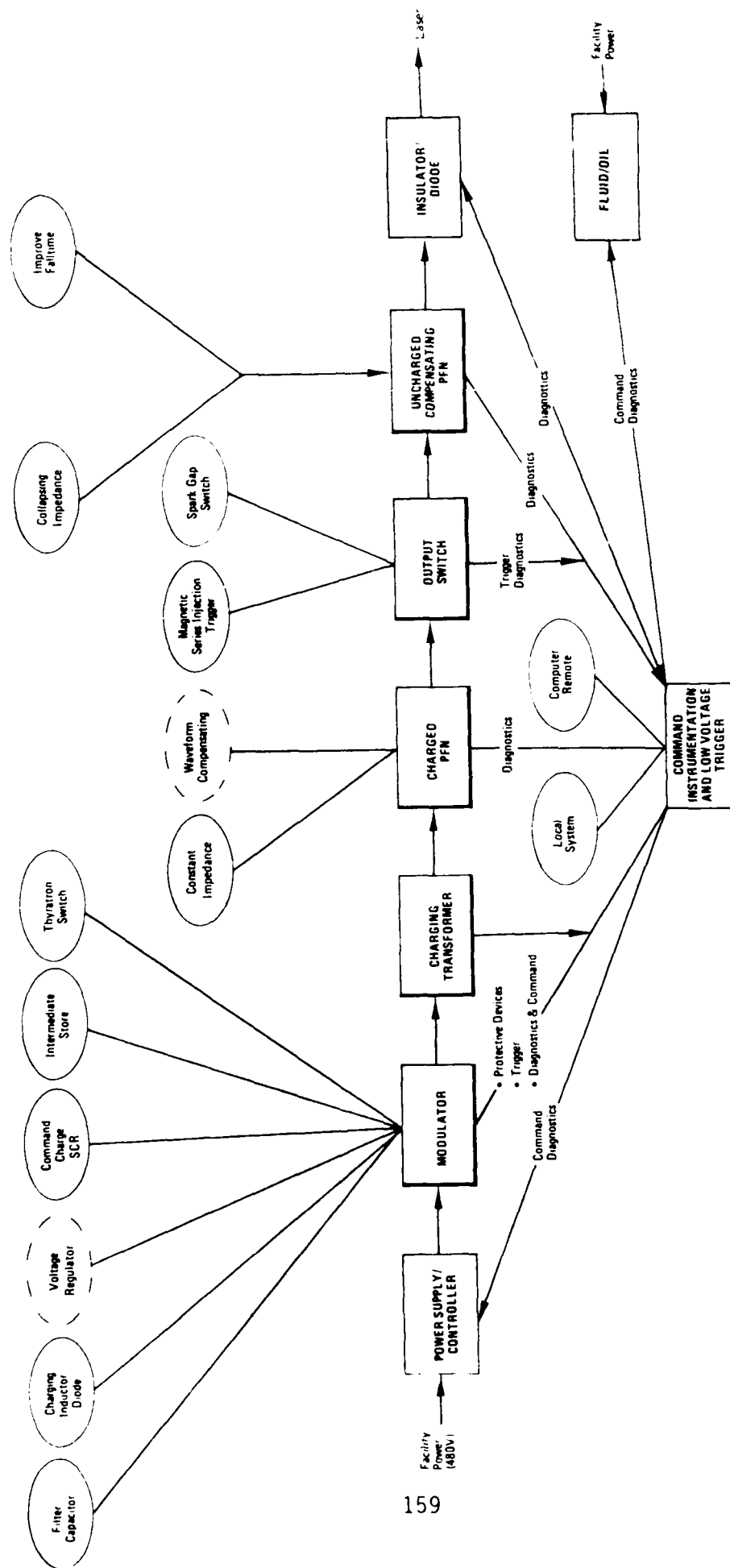
159

81-7-462
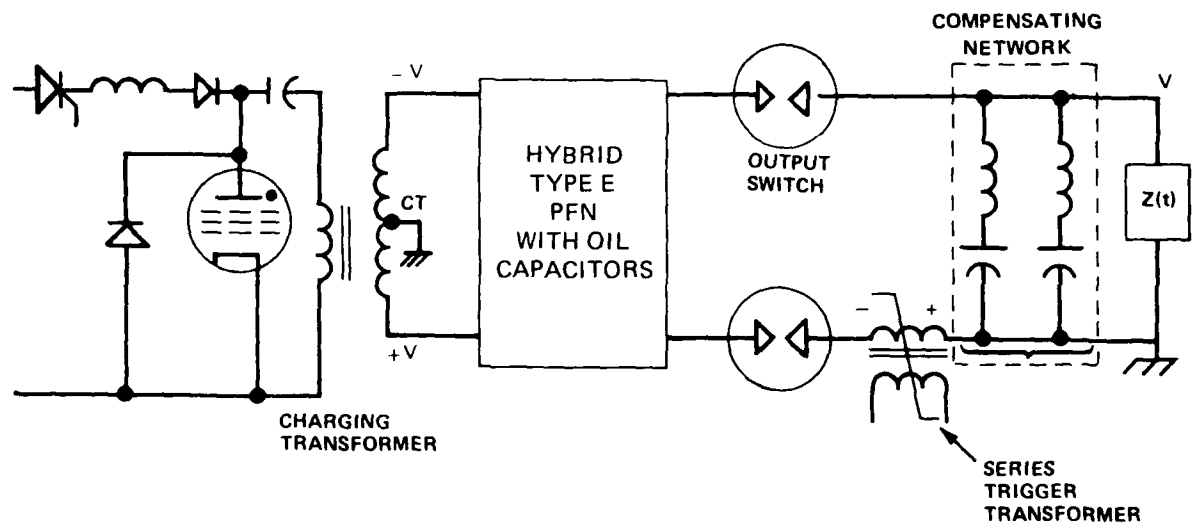
Figure 64. Primary Candidate for the Integrator Line Pulser is the Balanced
PFN--Transformer Charged Design

160

flexibility to vary output parameters and to adjust for variable load conditions. Engineering simplicity includes ease of assembly, ease of maintenance, and durability. Our selected design offers the following:

Major Advantages

- High reliability, performance, efficiency, and engineering simplicity. No compromises were made on any of these critical requirements.
- The selected PFN design centers around the use of oil capacitors. The advantages of oil capacitors are very significant for each of the evaluation criteria. Some of these advantages are:
  - Reliable - conservative stress
  - Long Life - no wearout
  - Simple oil circulation and purification
  - Low inductance
  - No grading of series sections
  - Tolerant of reversal and ringing
  - Low loss--dissipation factor < 0.001 at 100 MHz
  - Easy cooling--no hotspots
  - Ease of assembly and maintenance--visual inspection
  - Capacitance changeable--spacing or overlap
  - Good production and quality control
  - Tolerant of faults--self-healing
- The system exceeds all waveform specifications.
- A simple mechanical disconnect can provide the specified waveform into a constant impedance.
- Simple mechanical disconnects, along with the replacement of four coils and the change of spacing between a few metal plates, will adjust for different impedance collapses.
- The PFN is designed to efficiently couple energy into the diode, significantly reducing post-pulse energy and achieving high overall efficiency.
- The modulator subsystem uses long-life thyratrons with large derating factors. Interpulse modulation is achieved using long-life SCRs for command charge.
- The system is designed with very low stress levels throughout.
- The PFN design incorporates series injection triggering of two-electrode spark gaps for low prefire and low jitter operation.

161

Disadvantage

- The selected design is physically larger than some alternate approaches.

2.9.2.2 Thyratron-Switched PFN with Step-Up Pulse Transformer

The second pulsed power subsystem approach considered for the integrator is based on a PFN in the primary of a step-up output transformer, as shown schematically in Figure 65. To compensate for the time-dependent diode load, uncharged harmonic networks are added in the transformer secondary. This circuit is designated in Approach 1A. Several variations have been considered in response to the severe risks that became apparent during our analysis of this approach.

The first variation adds a peaking capacitor and magnetic output switch in the secondary of circuit 1A. This relaxes constraints on voltage risetime but does not achieve the falltime requirements. To this circuit we added a crowbar switch (Approach 1B). An alternative method of decreasing the falltime through passive networks in the secondary was also investigated (Approach 1C).

The results of our analyses can be summarized in terms of the following advantage and disadvantages:

Major Advantage

- This first concept has the potential advantage of very long lifetime switching. Thyratron and magnetic switches can be used for all switching functions.

Disadvantages

- The pulse transformer requirements, as a single-shot component, are significantly greater than any single-shot transformer ever built.
- The gap in pulse transformer technology is further widened by requirements for reliable, long-life, repetitive operation, i.e., reduced electric field stress levels and cooling.
- Capacitance and inductance parameters for the pulse transformer become an integral part of the circuit and, once built, cannot readily be changed. Several output parameters become fixed, substantially reducing the ability of the system to accommodate changes in load performance.
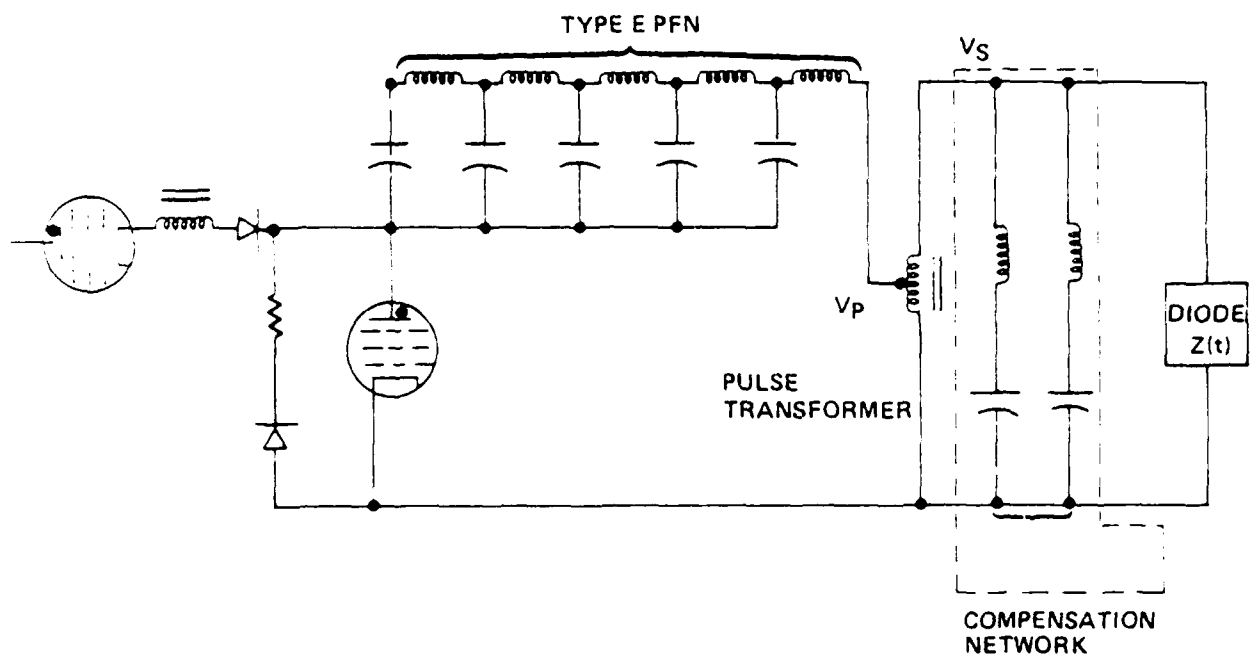
162

Figure 65. Thyratron-Switched PFN with Step-up Pulse Transformer

- Stray capacitance is a difficult problem and there is little, if any, safety margin for 100- to 200-ns risetimes (1A).
- Given output voltage and pulsewidth, energy per transformer is limited to a few kilojoules. This limits scaleability.
- For a 100-ns risetime, constraints on primary inductance are severe. Flexibility in PFN design is very limited. More importantly, the number of parallel thyratrons required to achieve the inductance criterion becomes physically unmanageable.
- Adding a peaking circuit so relaxes the primary inductance constraints that more detailed circuit and transformer design studies are warranted. However, the falltime must be actively reduced. The crowbar switch significantly limits efficiency, with losses > 20 percent.
- Using harmonic networks to decrease falltime does not appear feasible.

2.9.2.3 Marx Pulse-Forming Networks

We have investigated several types of Marx pulse-forming networks in the course of our assessments of viable approaches for the PFN system. Marx PFNs can be separated into two basic categories. In the first, each stage of the Marx contains a pulse-forming network. The second category uses a "standard" Marx generator as an element of a pulse-forming network, as illustrated in Figure 66. The full spectrum of PFN options has been conside d in our assessment of both categories. From this study we conclude the following:

Advantages:
- Marx PFNs are scaleable to very-high-energy systems that operate for short bursts.
- Rep-rate data exist at one-half the required energy per pulse. However, no Marx PFN (either single-shot or rep-rate) has achieved, simultaneously, the performance and efficiency of our selected design.

Disadvantages:
- The Marx PFN is the most complex approach possible. This complexity is exhibited by the large number of required spark gap switches and
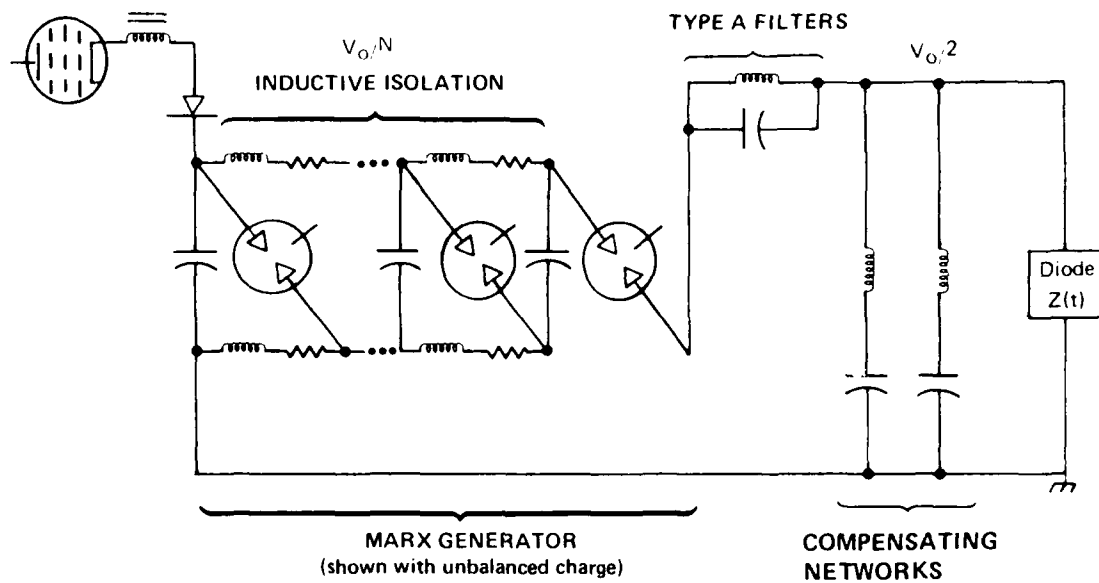
164

Figure 66.   Marx PFN Approach

duplicate pulse-forming networks. Marx generators have inherently complex triggering requirements, which are made even more difficult in modular rep rate systems.

- The Marx generators are particularly unsuited for reliable long life operation.

- Complex fault modes are an inherent result of the method of voltage step-up achieved by erection of a Marx generator. This is particularly true for inductive interstage isolation, which is necessary to meet minimum efficiency requirements.

- The spark gap switch in a Marx generator substantially reduced life. Switching in the system is achieved by a series of small spark gaps, each carrying the full current and charge delivered to the load for a given module. The result is at least a factor of 5 reduction in life over the switch concepts chosen for our proposed design.

- Marx generators are inefficient. To protect against fault modes from Marx erection and to ensure switch recovery, resistive damping is necessary. To achieve the required riseand falltimes without requiring many parallel Marx generators with parallel PFNs, crowbar switches may be required. Energy losses are, conservatively, > 20 percent.

- Repetitive energy storage capacitors are inherently problematical. Cooling considerations and corona within the capacitors very often require difficult designs.

2.9.2.4 Blumlein Network--Transformer Charged

The circuit is shown in Figure 67. The principal advantage is the use of a single 300-kV switch to yield 300 kV at the load. The disadvantages are threefold.

First, the charge transfer through the Blumlein switch is nominally twice that of the PFN switch. The life may therefore be expected to be less by the same factor.

Second, the waveform is not as good as the PFN. This results from dispersion of the switching wave as it travels down the first PFN. As a result, several parallel PFNs with higher impedance and many sections are required.
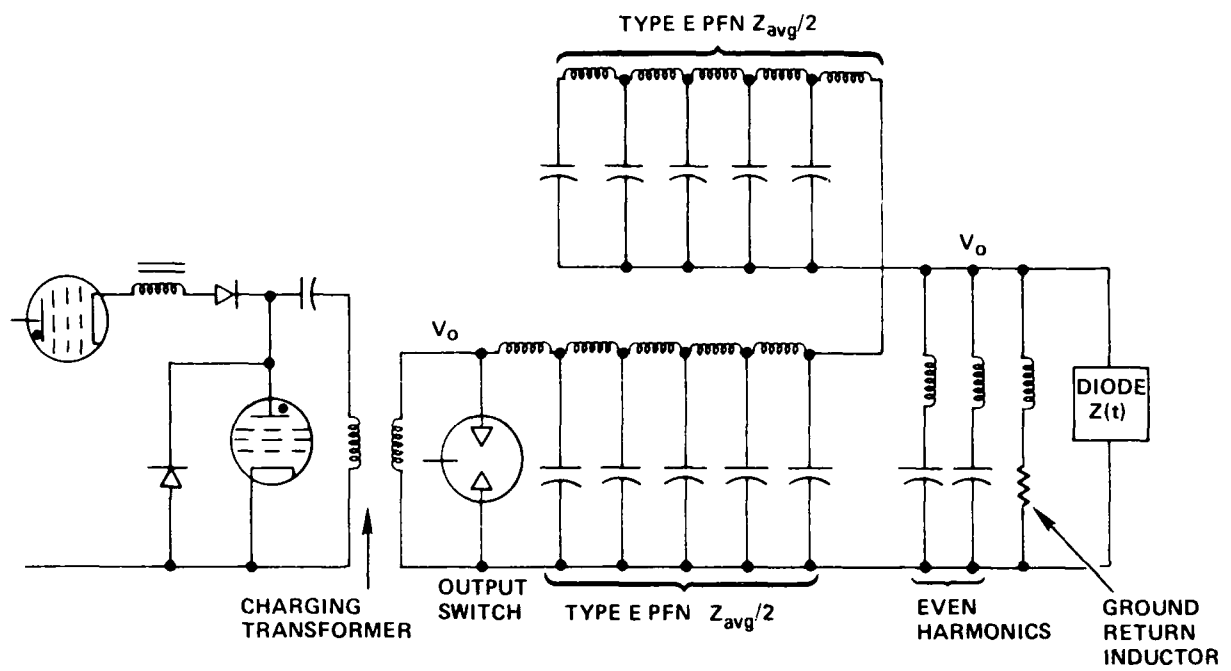
166

Figure 67. Blumlein Network-Transformer Charged

167

Finally, the presence of the ground return inductor causes a prepulse. There are also coupling losses, which result from charging resonances. Losses also occur during discharge.

The limitations above combine to make the Blumlein unattractive for this application.

2.9.2.5 Darlington Network--Transformer Charged

The Darlington network illustrated in Figure 68 for N = 3 is a generalized network in which the Blumlein networks (N = 2) and the PFN (N = 1) are special cases. Thus, all comments here concerning Blumleins apply in general.

The principal advantage is the use of a 200-kV switch. However, the charge transfer is nominally three times that of a PFN switch. In addition to the dispersion within an extra line there is also waveform degradation due to mismatches between lines.

Many PFN sections would be required to overcome these problems. To build such low-impedance, high-voltage lines, many lines would be needed in parallel to achieve the required mutual inductance.

For these reasons, Darlington networks of N = 3 become impractical. Higher values of N only aggravate the problems.

2.9.3 Description of Baseline Approach

The selected approach for the pulsed power subsystem for the integrator is the balanced transformer-charged pulse-forming network concept shown in the block diagram of Figure 63. We now proceed to briefly describe the subsystems that comprise this pulsed power subsystem. This subsystem exceeds all waveform requirements with significant margin.

2.9.3.1 Pulse-Forming Network Subsystem

Overview. We have selected as our primary approach the balanced charged PFN with the major components illustrated in Figure 64. The selected design concept configures the PFN subsystem into two modules, each driving a diode load of the laser cavity. The PFN design efficiently couples energy into the diode load, significantly reducing post-pulse energy into the diode and achieving high overall electrical efficiency.

168
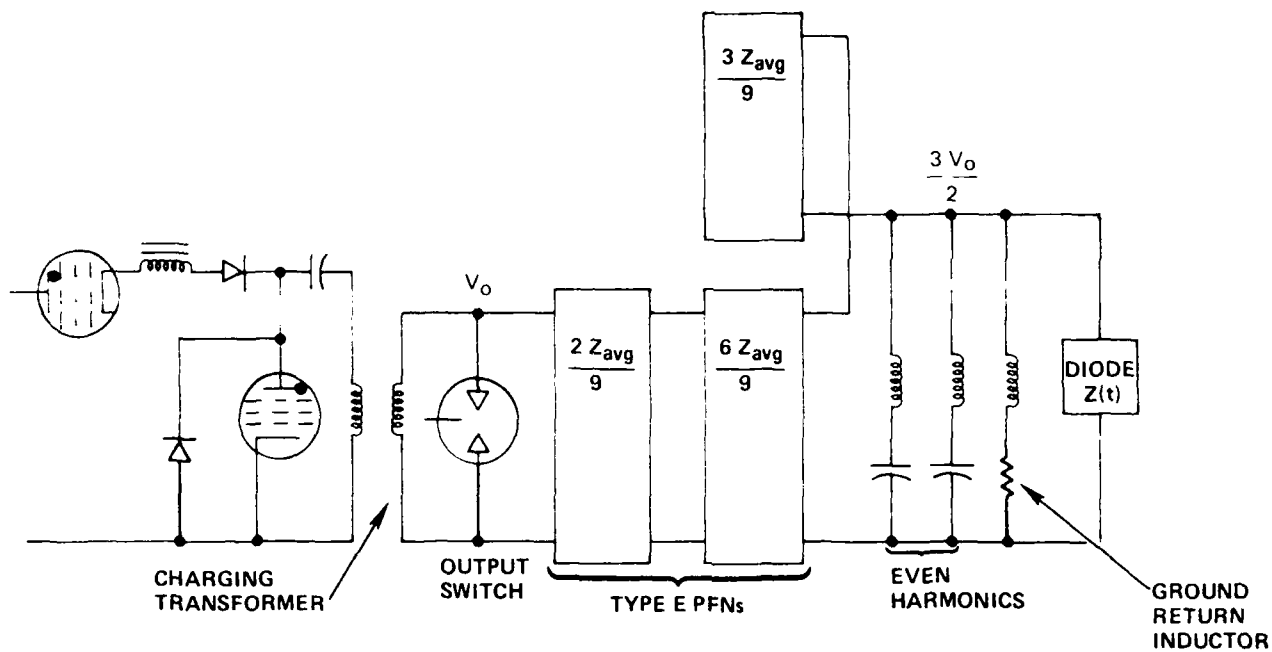
Figure 68. Darlington Network (n=3)--Transformer Charged

The most challenging requirement for the PFN is that it achieve a rapid falltime of the electrical pulse. The desired falltime, < 20 percent of the pulse duration, is achievable with a hybrid Guillemin Type E PFN.

The circuit shown in Figure 64 offers two important advantages. First, the waveform is inherently the best of all approaches considered. By using enough sections in the PFN, falltime can be reduced to about 15 percent without a crowbar switch. The second advantage is the slow current risetime through the charging transformer, which greatly eases the leakage inductance requirements and removes any capacitance requirement. These changes allow conservative dielectric stress, reliability, and long life.

A significant feature of our selected PFN approach is the use of capacitors formed using interleaved electrodes in a tank of oil. This design avoids the significant problems associated with the development, use, and reliability of high-voltage, rep-rate capacitor approach are as follow:

- Reliable--conservative stress
- Long life--no wearout
- Simple oil circulation and purification
- Low inductance
- No grading of series sections
- Tolerant of reversal and ringing
- Low loss--dissipation factor < 0.001 at 100 MHz
- Easy cooling--no hotspots
- Easy maintenance--visual inspection
- Capacitance changeable--spacing or overlap
- Good production quality control
- Tolerant of faults--self-healing

The very low inductance of the oil capacitor configuration makes it possible to build coils for Type E PFNs with the necessary mutual inductance (< 21 percent).

Heating of the oil does not involve the usual capacitor limitations of foil heating and contact resistance. Fractional loss in the oil per pulse will be minimal. With a stored energy of 10 kJ and 100 Hz the loss would be only 3.14 kW, or 0.3 percent.

A significant advantage is the ease of maintaining production and quality control. This is because the capacitor electrodes are subject only to the production and schedule limitations of mechanical shops.

Each oil tank contains a hybrid Type E PFN, the output switches and trigger, and a waveform compensation network. The capacitors of both the hybrid Type E and waveform compensation PFNs are designed to operate at 36 percent of the breakdown electric field value. This conservative approach gives a per-shot breakdown probability of $< 5 \times 10^{-9}$.

Reconfiguration of the PFN to provide the specified waveform into a constant impedance is by means of a simple mechanical disconnect.

2.9.3.2 Output Switch

This section describes the baseline design concept for the main output switch for high-repetition-rate PFN systems.

Switch Performance Requirements. One module of the line pulser must transfer 5.25 kJ to a time-averaged load impedance of 17.2 Ω at 300 kV, in a 1 μs pulse. Each of the output switches must pass 17.5-kA peak current and a charge of 17.5 mC/pulse, at an average repetition rate of 100 Hz.

Choice of Switch Design Concept. Several alternative switch designs were examined in light of the PFN switching requirements. The concept selected for the present application is a two-electrode spark gap triggered by an overvoltage pulse applied from a series-connected low-inductance pulse transformer. The driving requirements leading to this choice were to identify the simplest and most reliable spark gap concept, with particular emphasis on log life and minimum prefire rate. The switching requirements for the high-voltage PFN are not demanding in terms of switch inductance or switch arc formative time, allowing us to eliminate three-electrode spark gap designs from consideration. The three-electrode spark gap is essentially triggered in parallel, and the trigger generator impedance does not appear in series with the spark gap during the main pulse discharge. This arrangement allows the spark gap impedance to be minimized and is suitable for applications requiring an extremely fast (10-ns or less) risetime. When this kind of early-time performance is not required, the series-injection switch is preferred.

Operation of a series-injection trigger circuit is straight-forward. A very-low-inductance pulse transformer is placed in series with a two-electrode spark gap and the output voltage of this pulse transformer increases the voltage drop across the spark gap at the desired triggering time, causing the gap to break down.

The series triggered two-electrode spark gap was compared to a wide variety of other electrode configurations and triggering methods. These configurations include trigger planes located at the midplane, at V/N where N ranges from 2 to 10, enhanced trigger electrodes, "trigatron" systems, and e-beam and laser triggering. Planar and coaxial electrode geometries were evaluated. Performance of these switch designs was analyzed in theory and compared with a wide range of existing data.

The series-injection, two-electrode spark gap was chosen on the basis of prefire probability, reliability, life, and engineering simplicity. The primary advantages are as follow:

1. One can almost arbitrarily widen the operating range of the switch (subject only to breakdown of the switch insulators).
2. The switch gap is twice as long in this case as each of the subgaps are when a midplane trigger plate is used. This makes the switch roughly half as sensitive to electrode erosion, since a given quantity of charge transferred through the electrode system creates half the percentage change of gap length in a two-electrode as in a three-electrode switch. The advantage in life over three-electrode "V/N" configuration is even greater.
3. Removal of the trigger plate also removes any interference it may cause in the gas flow pattern when air is blown through the spark gap to aid in its voltage recovery and cooling. The air flow pattern for two-electrode switches is free of central stagnation points caused by the trigger plate, and it is much simpler to visualize and control.

In the present case, the spark gap will be stressed to 300 kV and pressurized to withstand at least 500 kV. In theory, by injecting a 500-kV trigger pulse, the spark gap can be broken down with no voltage applied to the PFN, giving an "infinite" operating range using the above definition. In

172

practice, this is unnecessary. Applying a trigger pulse of 350 kV through the low-inductance series transformer will guarantee firing of the gap, because spark gap breakdown characteristics are heavily skewed toward the self-firing voltage. That is, there is a voltage only a few percent higher than the average self-firing voltage at which the spark gap will always fire. However, at any voltage below the self-firing voltage, down to about 50 percent of this voltage, there is still a measurable probability of a spontaneous firing, or "prefire." A 350-kV trigger pulse will allow the spark gap electrodes to erode and increase the gap by over 25 percent before the gap begins to stop triggering on command. This degree of gap change requires several tens of millions of discharges for the spark gap design proposed here. The prefire probability will be better than one in 10^5 shots and can be even higher if desired.

The proposed baseline spark gap is illustrated in Figure 69. Stress in the insulator wall at switch breakdown will be below 12.5 kV/cm, comparable to the stress in the LS-15. The maximum wall stress at 300 kV will be still more conservative. At the given air pressure, wall breakdown could be expected at stresses of 80 to 100 kV/cm, indicating the safety margin built into the design.

2.9.3.3 Charging Transformer

The baseline design for the pulsed-power subsystem reduces constraints on the charging transformer. The performance requirements can be achieved using existing transformer technology. Four 300-kV charging transformers, each capable of transferring 3 kJ/pulse in ~ 12 µs have been selected. Two modulators are used in the baseline design, each driving its own pulse-forming network through a pair of charging transformers. The transformers are con- nected in parallel on the primary side and in series on the secondary side, with the common connection between secondary windings tied to system ground. This arrangement is preferred because it puts the transformer solidly inside the boundaries of known transformer designs and does not require a custom de- sign with center-tapped secondary.

To charge the pulse-forming networks in 12 µs, each transformer must have a primary leakage inductance not larger than 22.3 µH with a turns ratio of 4.3:1. There are no design problems associated with such a transformer.
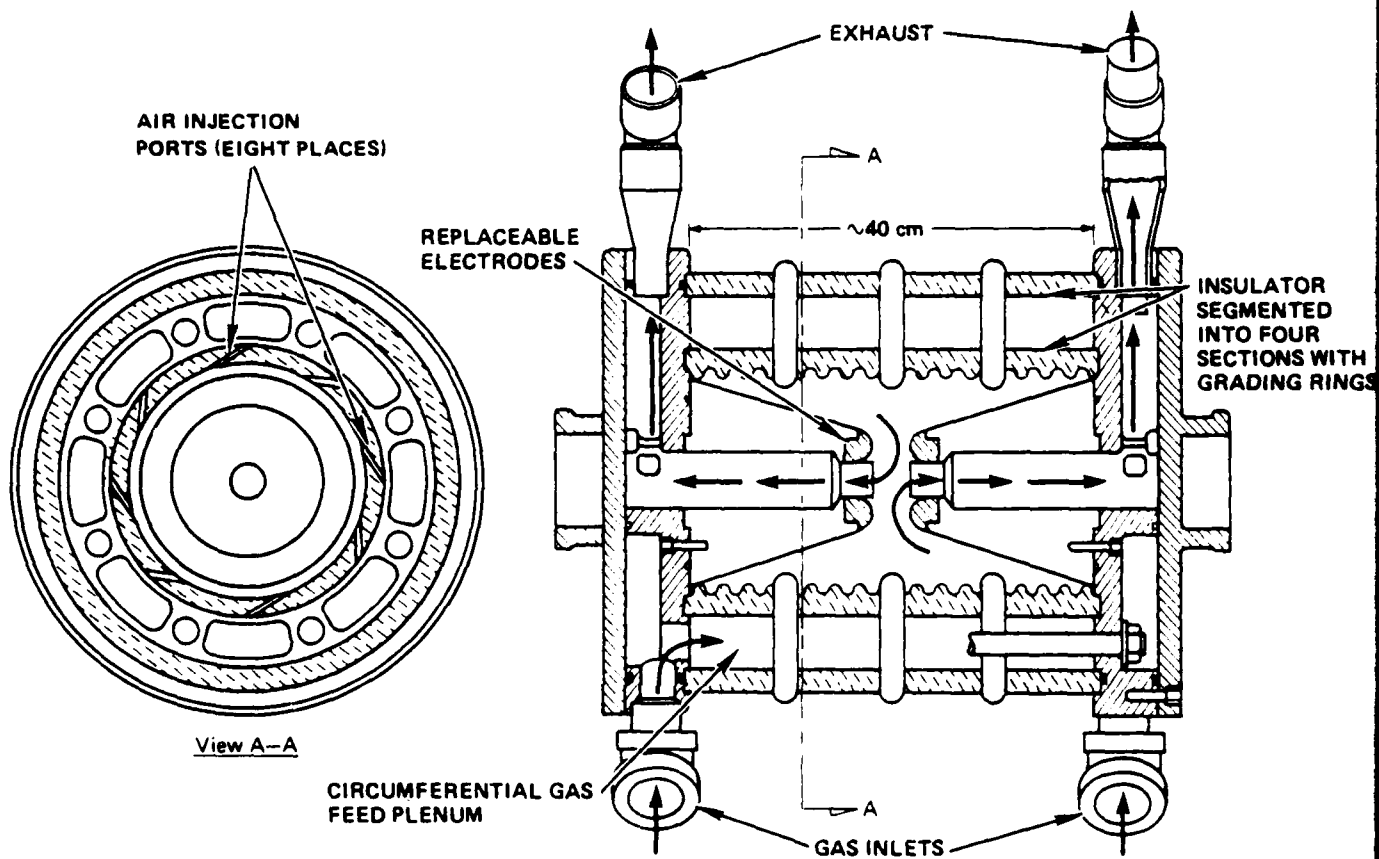
Figure 69. Cross-Sectional Views of the Proposed Output Switch

174

A major design requirement for this transformer is that the secondary be well graded for fast voltage transients so the sudden discharge of the pulse-forming network will not induce voltage breakdown between secondary turns. The design proposed takes this into account, and no damage will result when the pulse-forming network discharge removes the secondary voltage from the transformer (in ~ 100 ns) at the time that the transformer has achieved peak output voltage.

A brief survey of existing high-power pulse transformers has identified several units with performance parameters comparable with those required for the baseline system. For example, the 600-kV transformer, at 2.16 kJ/pulse, built by Stanganes in 1979 for the S^3 PFN system (currently installed at AERL), is a design similar to the one required here. In 1981, Stanganes delivered a 200-kV, 60-pps transformer at 4 kJ/pulse to LANL. This transformer had a turns ratio of 8:1, while the present unit requires a lower (easier) ratio. A transformer delivered to Fort Monmouth by Electro Engineering produces 170-kV output at 48 kJ/pulse with a burst rating 125 pps for 15 sec and a transfer time of 10 to 20 μs. This transformer had an 8.5:1 turns ratio, again more demanding than the unit needed for the present system. Some of the transformers identified in this survey are required to pass the rectangular output pulse from a PFN to a load with minimal distortion, a more stringent requirement than the present pulse-charging requirement. These factors indicate the basic technological feasibility of the pulse-charging transformer needed for the baseline power conditioning system.

The efficiency of transformer coupling is shown in Figure 70. Since the transformer coupling coefficient, k, can be made > 0.99, coupling losses should not exceed 2 percent. To these figures must be added resistive losses, which can be held to ~ 1 percent.

2.9.3.4 Modulator

Overview In our selected design approach, the modulator is defined as the pulsed-power subsystem between the primary dc power supply and the charging transformer. Electrical requirements for the modulator are presented in Table 10. The modulator, together with the charging transformer, provides the charging pulse to the PFN. The modulator consists of filter capacitors, a voltage regulator, a command charge section, intermediate storage capacitors,
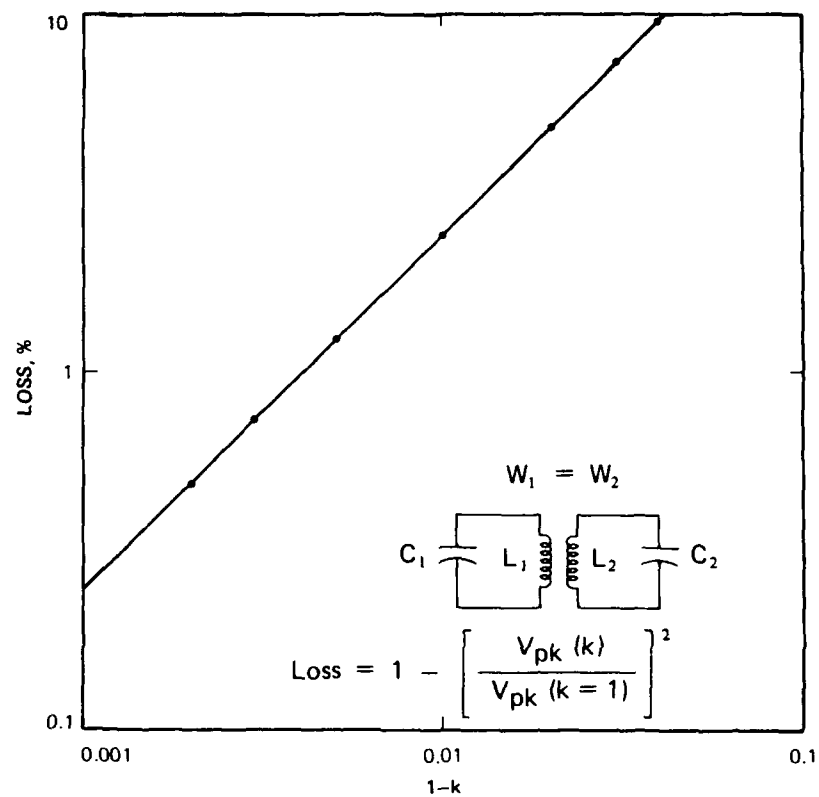
Figure 70. Losses in Pulse Transformer Charging a Capacitor

TABLE 10. MODULATOR SUSBYSTEM REQUIREMENTS

Parameter	Value
• Pulse repetition rate	100 Hz (average) 200 Hz (max for 1 s)
• Interpulse spacing	5 to 15 ms
• Run time	≥ 1 min continuous
• Duty cycle	5 20-s runs/day 4 1-min runs/month

177

and discharge circuit. Technical issues affecting the modulator design include the modulator response to a variable interpulse time, selection of the intermediate switch (thyratron) in the discharge circuit, and reverse current protection for the intermediate thyratron. In addition, possible fault modes, fault protection, and the use of a dummy load for system checkout have been designed and evaluated.

We have chosen a baseline approach in which the modulator subsystem is configurated as two separate modules of the total line pulser system. Each module will contain identical circuits that store 6.4 kJ/load and deliver this pulse energy to the charging transformer upon command at a pulse repetition rate of up to 200 Hz.

The use of two modules for the modulator subsystem is advantageous because this approach provides considerable flexibility in system assembly and delivery, system checkout, and demonstration of fault mode protection.

A wide range of modulator designs has been evaluated for charging the PFN system. Several options for the various switching requirements have been analyzed. These options include solid-state, magnetic, thyratron, and spark-gap switches. Performance trade-offs covering reliability, efficiency, and jitter have been conducted and compared closely with existing data.

Variations in the charging times and the number of stages of time compression have been parametrically studied for each of the several options for the PFN system. Several options for voltage regulation also have been evaluated with the final design awaiting further specification of requirements for reproducibility.

For the selected baseline PFN system the modulator design shown in Figure 71 has been chosen.

The modulator component design is affected strongly by the choice of a thyratron for the intermediate discharge switch. The operating characteristics limit both primary voltage and current. The three thyratrons considered applicable are the EG&G MAPS-40, the ITT KU-275C, and the ITT F-187. The peak and rms currents in the PFN charging loop may be determined for a selected charge time, τ, the energy stored in C_I, and the thyratron anode voltage. Peak and rms currents (at 200 Hz) vs. charge time for the three thyratron candidates are plotted in Figure 72 for 6.4 kJ/pulse. The average discharge current for each thyratron is shown in Table 11, along with the minimum number of thyratrons necessary to conduct this current.
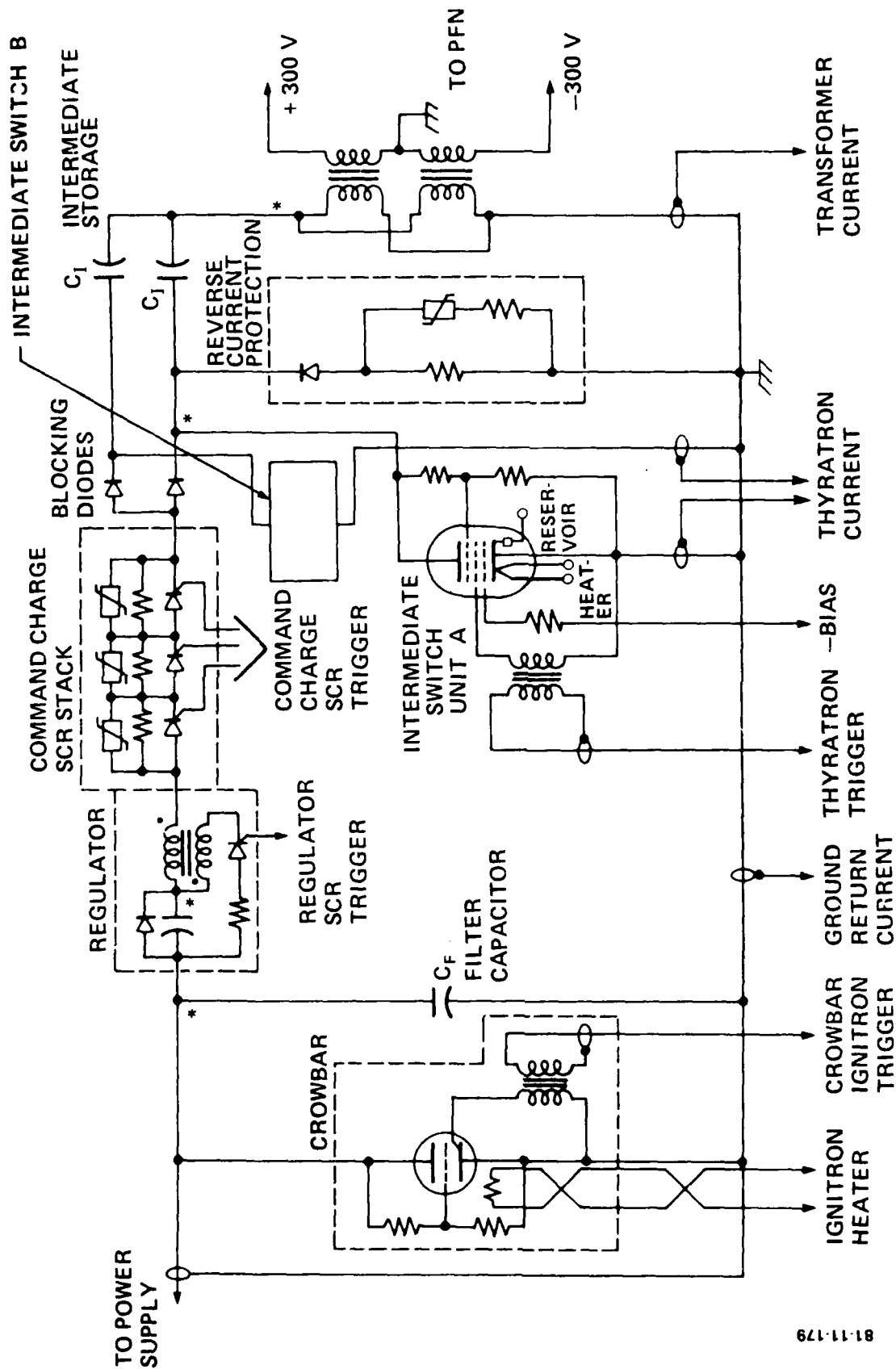
Figure 71. Schematic Diagram of Modulator to Charge PFN
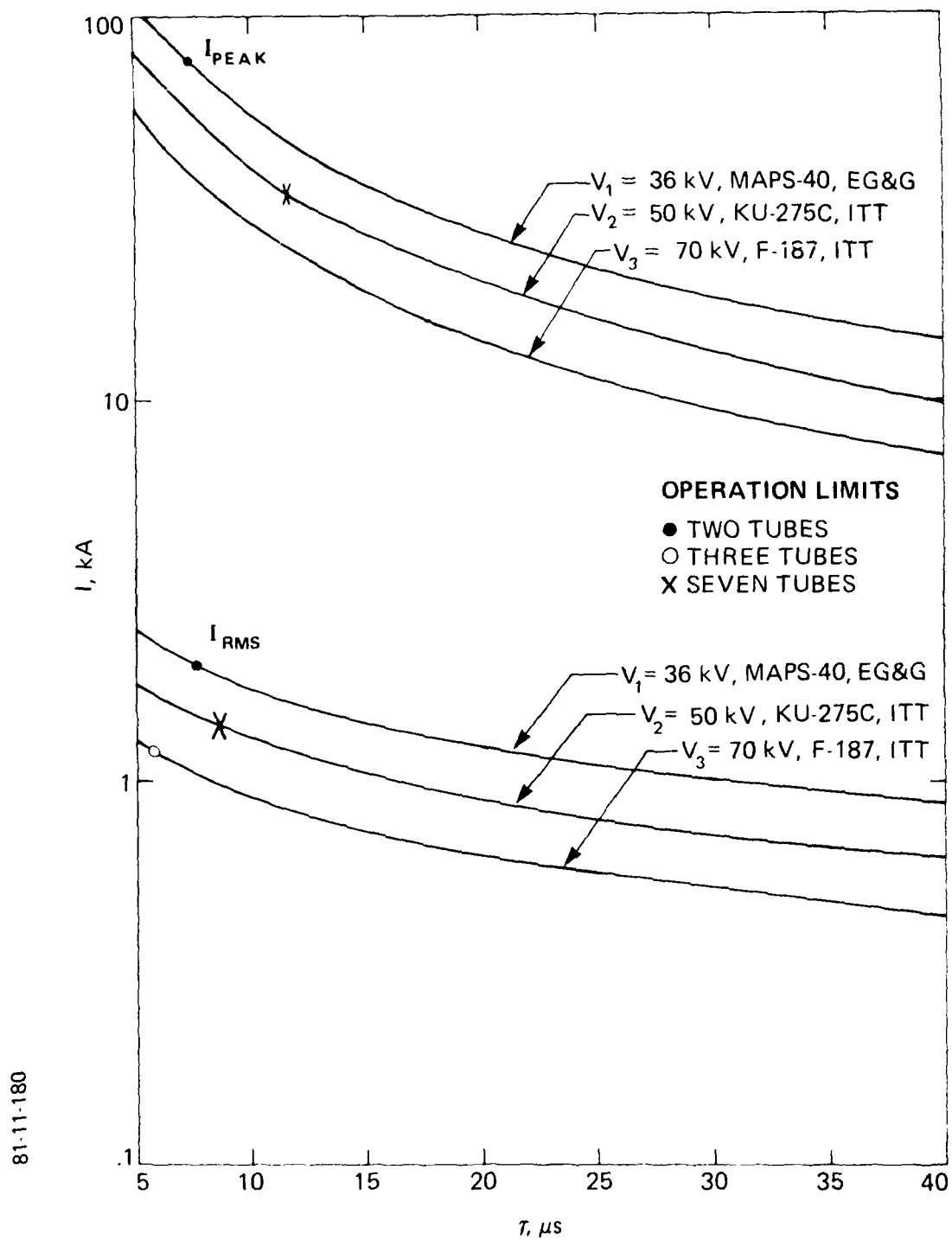
81-11-179

179

Figure 72. Peak and RMS Thyratron Current vs. PFN Charge times, τ

81-11-180

180

It is desirable to reduce the PFN charging time to assist in relaxing the probability of switch prefire and oil breakdown. The time dependence of these phenomena is weak, however, and the charging time is determined by the constraints of the charging transformer and thyratrons. Based on thyratron ratings and the minimum number of tubes listed in Table 11, the minimum charge time allowed by each thyratron is determined. A minimum of seven KU-275C thyratrons are required in parallel.

Table 11 shows that a minimum of three F-187s are required in parallel, while only two MAPS-40s are required. Each F-187 would handle 430 kW, wile the MAPS-40s would have to handle 640 kW. For long life and reliable operation, the MAPS-40s should be derated to at least 500 kW, so that three MAPS-40s would be required rather than one. The schematic of Figure 72 shows the operation of two thyratrons in parallel for each module. To eliminate current sharing problems, the intermediate store is divided into two equal capacitors. Each thyratron discharges a capacitor through the transformer into the PFN. A variation in triggering of one thyratron from the other would result in little difference in the voltage peak on the PFN.

A range of charge times can be chosen such that either the MAPS-40 or F-187 thyratron will operate with significant derating factors. However, reliable long life operation of the F-187 at its rated high average power levels is yet to be demonstrated.

The low peak and rms currents imply that an SCR would be better suited as the command charge switch than a thyratron. SCRs have been successfully operated in high-voltage stacks for several years at voltages up to 170 kV at average currents to 65 A. The device used in these stacks is an International Rectifier SCR rated at 600 V and 135 A rms. These switches are slow, turning on in 20 to 25 μs. However, since the intermediate store in the line pulser system is charged in 4 ms, these SCR devices are ideally suited as command charge switches.

TABLE 11.   AVERAGE CURRENT IN PFN CHARGING LOOP

V_C (kV)	Thyratron Type	Average Current (A)	Minimum Number of Tubes
36	EG&G MAPS-40	71	2
50	ITT KU-275C	51.2	7
70	ITT F-187	36.6	3

2.10 RAMAN CONVERTER SUBSYSTEM

2.10.1 Two-Step, Two-Cell Approach

The basis for our Raman conversion system is the two-step, two-cell approach which is shown schematically in Figure 73. The output from the XeF laser is directed into the first hydrogen cell. The output from a smaller laser operating at the first Stokes frequency is also inputted to this cell via a dichroic element. This first Stokes injector can be produced either from a small portion of the XeF pump which is split off from the main XeF beam and Raman converted to the first Stokes frequency in a separate hydrogen cell or from an entirely separate source; e.g., a dye laser. The XeF beam is converted to the first Stokes frequency in the first cell. After separation from the undepleted pump, this shifted beam is then used as input to the second hydrogen cell where it is Raman shifted to the second Stokes frequency using an injector at this second Stokes frequency.

There are several advantages which our proposed two-step, two-cell approach has over a system using a single hydrogen cell to convert directly to the second Stokes wavelength. These include wavelength flexibility, better control of parametric (four-wave) processes and potential improvement in output beam quality.

Wavelength flexibility can be achieved by using different gases in each of the cells. For example, deuterium can be used in the first cell and hydrogen in the second to produce output at ~ 470 nm (as opposed to ~ 500 nm produced from two shifts in hydrogen). This wavelength flexibility may be useful for transmission through certain types of ocean water.

Using two cells also makes suppression of parametric processes easier if they should prove to be a problem. This is due to the fact that as the number of wavelengths that are present increases, the number of combinations which can produce four-wave mixing increases dramatically. With the two-cell approach, no more than two wavelengths should be present at appreciable levels, while with a single cell approach as a minimum, the pump, first Stokes and second Stokes all need to be present.

It is our assertion[40] that the beam quality of the Raman shifted output beam depends only on the beam quality of the injector at the output
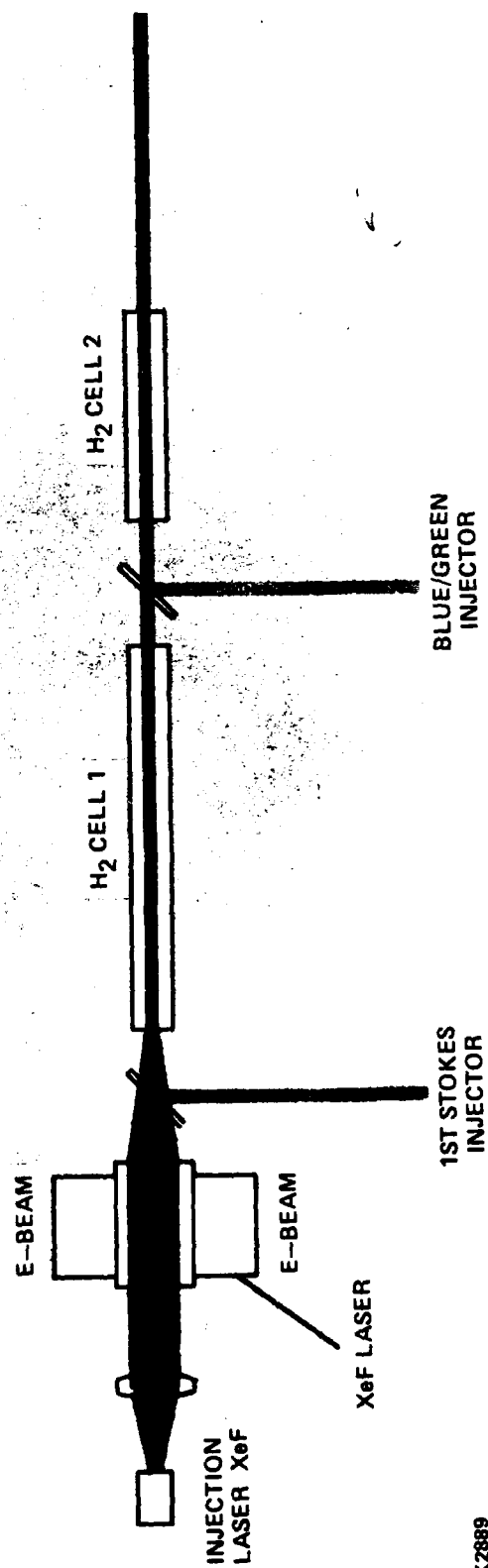
---

40. Developed under AERL IRAD funding

183

Figure 73. Schematic of Raman Converter Subsystem

K2889

184

frequency and any abberations acquired by that beam in passing through the Raman active medium and optical train. The two-cell approach makes optimal use of this assertion and is reflected in our conceptual design.

2.10.2 System Design Considerations

The Raman conversion process can be represented by the following equation

$$\frac{\partial I_p}{\partial z} = - g I_s I_p; \quad \frac{\partial I_s}{\partial z} = \frac{\omega_s}{\omega_p} g I_s I_p$$

where I_p and I_s are the pump and Stokes intensities, g is the Raman gain at the pump wavelength, ω_p and ω_s are the pump and Stokes frequencies and z is the length in the Raman active medium. From these equations, it can be seen that the fraction of the pump radiation converted into Stokes radiation depends on the quantity $g I_p L$, where L is the length of the Raman active medium.

The gain for Raman conversion in hydrogen falls into three pressure regimes.[41] At very low pressure where the hydrogen is Doppler broadened, the gain is proportional to the density. At slightly higher pressures, hydrogen exhibits a pressure narrowing regime where the gain is proportional to the density squared. At still higher pressures, collisional broadening occurs and the gain is then independent of the hydrogen density. It is in this last regime that we want to operate, since it is here that the Raman gain is maximum. The gain coefficient at 350 nm in this pressure regime is $\sim 4.5 \times 10^{-3}$ cm/MW.

41. Murray, J.R. and Javan, A., J. of Mol. Spectra. 42, 1 (1972).

AVCO EVERETT

In order to convert efficiently over a reasonable path length, it is necessary to operate at fairly high fluxes. To achieve these fluxes for a given pulse energy, one needs to operate with short pulses and/or high fluences. The pulse length is constrained by the XeF laser system requirement of ≥ 1 μs. We have, therefore, chosen to operate at 1 μs which is the shortest pulse length consistent with the system requirement and pulse forming considerations.

The fluences at which the system can be operated are limited by optics damage. Since uncoated transmissive optics can sustain higher fluences without damaging than can coated reflective optics, we have chosen to use uncoated window material for our Raman cells. The choice was made to accept the higher reflective losses in order to minimize the length needed for efficient conversion in the Raman active medium, since the length of the medium will affect beam quality.

Once the intensity is fixed, the length for the Raman active medium follows automatically. This length is split between the two hydrogen cells in our approach. The highest reasonable flux levels are chosen in order to keep this length at a minimum since thermal fluctuations in the cells will adversely affect beam quality. The beam quality is related to the thermal fluctuations by the following equation

$$\delta\phi = \frac{2\pi}{\lambda} \, \beta L \, \frac{p}{p_s} \, \frac{\delta\rho}{\rho}$$

where $\delta\phi$ is the rms wavefront distortion in radians, λ is the wavelength of the incoming radiation, β is the Gladstone Dale coefficient, L is the length of the Raman active medium, p/p_s is the pressure in atmospheres and $\delta\rho/\rho$ is a measure of the thermal fluctuation.

A baseline medium homogeneity ($\delta\rho/\rho$) of $\sim 3 \times 10^{-5}$ has been demonstrated at AERL.[42] Using this value in the preceding equation, the required 1.3 XDL beam quality should be achievable for a raman cell length of $\sim$ 190 cm at 6 atm of hydrogen. This path length is consistent with the required 30 percent conversion efficiency to the blue-green.

---

42. Under Contract No. DAAK40-78-C-0126 DARPA.

If Raman conversion is allowed to build up from the noise (spontaneous Raman scattering), then any photon which is emitted in an angle approximately equal to the aspect ratio of the Raman device may be amplified, leading to a Raman beam with high divergence. Since this is inconsistent with the system requirement of good beam quality, it is necessary to inject at the Stokes frequency. As discussed earlier, injecting also has other advantages. It inhibits the parametric processes which produce anti-Stokes and higher order Stokes radiation which would adversely affect the first Stokes conversion efficiency.[43] It also decreases the length necessary for efficient conversion and, thus, improves the overall quality be decreasing the beam degradation caused by thermal fluctuations in the Raman active medium.

Two basic options exist for the choice of an injector. A portion of the main XeF pump can be split off and converted to the desired wavelength in a separate H_2 cell or a completely separate source, for example, a dye laser can be used. There are advantages and disadvantages to both schemes.

If a converted portion of the main beam is used as an injector and it is injected in temporal phase with the main beam, then the correlated gain which is equivalent to the monochromatic gain is achieved. This concept is discussed in detail in papers by Stappaerts, et al.[44] and Trutna, et al.[45]

If a correlated injector is not used, an additional interaction length is needed in the Raman medium. If the uncorrelated injector intensity is assumed to be equally distributed among M longitudinal modes with random phases, the additional interaction length needed can be expressed by the following

$$\ell_c = \frac{nM}{gI}$$

where g is the Raman gain and I the pump intensity.

---

43.   Newton, J.H., and Schindler, G.M., Optics Lett. 6, 125 (1981).

44.   Stappaerts, E.A., Long, W.H., Jr. and Komine, H., Optics Lett. 5, 4 (1980).

45.   Trutna, W.R., Jr. Park, Y.K., and Byer, R.L., IEEE J. of Quantum Electro. QE-15, 648 (1979).

AVCO EVERETT

The difference between correlated and uncorrelated injection sources is illustrated in Figure 74 which shows the expected blue-green output energy as a function of injector energy. In generating Figure 74, it was assumed that the initial XeF energy was 100 J and that the gI_pL product for the Raman cell was that corresponding to our conceptual design. From Figure 74, it can be seen that the required 30 percent conversion efficiency can be achieved using either approach at reasonable injection levels.

Since the use of an uncorrelated injector would eliminate problems associated with temporally correlating the injector and the main pump beam and simplify alignment jitter problems, we have chosen to use this approach in our conceptual design.

2.10.3 Conceptual Design

Our conceptual design is presented in Figure 75. The output from the XeF laser which has been injection locked to provide narrow band operation is directed into the first hydrogen cell along with the 414 nm injector by using a dichroic element. After conversion to the first Stokes frequency in cell $\alpha 1$, any unconverted pump is removed via a dichroic and the first Stokes radiation is concentrated and used as the pump for the second Raman cell. A diffraction limited injector at the second Stokes frequency also enters this cell where it is used to convert the 414 nm radiation to the Blue-Green. This conceptual design meets the system requirements of 30 percent conversion efficiency to the Blue-Green and an output beam quality of 1.3 XDL.
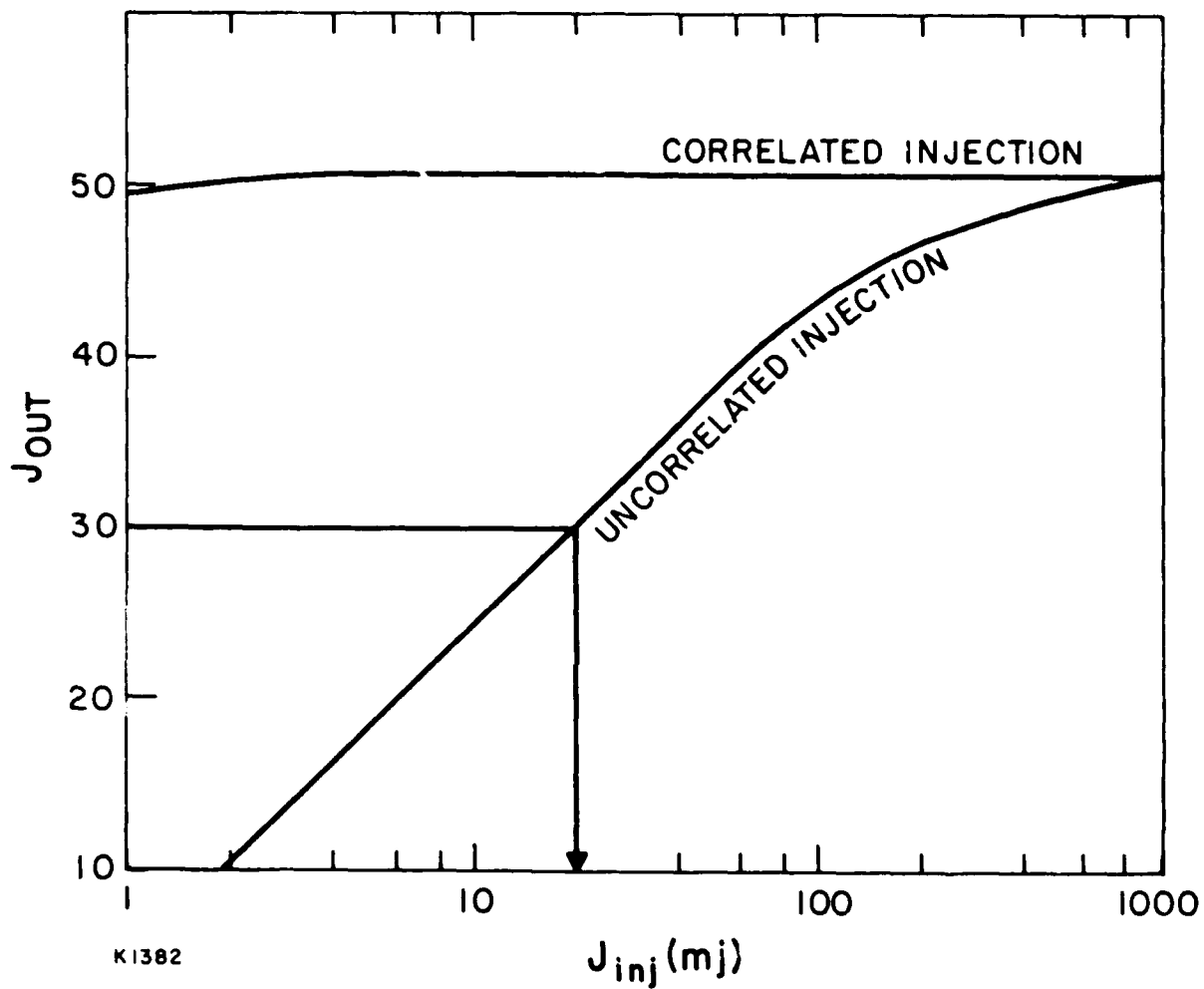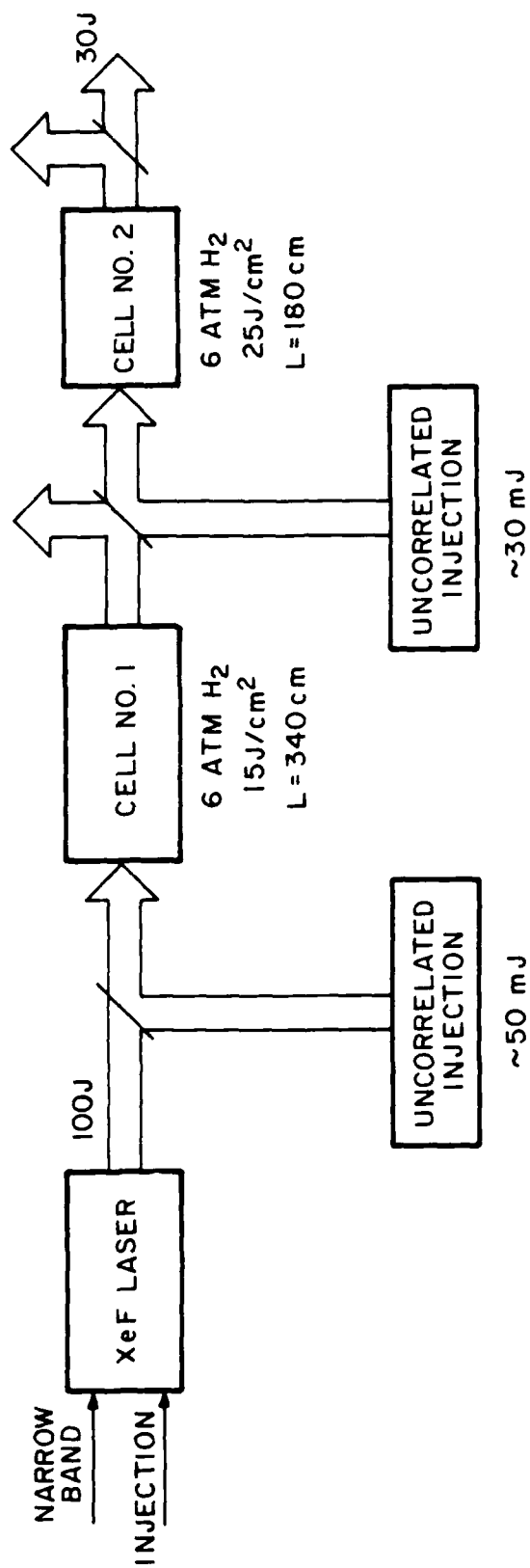
Figure 74. Output Energy vs. Input Energy for Injector Options

189

Figure 75. Point Design to Meet Blue-Green Requirements

K1381

190

3.0 SCALING AND SUMMARY

A conceptual design has been generated for a blue-green laser system with a closed cycle XeF laser as the driver. Design is based on device performance requirements of Table 12. The XeF laser serves to integrate laser technologies and to provide a test bed for addressing scaling issues. Scaling is of interest for a practical system of sufficient power to provide a driver for a Raman shifted blue-green laser as a ground based communications system. Scaling to higher powers for weapons application is also of interest.

The reported conceptual design meets all performance requirements. Demonstrated technologies are used wherever possible. The device is aimed at addressing all critical technologies including high reliability, high overall efficiency ($\geq$ 1 percent) and good beam quality ($\geq$ 1.3 x DL). The design allows minimal modification to implement thermionic cathodes and thereby demonstrate long run duration (> 10 hrs) and minimal modifications to demonstrate long ($\sim$ 2 μs) pulse lengths.

Component and system trade-offs were conducted to produce a baseline design. These studies point to areas where improvements in existing technologies are warranted. A listing of scaling issues and the extent to which they are addressed by the XeF integrator is given in the following section. Recommendations for critical experiments tests are given in Section 3.2.

3.1 SCALING MATRICES

Scaling issues are listed in Tables 12 and 13 for communications and weapons applications respectively. Much of these tables is self-explanatory, hence only those points which require clarification are discussed in this test.

3.1.1 Communications Applications

Cavity operating conditions will not differ significantly between the integrator and a full scale system.

E-beam/B-field issues of cathode life and outgassing are partially addressed in a 60-sec run duration. Other issues are fully addressed as listed.

TABLE 12. SCALING MATRIX FOR BLUE/GREEN COMMUNICATION

TECHNOLOGY	KEY ISSUES	VERIFICATION		
		FULLY	PARTIALLY	NOT ADDRESSED
LASER CAVITY	JOULES/LITER FUEL BURN UP ASPECT RATIO DEPOSITION UNIFORMITY INT. MEDIUM QUALITY	ALL ADDRESSED VARIABLE PUMP POWER (RAMAN CELL)		
E-BEAMS/B-FIELD	CATHODE LIFE UNIFORMITY CLOSURE VS. B-FIELD POISONING OUTGASSING	UNIFORMITY CLOSURE VS. B-FIELD POISONING	CATHODE LIFE OUTGASSING	
PULSED POWER	SWITCHES SCALABLE CONFIGURATION COMPONENT LIFE	SCALABLE CONFIG.	COMPONENT LIFE SWITCHES	
FOILS/SUPPORT ST.	TYPE OF COOLING LENGTH SCALING (P.C) OVER PRESSURE FOIL LIFE HIBACHI HEAT LOAD	TYPE OF COOLING OVER PRESSURE HIBACHI HEAT LOAD	FOIL LIFE	
FLOW	TEMP. UNIFORMITY TEMP. CONTROL COMPACT LINEAR CONF. MEDIUM HOMOGENEITY	TEMP. UNIFORM ETC. ADDRESSED		
RECYCLABILITY	MATERIALS COMPATIBILITY SCRUBBER SHAFT SEALS	MATERIALS ETC. ADDRESSED	STRUCTURE LIFE	
ACOUSTICS	SINGLE PULSE CLEARING MULTI-PULSE CLEARING MUFFLER CONFIGURATION ASPECT RATIO FAN NOISE	ALL ADDRESSED		
OPTICS	APERTURE SIZE MATERIALS COMPONENT LIFE ALIGNMENT FLUX AND FLUENCE	MATERIALS ALIGNMENT	COMPONENT LIFE FLUX AND FLUENCE	

K5036

192

TABLE 13.   SCALING MATRIX FOR WEAPON APPLICATIONS

TECHNOLOGY	KEY ISSUES	VERIFICATION		
		FULLY	PARTIALLY	NOT ADDRESSED

LASER CAVITY	JOULES/LITER
	FUEL BURN UP
	ASPECT RATIO
	DEPOSITION UNIFORMITY
	INT. MEDIUM QUALITY
		INTRINSIC EFF.
		P,T
			JOULES/LITER
			FUEL BURN UP
			ASPECT RATIO
			DEPOSITION
			  UNIFORMITY
			INT. MEDIUM
			  UNIFORMITY	

E-BEAMS/B-FIELD	CATHODE LIFE UNIFORMITY CLOSURE VS. B-FIELD POISONING OUTGASSING	CLOSURE VS. B-FIELD CATHODE LIFE POISONING	UNIFORMITY OUTGASSING	
PULSED POWER	SWITCHES SCALABLE CONFIGURATION COMPONENT LIFE	COMPONENT LIFE	SWITCHES	SCALABLE CONFIG.
FOILS/SUPPORT STR.	TYPE OF COOLING LENGTH SCALING (P.C) OVER PRESSURE FOIL LIFE HIBACHI HEAT LOAD	TYPE OF COOLING OVER PRESSURE FOIL LIFE	HIBACHI HEAT LOAD	LENGTH SCALING (P.C)
FLOW	TEMP. UNIFORMITY TEMP. CONTROL COMPACT LINEAR CONF. MEDIUM HOMOGENEITY	OPTION FOR FULL M		
RECYCLABILITY	MATERIALS COMPATIBILITY SCRUBBER SHAFT SEALS	ALL ADDRESSED		
ACOUSTICS	SINGLE PULSE CLEARING MULTI-PULSE CLEARING MUFFLER CONFIGURATION ASPECT RATIO FAN NOISE	SINGLE PULSE CLEARING MUFFLER CONFIGURATION	FAN NOISE ASPECT RATIO	MULTI-PULSE CLEARING
OPTICS	APERTURE SIZE MATERIALS COMPONENT LIFE ALIGNMENT FLUX AND FLUENCE	COMPONENT LIFE	MATERIALS ALIGNMENT FLUX AND FLUENCE	APERTURE SIZE MOPA

K 5037

Pulsed power is designed in a scaleable configuration. Component life, and switches in particular are tested to the extent of 60-sec run durations.

Foils and Foil Supports issues are addressed to the extent of 60-sec run duration.

Recyclability issues are addressed to the extent of total test duty time for the device.

All acoustics issues are addressed.

All optics issues are addressed to the extent of 60-sec run duration and total test duty time for the device. For example, optics flux effects are not fully addressed since transient effects persist in window and mirror thermal response.

3.1.2 Weapons Application

Since the integrator is significantly smaller in size from a weapons laser, scaling verification is not as complete as for the communications application.

Laser cavity issues related to very long pulse lengths are partially addressed by the integrator. Other issues are fully addressed.

E-beam deposition uniformity and outgassing related to very long pulse lengths are partially addressed. Other issues are fully addressed.

Pulse power for very high-power devices may require a different configuration. Switch performance for high-voltage and charge transfer is partially addressed. Component life in a weapons scenario is fully addressed.

Foils cooling by phase change is not addressed for very long flow lengths. Heat loads on the vacuum side of the support structures for high gun voltages is partially addressed. Other issues, such as the selection of cooling scheme, are fully addressed.

With the allowance for fan power to provide flow Mach numbers appropriate to high power lasers, all flow issues are addressed.

All recyclability issues are addressed.

Rep-pulse acoustic simulation for high-power devices is not designed into the integrator. Other issues are addressed as shown.

Certain optics issues are addressable only at full scale, e.g., fabricability, optical quality and figure. A MOPA configuration, appropriate to

very large devices, is not addressed. Materials selection, flux and fluence tolerances and alignment are partially addressed. Localized flux and fluence tolerances and chemical compatibility may be fully simulated to establish component life.

3.2 CRITICAL EXPERIMENTS

Although there has been a considerable amount of research into the various technologies that are necessary for fabricating a repetitively-pulsed excimer laser, there are a number of key issues remaining. The list of associated critical experiments is given in Table 14 for the various technologies. For the XeF laser there remains the issue of narrow line extraction. Injection experiments have been performed at room temperature that appear encouraging; to date no experiment has been performed at elevated temperatures. However, Northrup Corp. (NRTC) has funding to investigate narrow line, efficient, high temperature XeF laser issues. As far as e-beams are concerned, the issue that should be addressed is the outgassing rate from the cold cathodes. There is the additional issue of life for the cold cathodes even for the relatively short run durations required by the integrator. The PFN switches should be operated at the repetition rates required by the design. At Avco we have recently fabricated a switch test facility for the testing of the Marx switches on the scale-up. This facility could be used to test the integrator switches. In the case of foils, the life of Al clad Ti foil should be tested to insure that it has the required life under the cyclic stress conditions that it will be subjected to in the integrator. These foils may be tested on the proposed foil testing facility for the HgBr space-based program at Avco. Continued testing of optics coatings for chemical and optical survivability as well, as structural materials in the hot cavity environment is warranted. In the case of acoustics, ongoing DARPA programs at Poseidon and AERL will broaden the basis for evaluation of muffler concepts. Further we propose that the flow field on Humdinger Jr. be diagnosed with the DARPA/ Rocketdyne digital hetrodyne interferometer (DHI). The optics requires critical experimentation to determine not only chemical compatibility but also fluence limits of the window and mirror coatings. Corrective and adaptive optic concepts should also be evaluated. Damage thresholds for dichroic coatings required for the Raman optics should also be investigated, as well as further information on damage to uncoated transmissive optical elements.

195

TABLE 14.   CRITICAL EXPERIMENTS

TECHNOLOGY	EXPERIMENTS REQUIRED
LASER KINETICS	NARROW LINE < 0.5 Å EXTRACTION
E-BEAMS	LIFE, UNIFORMITY, OUTGASSING
PULSED POWER	SWITCHES
FOILS/HIBACHI	OVERPRESSURE, LIFE, TRANSPARENCY
FLOW	NONE
MATERIALS COMPATABILITY	OPTICS, STRUCTURAL MATERIALS
ACOUSTICS	(PENDING ONGOING TESTS) D.H.I IMPLEMENTATION
OPTICS	MATERIALS DAMAGE THRESHOLD

K1568-1

196

DISTRIBUTION LIST FOR FINAL TECHNICAL REPORT

Contract No. DAAH01-80-C-1783

Director, Defense Advanced Research Projects Agency
1400 Wilson Boulevard
Arlington, VA 22209
Attn: Program Management Division (MIS) (1 copy)

Defense Advance Research Projects Agency
1400 Wilson Boulevard
Arlington, VA 22209
Attn: Director, Laser Division (1 copy)

Defense Advanced Research Projects Agency
1400 Wilson Boulevard
Arlington, VA 22209
Attn: Dr. J.A. Mangano (1 copy)

Defense Advanced Research Projects Agency
1400 Wilson Boulevard
Arlington, VA 22209
Attn: Col. R.P. Benedict (10 copies)

Commander, U.S. Army Missile Command
Redstone Arsenal, AL 35809
Attn: DRSMI-RHS (Miller)(1 copy)
                (Duncan) (1 copy)
                (Womack) (1 copy)
                (Cason) (1 copy)
      DRSMI-RA (1 copy)
      DRSMI-IYD
      DRSMI-RRD (Howgate) (2 copies)